Genetically Encoded Fluorescent Biosensors to Light Up Biological Signaling

Shen Zhang

P.R. China

Bachelor of Science (B.S.), Sichuan University, 2013

A Dissertation Presented to the Graduate Faculty

of the University of Virginia in Candidacy for the Degree of

Doctor of Philosophy

Department of Chemistry

University of Virginia

May, 2020 Degree will be Conferred

ABSTRACT

The fluorescence imaging toolkit has continuously accelerated biomedical research. While a number of fluorescent biosensors are now available for studying the spatiotemporal regulation of signaling networks, it remains challenging to achieve multiplexed sensor imaging and imaging in more complex biological systems such as live animals.

Although most Zn^{2+} ions in our bodies are immobilized within proteins, less tightly bound Zn^{2+} has emerged as a key modulator in biological systems. In the brain, Zn^{2+} is concentrated into presynaptic vesicles and released into synaptic clefts along with other neurotransmitters such as glutamate. Synaptically released Zn^{2+} modulates brain excitability through its interaction with surface receptors of neurons. In the pancreas, Zn^{2+} secretion from β-cells in islets is an indicator of insulin secretion and the functional potency of islets. Previous studies have reported a number of genetically encoded Zn^{2+} indicators (GEZIs), which have been widely used to monitor Zn^{2+} in the cytosol and intracellular organelles. However, it is challenging to localize existing GEZIs to the extracellular space to detect secreted Zn^{2+}. In the second chapter, I describe two photostable, green fluorescent protein (GFP) based indicators, ZIBG1 and ZIBG2, which respond to Zn^{2+} selectively and have affinities suited for detecting Zn^{2+} secretion from intracellular vesicles. In particular, ZIBG2 can be effectively targeted to the extracellular side of plasma membrane. We applied ZIBG2 to monitoring glucose-induced dynamic Zn^{2+} secretion from human pancreatic islets. In addition, we developed novel GEZIs with fluorescence excitation and emission in the far-red region of the visible spectrum. We expect these new tools will be

particularly useful for *in vivo* imaging due to reduced phototoxicity and increased deep tissue penetration.

Imaging of serotonin, a crucial signaling monoamine playing important roles both within and outside the central nervous system, has been difficult. We fused a circularly permuted green fluorescent protein (cpGFP) with a serotonin-binding protein. Structure-guided mutagenesis and library screening yielded Green Genetically Encoded Serotonin Sensors (G-GESSs). G-GESS1 has proven to be a robust indicator for visualizing serotonin dynamics *in vitro* as well as in live cells and tissue. To validate the G-GESS fluorescent biosensors in complex biological systems, we applied G-GESS1 in brain tissue imaging and live mice imaging. We were able to capture the transient release of serotonin utilizing G-GESS1. Research is ongoing to continue the characterization of G-GESS1.

Compared to green fluorescent protein (GFP) based biosensors, red fluorescent protein (RFP) based biosensors are inherently advantageous because of reduced phototoxicity, decreased autofluorescence, and enhanced tissue penetration. However, there is a limited choice of RFP-based biosensors and development of each biosensor requires significant effort. In the fourth chapter, we describe a general and convenient method, which uses the genetically encoded amino acid, 3-aminotyrosine (aY), to convert GFPs and GFP- based biosensors into red.

ACKNOWLEDGMENTS

Thank you, mom, dad, and my wife Jieyi, for your love and unconditional support.

Thank you, Ethan, for always smiling at me, bringing me fancy stuff you made from daycare, no matter how late I got home from a busy day.

Thank you, Dr. Ai, for giving unfailing guidance throughout the years.

Thank you, Dr. Ji, for providing ideas and help (even one month of accommodation) in the early years of my Ph.D.

Thank you, all my labmates, for sparks from our daily conversations.

Table of Contents

Chapter 1

Overview of Genetically Encoded Fluorescent Biosensors

1.1. INTRODUCTION

Biosensors are essential tools for elucidating functions and dynamics of living organisms. To date, many types of biosensors with various readouts have been developed, and fluorescent biosensors are among one of the most widely used options. In particular, genetically encoded fluorescent biosensors stand out because of their biocompatibility and low toxicity. In this chapter, I summarize different types of genetically encoded fluorescent biosensors with focuses on development strategies and their applications.

1.2. FLUORESCENT PROTEINS

In 2008, the Nobel Prize of Chemistry was awarded to three prominent scientists for their discovery and development of green fluorescent protein (GFP), a uniquely structured protein with a spontaneously-formed chromophore situated in the center of a β-barrel (**Figure 1**). In addition to GFP, a large number of FPs have been discovered or engineered in the past two and a half decades. This unique protein family has drawn great attention, especially for applications in cell labeling and biosensing.

Currently, the term “fluorescent proteins” has been utilized to describe two major types of proteins: those producing inner chromophores through post-translational modification and those binding small-molecule chromophores from the surrounding.

1.2.1 Prototypical Fluorescent Proteins

Most prototypical FPs were initially discovered in marine organisms.[1] GFPs, the first series of FPs discovered, are by far the most developed fluorescent proteins. The brightness, folding, and photostability have been improved dramatically through directed evolution.[2] By changing the amino acids of and surrounding the chromophores, researchers were also able to change the emission wavelengths of FPs.[3] [4, 5] Since then, the broad range of the FPs spectrum has taken advantage of both Förster resonance energy transfer (FRET) imaging and multicolor imaging. In the past decades, endless efforts have been put into engineering bright and photostable FPs for tissue imaging. There has been tremendous improvement in this area.[6-8] The advantage of longer wavelengths in emission is to have less scattering and less absorption by endogenous molecules *in vivo*. In living tissue, red or even near-infrared fluorescent proteins would be ideal for imaging thick samples such as brain tissues. Another improvement is the development of FP variants that are better suited for different cellular compartments through protein engineering: for example, removing redox-sensitive amino acids to make the FPs less redox sensitive;[9, 10] Or changing the pKa of FPs to make the FPs suitable for acidic organelles.[11, 12] FPs engineered to these ends have provided tremendous possibilities in the development of biomarkers because of their optimized properties.

The first category of prototypical FPs includes the most widely used FPs. In the early 21st century, Tsien's lab and other scientists expanded the emission wavelengths of FPs across the visible spectrum. Subsequently, scientists are trying to develop FPs with more red-shifted emissions to allow better deep-tissue imaging.

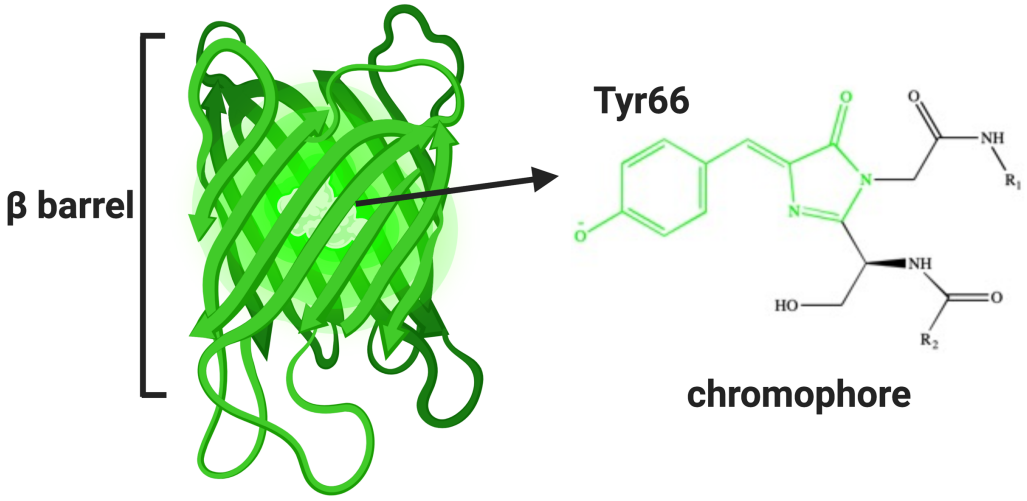

Figure 1. The structure and chromophore of Green Fluorescent Protein. GFP is composed of two major parts: the β-barrel and the chromophore. The protective β-barrel structure serves as a shield against environmental damages to the chromophore in the center, which is formed through post-translational modification.

1.2.2 Nonprototypical Fluorescent Proteins

The first type of nonprototypical FP was engineered from flavin mononucleotide binding proteins, which can be found in bacteria, plants, and fungi. The protein families have specific regions named light oxygen voltage-sensing (LOV) domains that bind the cofactor flavin mononucleotide (FMN). LOV domains are weakly fluorescent under UV illumination.[13] The first generation of FMN-binding FPs (FbFPs) was made using mutations to interrupt the covalent interaction between the FMN and surrounding residues.[14, 15]

Further efforts have been put into FbFPs to yield better photoproperties.[16, 17] Interestingly, one variant of the FbFPs, named miniSOG, plays a role as the fluorescent

singlet oxygen generator.[18]

Compared to prototypical FPs, FbFPs suffer from lower brightness and photostability. However, they have the advantages of fast turn-on fluorescence, being able to be fluorescent without oxygen, and small in sizes. To date, most of the FbFPs serve as markers in hypoxic or anoxic environments.[15]

Another type of nonprototypical FPs named UnaG, first characterized by Kumagai et al., can bind bilirubin reversibly and give a green fluorescence.[19, 20] This FP is brighter and smaller than GFP, can be expressed in hypoxic conditions, and is not pH sensitive in physiological ranges.

One of the significant achievements of nonprototypical FPs is the engineering of a full-length bacteriophytochrome (DrBphP) with a single mutation (D207H) to yield a fluorescent protein with a near-infrared emission.[21] Shu et al.[22] chose to limit the engineering of DrBphP to its chromophore-binding domain (CBD) and further developed a variant of the wild type DrBphP, named IFP1.4, which was expressed in mice to show spectrally deconvoluted liver fluorescence. To improve the brightness of fluorescent proteins in the near-infrared region, Filonov et al.[23] used another template, bacteriophytochrome RpBphP2. Using a similar process of domain selection and protein engineering, they were able to create an FP named iRFP. Recently, growing numbers of nonprototypical FPs have been developed using different bacteriophytochromes through protein engineering.[24-26]

Nonprototypical FPs provide significant advantages over prototypical FPs because of their more red-shifted spectra. This creates possibilities in deep-tissue imaging and displays less background when imaging *in vivo*. They do have disadvantages, though, due

to a lack of further optimization. Nonprototypical FPs are far less bright than prototypical chromophore FPs. Another drawback of nonprototypical FPs is that they have weak specificities for biliverdin and thus require exogenous biliverdin or co-expression of biliverdin-generating heme oxygenase for efficient fluorescence (**Figure 2**).[22]

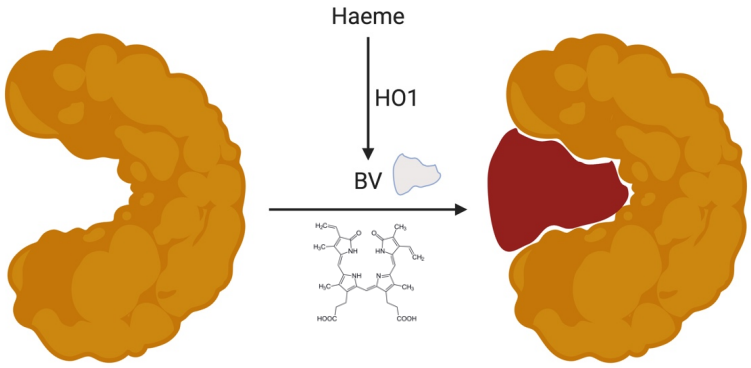

Figure 2. Schematic representation of biliverdin chromophore based fluorescent proteins. Biliverdin (BV), can be endogenously produced and bind with DrBphP. Though multiple rounds of directed evolution, BV and the protein are tightly bound and thus improving the efficiency of photon release.

Rhodopsin proteins work as light-dependent ion channels. Rhodopsins covalently bind retinal as a nonprototypical chromophore with very weak fluorescence in the near-infrared region. Because of its broad spectrum in absorbance, rhodopsin pairs perfectly with most of the red fluorescent proteins as a FRET acceptor.

For comprehensive properties of fluorescent proteins, please refer to https://www.fpvis.org/, a community-editable fluorescent protein database, which catalogs an expanded range of FPs.

1.3. FLUORESCENT PROTEIN BASED BIOSENSORS

Sensors are utilized in different experimental setups and targets of typical requirements. However, several general categories of sensors have been developed.

The selectivity and sensitivity toward their target of interest can be critical when designing sensors. The typical binding motifs of the sensor construct must bind the analyte of interest with specificity and a broad dynamic range. Another concern in engineering a sensor is whether it will interrupt the microenvironment, either by consuming the substrate itself or by influencing the downstream signaling pathways. The criteria to distinguish good from bad sensors are usually determined by kinetics, affinity, sensitivity, specificity, photostability, and reversibility. For quantitative sensors, the fluorescence readout must be ratiometric, either in excitation or emission. If changing in the concentration of the sensing target of interest only induces a fluorescence change in a single wavelength, such a sensor may not be suitable for quantification purposes. When applying sensors in tissue imaging or *in vivo* imaging, the quality of the results also relies heavily on the signal-to-noise ratio (SNR). SNR is the difference between the detectable range of signals and the noise of instruments and autofluorescence in tissue. More advanced imaging techniques are used in *in vivo* imaging to increase the SNR and resolution.[27, 28] As a result, such experiments rely on whether the sensors are suitable for such advanced techniques.

1.3.1 Förster Resonance Energy Transfer (FRET) Based Sensors

A FRET sensor typically requires three parts: the donor fluorophore, the acceptor fluorophore, and the sensing domain. When the two chromophores are physically close

enough and are situated in a preferable orientation, the FRET efficiency would be high. The extent of energy transfer can be determined either by detecting the fluorescence emitted from the acceptor fluorophore or by measuring the decrease in the fluorescent lifetime of the donor fluorophore.

FRET is commonly used in sensor constructs. First, FRET gives a ratiometric readout, ideal for quantitative measurement. Second, FRET sensors are easier to engineer. The disadvantages, however, are that FRET sensors often have a low dynamic range and their broad spectrum limits the use of other sensors with FRET sensors simultaneously.

Two factors must be taken into consideration when constructing a FRET sensor. The first factor is the spectral overlap between the donor FP emission and acceptor FP absorption. The second is a conformational change in the sensing proteins that alter the proximity and orientation of the donor and acceptor FPs in response to the change of analytes of interest.

1.3.1.1 Intramolecular FRET Sensors

The type of intramolecular FRET sensors is the most used FRET construct. It contains the donor and acceptor FPs fused at the N' and C' terminus of an interaction region. When there is a dynamic change of the analyte, there will be a conformational change in the interaction region. This alters the proximity and orientation of the two FPs and further changes the FRET efficiency (**Figure 3**). The quantification of FRET sensors is calculated as the ratio of FP fluorescence intensity in the acceptor to the donor. The concentration of the analyte of interest may be determined by plotting the FRET ratio into the standard curve.

The major advantage of intramolecular FRET sensors is that they are suitable for quantitative measurements. The disadvantages of intramolecular FRET sensors are quite obvious: First, they have a low dynamic range; the high baseline of FRET originating from tethered fluorophores, which is larger than with single FP sensors, may not be suitable for some cellular compartments. Second, the broad spectrum overlap with other colors of sensors may make it challenging to monitor the dynamics of two analytes at the same time.

Meanwhile, the FP pairs suitable for FRET imaging are limited because of the FRET efficiency, brightness, and photostability. A typical FP pair for FRET is cyan fluorescent protein and yellow fluorescent protein. Recently, the successful engineering of a super bright red fluorescent protein, named mScarlet, has created the possibility of a green fluorescent protein and a red fluorescent protein pair.[29]

The first intramolecular FRET sensor is the well-known Ca^{2+} sensor, named Cameleon.[30] Cameleon is the first genetically encoded Ca^{2+} sensor that enables the monitoring of Ca^{2+} dynamics in different cellular compartments of HeLa cells. Since then, countless intramolecular FRET sensors have been engineered.[31, 32] Recently, a unique scaffold for Zn^{2+} imaging, named eZinCh-2, was engineered. Instead of using sensing domains between the FP pairs, Hessels et al. used two out of four Zn^{2+} binding residues on the outsides of Citrine and Cerulean FPs to trigger the conformational change upon binding with Zn^{2+}.[33]

Intramolecular FRET sensors are also widely used in FRET-opsin and QuasAr2 voltage sensors.[34-36] These sensors utilize rhodopsin as a non-fluorescent FRET acceptor for different fluorescent proteins, and they monitor the changes in fluorescence of the FRET donors in the form of membrane potential change. This type of FRET sensors has

drawn tremendous interest recently. Many FRET-opsin based voltage sensors have been developed, and the colors of the sensors have been expanded toward the red wavelength.[37, 38]

Another extensive use of intramolecular FRET indicators is to monitor the dynamics of protein kinases. Because of the relatively significant conformational changes in the process of phosphorylation, it is relatively easy to engineer genetically encoded sensors where a change in conformation occurs in response to signaling.[39-44]

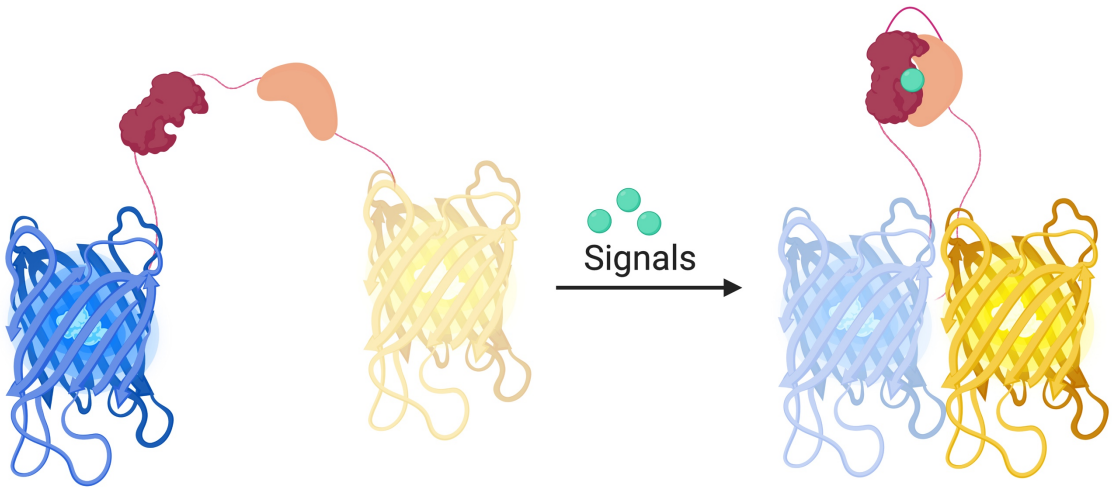

Figure 3. Schematic representation of intramolecular FRET sensors. Upon binding with the target of interest, the sensing domain would undergo conformational change, resulting in the change of proximity between the FRET pair, and eventually alter the FRET efficiency.

1.3.1.2 Bimolecular FRET Sensors

Bimolecular FRET sensors are primarily developed to sense signaling, such as signal-dependent clustering or receptor dissociation. Bimolecular FRET sensors consist of

two interactive domains linked separately to a FRET pair. They yield a high FRET ratio from the interaction of the two sensing domains. Similar to intramolecular FRET sensors, bimolecular FRET sensors possess the ability of ratiometric and reversible fluorescence change, and they have a higher dynamic range than intramolecular FRET sensors, because of the separation of the FRET pairs.[45]

Some bimolecular FRET sensors are designed to form large clusters. This leads to signal amplification, but it reduces the quantitative power of the observed signal change, as the ratio of the acceptor to donor fluorophores does not remain the same. Another disadvantage of bimolecular FRET sensors is that they require two separate vectors and express both in cells. This may result in different expression levels between the two parts of the sensors. Recently, a G-protein coupled receptor (GPCR) based sensor was developed to measure the activation of the G-protein complex in cells.[46] The sensor consists of a Gαi1, Gαi2, or Gαi3 subunit attached to mTurquoise2, and Gγ2 fused to cp173Venus. It was shown to rapidly detect G-protein dispersion induced by the activation of six different G-protein-coupled receptors. Another example was a FRET-based sensor that took advantage of the significant conformational change of inner loop three of GPCR, using M1-, M3-, and M5-acetylcholine receptors to monitor the acetylcholine dynamics in cells.[47, 48] Other bimolecular FRET sensors have been developed to detect the plasma membrane localization and the clustering of protein post-translational modifications.[49, 50]

1.3.1.3 Cleavage FRET Sensors

Cleavage FRET sensors are suitable for monitoring the activities of proteases. Cleavage FRET sensors are constructed by pairing the FRET donor and acceptor on either

side of a linker that has a substrate cleavage site for a specific protease. The FRET ratio of cleavage sensors can be high because the protease separates the two FPs. Although cleavage FRET sensors are easy to design, their disadvantage is obvious: the FRET changes are irreversible, and these sensors cannot monitor the dynamics of enzyme activities.

Cleavage FRET sensors have been developed for viral proteases, matrix metalloproteases, and caspases. Recently, a caspase-3 sensor was developed for *in vivo* imaging using mKate2 or eqFP650 and iRFP.[51]

1.3.1.4 Homo-FRET Sensors

Homo-FRET is a rare type of FRET in which the donor and accepter consist of the same fluorophores. With homo-FRET sensors, the fluorescence change is measured through anisotropy changes, rather than spectra differences. Homo-FRET sensors are less restricted than other FRET sensors for the selection of fluorescent protein pairs. Another advantage is that single-color sensors are more suitable for multiplex imaging. The disadvantage is that the homo-FRET sensors are more difficult to image and quantify. To date, a few homo-FRET sensors that monitor the dynamics of NADPH/$NADP^+$, Fe–S clusters and 3'-phosphoinositides have been developed.[52-54]

1.3.2 Single Fluorescent Protein Based Sensors

With the drawbacks of FRET-based sensors, such as their broad spectral profile bandwidths and low dynamic ranges, monitoring multiple targets and more complicated organelles is challenging. In comparison, genetically encoded sensors using single

fluorescence as readouts are more versatile than FRET sensors and have been extensively developed recently.

Compared with FRET sensors, single FPs are smaller in size, require narrower spectral bandwidth, and can be applied to a broader range of fluorescence from blue to near-infrared. They also often have higher dynamic ranges than FRET sensors. One of the drawbacks of single FP sensors is that many of them are intensiometric and, therefore, can sense only relative changes. Nonetheless, this issue can be addressed by using the excitation ratiometric change of GFPs, as the chromophore contains both protonated and deprotonated forms. There are two primary constructs of single FP sensors. The first requires only an FP itself and exploits a natural sensitivity of the FP to the target. The second, and more popular construct, is to attach the sensing/binding domains of the target of interest onto the FP to modulate its fluorescence. A major example of the first construct is to substitute the chromophore of wild type FPs with non-canonical amino acids (ncAAs), mainly tyrosine analogs. These tyrosine analogs are chemically sensitive to analytes such as H_2S and reactive oxygen species (ROS).[55, 56] For the second construct, the optimizable elements are similar to those of FRET sensors, consisting of an FP, an interaction or binding domain, and linkers. These sensors use a circularly permuted version of FPs. This provides a new open-cut that is close to the chromophores of the FPs, so it allows protein fusion onto the termini to effectively manipulate the solvent and oxygen accessibility of the chromophore. Some sensors are attached with reference FPs onto the c-terminus of the sensors, which is distant from the sensing part, to provide an internal control for ratiometric imaging.

1.3.2.1 Intrinsically Sensitive Single FP Sensors

The chromophore of FPs is usually sensitive to the microenvironment, such as pH, and it may be reactive to some ROS. The protonated chromophore of FPs has a massive blue shift in absorption, with very dim fluorescence at standard excitation wavelengths. In this case, the first and very successful intrinsically sensitive single FP sensors are pH sensors.[57-59] In 2012, a red version of pH-sensitive FP was developed, it enables multiplex interrogation of synaptic activity.[60]

Rational design and random mutagenesis of residues surrounding the chromophore can alter the spectral properties and change the chromophore pKa to become more or less sensitive to physiologically relevant pH. By further optimizing the pH-sensitive FPs, ratiometric pH sensors have been successfully engineered as well.[61-63]

High concentrations of halides can induce changes in chromophore pKa, leading to intrinsic FP sensors for chloride and iodide.[64]

Some FPs are extremely sensitive to metals. Copper can efficiently quench fluorescence in native iLOV and in GFPs that were engineered to have metal-binding ligands on their exterior.[65-67] Another intrinsic FP sensor that is sensitive to copper utilizes the metal-chelating ncAA L-DOPA. L-DOPA was incorporated into the chromophore of a green fluorescent protein to replace the tyrosine.[68] Hg^{2+} has been shown to induce turn-on fluorescence upon binding different FbFPs and GFPs, but it inhibits the fluorescence of IFP1.4 by blocking biliverdin binding.[69-71] Interestingly, IFP2.0 derived from IFP1.4 is sensitive to singlet oxygen as the ROS may also interrupt the biliverdin binding.[72] Another group of intrinsic FP sensors is based on the reaction between the chromophore and the analytes of interest. Chen et al. developed the first genetically encoded, reaction-based H_2S

sensor. The authors genetically modified the chromophore with the azide-containing structure. In the presence of H_2S, the azido functional group would be reduced to an amine-containing matured chromophore.[55] Based on the same idea, a reaction-based H_2S sensor was developed to further optimize the sensitivity, selectivity and dynamic range, while a sensor with ratiometric change has been recently developed to quantify the concentration of H_2S.[73, 74] A peroxynitrite ($ONOO^-$) sensor was developed based on the reaction between $ONOO^-$ and the boronic analog of the chromophore tyrosine.[56] The reaction-based sensors are relatively easy to develop in terms of design, and they are robust in monitoring the release of analytes. However, the major drawback is that reaction-based sensors are irreversible and thus cannot monitor the dynamics of the target of interest.

1.3.2.2 Conformational Change-based Single FP Sensors

Single FP sensors based on conformational change are FPs fused with the binding domain of the target. When the binding domain binds the target of interest, the conformational change modulates the solvent and oxygen accessibility of FPs fused with the binding domain. As a consequence, this changes the fluorescent intensities of the FPs (**Figure 4**). Depending on how the microenvironment surrounding the chromophore changes, these sensors can be either intensiometric (turn on or off) or ratiometric (excitation or emission spectra). There are two primary constructs of conformation-based, single FP sensors. In the first, a circular-permuted FP is inserted into one of the loops of the binding domain. In the second, the intact binding domain is fused into the loop of the FP that is adjacent to the chromophore. Conformation-based, single FP sensors have blossomed in the past two decades. This includes the most famous series of Ca^{2+} indicators

such as the GCaMP family (with the most recent GCaMP7) and the GECO family with optimizations in dynamic range, sensitivity, kinetics, and multiplex imaging.[75-79] Another broad family of conformation-based, single FP sensors is *Escherichia coli* periplasmic binding protein-based (PBP-based) sensors. Because the PBP family exhibits a massive conformational change between the apo and the bound state, it is an ideal family of targets for sensor engineering. Meanwhile, PBP families have been identified to bind a wide variety of ligands, including some crucial ligands that are involved in brain signaling and metabolism.[80] The most important of these is iGluSnFR and its variants.[81, 82]

Another rising family of genetically encoded sensors are G-protein coupled receptor-based (GPCR-based), single FP sensors (**Figure 4**). Although the idea of taking advantage of the conformational change at intracellular loop three can be dated to 2011,[47]

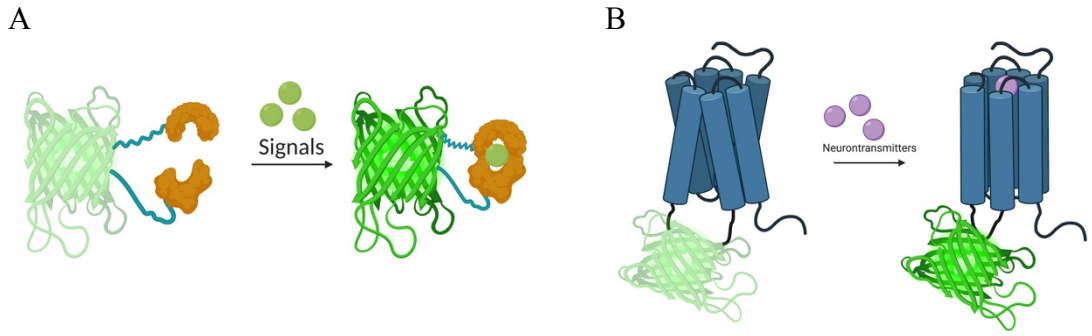

Figure 4. Two major platforms of single FP based sensors. A) cpGFP fused with sensing domains. B) cpGFP inserted into GPCR. The conformational change would lead to the change in microenvironment of the chromophore, resulting in the change in fluorescence intensity.

the FRET-based sensors have been suffering from low dynamic range and thus cannot be used for *in vivo* experiments. Recently, Li and Tian's labs have made dramatic progress on

GPCR-based, single FP sensors for acetylcholine and dopamine, and these sensors are robust in live-mouse imaging with fast kinetics and high dynamic ranges.[83-85]

1.4. ENGINEERING OF GENETICALLY ENCODED SENSORS

Single FPs and FRET sensors share some strategies in design and optimization. For most sensors in these two categories, the components include FP, binding domain, and linkers between different parts. Optimizing the length and components of linkers can be crucial. Saturation mutagenesis is often applied to create genetic libraries for the improvement of sensors. However, the two types of sensors have some major differences. One difference is the choice of FPs. In designing FRET sensors, the FP pair is determined by the spectral overlap between the emission spectra of the donor and the excitation spectra of the acceptor. An acceptor with better photoproperties is always preferable. In contrast, single FP sensors could be constructed from any FP, although the reality is that GFP and YFP are the fluorophores that are easy to engineer because they have better maturation efficiency, folding, and other photoproperties. In the red region of the spectrum, mApple, mRuby, mCherry, mOrange2, and mKeima also have been used as the fluorescent part of the sensors.[86-88]

For single FP sensors, a crucial characteristic that has to be optimized is the circular permutation site.[89] By rearranging the N' and C' terminus of FPs, the chromophore is more exposed to the microenvironment. While circular permutation for most of the FPs has been successful, the engineering of sensors also requires further optimization such as termini locations and linker composition. This requires a tremendous amount of work in library

construction and screening. Recently, a high-throughput method based on fluorescence-activated cell sorting (FACS) screening of insertion sites between binding domain and FPs was successful in the engineering of a sensor for maltose.[90] As is the case with other sensors, this method is likely to be useful in determining the termini locations.

1.5. EXAMPLES OF FEATURED SENSORS

Here briefly summarized are the genetically encoded sensors in the research field that is related to my thesis.

1.5.1 Ions/Metals

Ca^{2+} sensors are the most successful and extensively studied genetically encoded sensors because Ca^{2+} plays a crucial role in cell signaling. Hundreds of Ca^{2+} sensors that vary in emission wavelength, kinetics, and thermodynamic properties have been developed to achieve the goal of multicolor imaging, deep-tissue imaging, and other approaches. However, these sensors do share a similarity in Ca^{2+} binding motifs. Most Ca^{2+} sensors are composed of a C' terminus of calmodulin (CaM) and myosin light-chain kinase (M13) to induce conformational changes when Ca^{2+} is present. The CaM and M13 are most commonly fused with a FRET pair to engineer an intramolecular Ca^{2+} FRET sensor (Cameleon sensor series) or with a circularly-permuted FP to create a single FP-based Ca^{2+} sensor (GCaMP and GECO sensor series). These two platforms have been thoroughly engineered by many labs to improve photophysics, dynamic range and kinetics.[77, 87, 91-96] Other Ca^{2+}-binding domains have also been used to induce the conformational change of

cpFP, such as troponin C,[97, 98] RS20 and ckkap in place of M13.[99, 100]

Besides improving the sensitivity and dynamic range of Ca^{2+} sensors, researchers have been working to expand the palette as well.[78] A tremendous achievement is that Qian et al. have developed a near-infrared Ca^{2+} sensor based on mIFP, which significantly expanded the spectrum of genetically encoded Ca^{2+} sensors toward the near-infrared-shifted region.[100]

Meanwhile, there are intrinsic sensitivity FP sensors for Ca^{2+}, including CatchER, in which residues on the exterior of the GFP beta-barrel were mutated to bind Ca2+ and increase the intensity of fluorescence directly.[101]

Other than traditional Ca^{2+} sensors that try to monitor the Ca^{2+} dynamics with temporal and spatial resolutions in different organelles *in vivo*, there is one Ca^{2+} sensor with some intriguing innovations. By taking advantage of the photoconvertible FP, EOS (**Figure 5**), Fosque et al. were able to engineer a brand new type of Ca^{2+} sensor, named CAMPARI.[102] When Ca^{2+} is present, the irradiation of CAMPARI with blue light induces a permanent shift of fluorescence from green to red as a result of locking the Ca^{2+} signal in place. Recently, CAMPARI 2.0 has been engineered to be brighter and have a better conversion rate.[103]

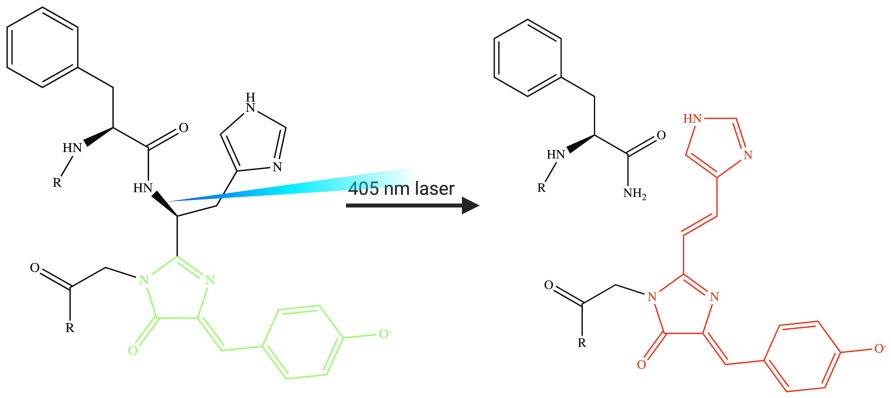

Figure 5. Photoconversion of EOS fluorescent protein family. The chromophore contains a tripeptide His62-Tyr63-Gly64 that initially emits green fluorescence. Irradiation using 405 nm laser induces cleavage between the amide nitrogen and alpha-carbon atom in the histidine residue, creating a highly conjugated system and resulting in the dramatic shift of fluorescence emission to red.

Many sensors for other biologically relevant ions have been engineered in similar designing strategies of genetically encoded Ca^{2+} sensors. FRET sensors composed of different binding motifs fused between a FRET pair have been engineered for Zn^{2+},[32, 104-107] Cu^{+},[108] Mg^{2+},[109] and K^{+}.[110, 111] Single fluorescent protein-based sensors also have been engineered to monitor the dynamics of Zn^{2+},[112-116] Cu^{+},[117] and K^{+}.[111]

Other than the conformational change triggered by the binding site of genetically encoded sensors, prototypical fluorescent proteins themselves also can be sensitive to some ions. Concentrated halide anions may penetrate the beta-barrel of fluorescent proteins and decrease the fluorescent intensity because of the increase of pKa.[64] Moreover, EYFP is sensitive to chloride and iodide, so it is further engineered into sensors to monitor inhibitory

synaptic activities.[118, 119]

Some unique methods have been developed to create metal ion sensors. Niraikulam et al. incorporated L-DOPA in place of L-tyrosine into GFP by genetic-code engineering to make the chromophore of GFP more sensitive to Cu^{2+}.[68]

The number of sensors made by introducing bioluminescent proteins into the construct is growing at a rapid pace, providing less background noise and better compatibility for *in vivo* imaging.

Work has been done to utilize luciferase, such as NanoLuc, to create genetically encoded bioluminescence resonance energy transfer (BRET) sensors for measuring intracellular Ca^{2+} and Zn^{2+}.[120, 121] The most successful BRET sensor is composed of an

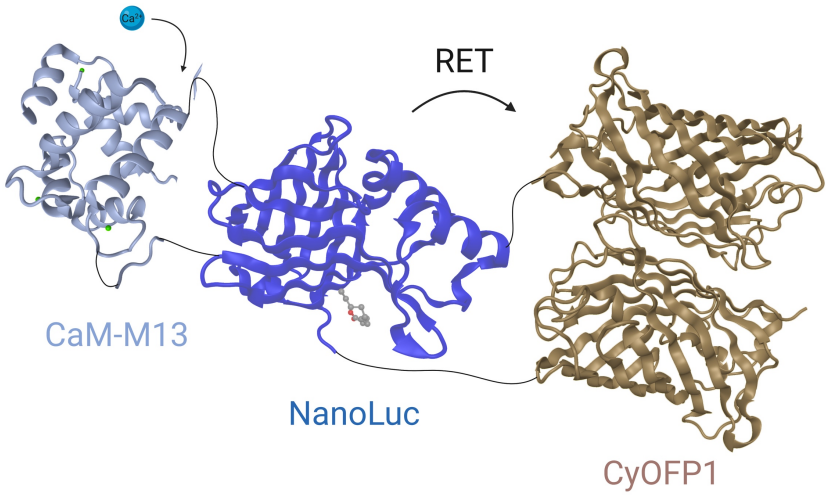

Figure 6. Model of Orange CaMBI in the Ca^{2+} bound state. CaM and M13 domains are fused with NanoLuc and two copies of CyOFP1. Binding of Ca^{2+} induces binding of CaM to M13, enhancing NanoLuc activity. RET to CyOFP1 shifts emission to orange and increase the fluorescence intensity.

orange calcium-modulated bioluminescent indicator fused with NanoLuc luciferase, CyOFP1, with the traditional calcium-binding motifs (**Figure 6**).[122]

1.5.2 pH

pH is crucial in regulating the homeostasis of any living cells. Many biological events undergo pH change, such as cell metabolites and signaling. In different cellular compartments, the range of pH may be significant. Early efforts to engineer genetically encoded pH sensors focused on the mutations of GFP to move pKa closer to the physiological range.[57, 59, 123] After successfully engineering GFP-based pH sensors, the spectrum of pH sensors has been expanded throughout the visible region.[124-128] Of all the genetically encoded pH sensors, the most sensitive red FP-based pH sensor is pHTomato, with a pKa of 7.8.[129] In pHTomato, six amino acids were mutated by random mutagenesis. Although pHTomato satisfies the need for higher pH sensitivity, this sensor exhibits only a 3-fold of change, which is approximately 50% of pHluorin.

1.5.3 Metabolites and Signaling

The survival of living creatures heavily depends on the metabolism of every cell and organelle. Much effort has been put into engineering a wide range of genetically encoded sensors for metabolites to develop such a sophisticated metabolism map.

Coupling FRET pairs with different enzymes has enabled the construction of genetically encoded sensors capable of monitoring the endogenous catalytic activity of phosphorylation, especially sensors for the signaling molecules cAMP and cGMP.[130-139] Worth mentioning is that some of the FRET-based sensors can be used for detection in

transgenic mice, providing a robust response upon stimulation.[140] Similar strategies have been used to engineer genetically encoded sensors for sugars,[141-144] amino acids,[145-150] ATP,[151, 152] and $NADP^+$.[153] Several single FP-based sensors have been engineered for kinase, ATP, NADH, NADPH, and GTP to achieve better signal-to-noise ratio and multicolor imaging of different analytes of interest.[154-159] Recently, Lobas et al. developed a genetically encoded ATP sensor whose binding affinity is more relevant to the physiological range and is able to detect the release of ATP in neurons.[160] With strategies similar to those mentioned above, some single FP-based sensors were able to monitor signals *in vivo*.[82, 161]

Another family of sensors has been developed to sense the mechanical and biochemical signals at the cell membrane, which can result in the activation of transcription factors.[162-166] Ting et al. presented the first three genetically encoded fluorescent reporters of the family for the kinases Src, Abl, and epidermal growth factor (EGF) receptor. These genetically encoded sensors consist of fusions of CFP, a phosphotyrosine binding domain; SH2, a consensus substrate for the relevant kinase; and YFP. Subsequent studies have mainly focused on modifying this classical construct to achieve the sensing of different molecules or to provide a better signal-to-noise ratio.

1.5.4 Redox

Almost all redox sensors function by the reversible oxidation of two cysteines to form a disulfide bond, thus changing the microenvironment of the chromophore of FPs. One primary design strategy is to mutate the residues close to the chromophore of FPs to cysteines. Under oxidative conditions, the cysteines form disulfide bonds with other

cysteines on the FP. The conformational change after forming disulfide bonds results in a change of fluorescent intensities. The first genetically encoded redox sensor based on the disulfide bond formation was developed in 2001.[167] Formation of a disulfide bond between the two cysteines induces a distortion of β-barrel that is fully reversible and results in a 50% decrease in the intrinsic fluorescence. Since 2001, the visible spectrum has been filled with redox sensors based on disulfide bond formation.[168-170] The formation of disulfide bonds may also be applied to the change in proximity of FRET pairs, increasing FRET efficiency upon oxidation.[171]

Other engineering strategies for redox sensors are to fuse the FPs with reaction domains containing cysteines. Oxidation of the cysteines leads to the conformational change of the reaction domain, thus changing fluorescence intensity or FRET efficiency.[172-176]

Most of these sensors are responsive to oxidizing and reducing agents, and they have primarily been used to sense H_2O_2 and oxidative stress. Similar approaches are used to detect a reduced and oxidized glutathione balance and to monitor thioredoxin dynamics.[177-181]

Because of the nature of reactive oxygen species, another unique way of sensing redox dynamics is to incorporate non-canonical amino acids (ncAAs) into FPs that can react with ROS, leading to the change of fluorescent intensity (**Figure 7**).[55, 56, 74]

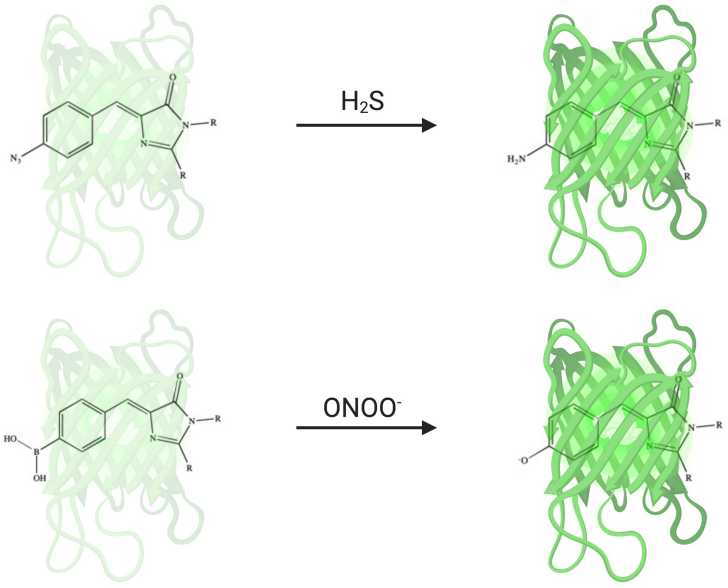

Figure 7. GFP chromophore substituted with ncAAs. FP chromophores are modified with the sulfide-reactive azide or ROS-reactive boronic functional group. These structurally modified chromophores were selectively reacted with H_2S or $ONOO^-$, resulting in sensitive fluorescence enhancement detectable by spectroscopic and microscopic techniques.

Recently, Eroglu et al. reported the development of novel multicolored fluorescent quenching-based probes for nitric oxide. By fusing a bacteria-derived binding domain close to the chromophore of FPs, the binding of nitric oxide results in the quench of the chromophore, triggering a decrease of the fluorescence intensity.[182]

1.5.5 Voltage

Voltage regulates almost every physiological condition in our nerves and muscles. Changes in membrane potential and polarity take place in every biological organ, tissues, and cells.

In living creatures, the two most abundant voltage-dependent conductances, Na^+

and K^+, are essential for electrical impulses in the central neuron system, known as the action potential. There are about 100 different variants of voltage-dependent channels for Na^+ and K^+ in the central neuron system. Previous studies on the ion channel were carried out using glass electrodes to measure electrical signals in cell membranes. The drawback of this strategy is that most axons in the central nervous system are too small to be measured with electrodes, losing the resolution of neurological study. Tremendous work has been put into developing genetically encoded voltage indicators (GEVIs) to monitor the dynamics of membrane potential.

To date, there are three major types of GEVI. The first type is the combination of a voltage-sensing domain (VSD) and cpFP. The first GEVI engineered by fusion of VSD and cpGFP, named FlaSh, exhibits a 5% fold of change with poor kinetics.[183] Five years later, Ataka et al. engineered SPARC, a GEVI with much faster kinetics.[184] Unfortunately, these initial sensors have weak membrane localization, so they could not be used in primary cultured neurons or brain slices.[185] To improve membrane localization, Murata et al. replaced the voltage indicator of voltage-gated K+ channels (Kvs) with a reaction domain of the Ciona intestinalis voltage-sensitive phosphatase (Ci-VSP). They were able to express it successfully in Ciona sperm tail membranes.[186] Since Ci-VSP was identified as a potential sensing domain for GEVI, researchers have developed two primary alterations of VSD-based GEVI. The first type is Arclight and its derivative, Bongwoori. They have the Ci-VSP fused to an intracellular super ecliptic pHluorin.[187, 188] Depolarization of the membrane would induce a conformational change in VSP, leading to changes in fluorescence intensity. Arclight and Bongwoori have high brightness but poor kinetics, making them suitable for detecting slight changes in voltage. The second type of sensors

are composed of circular-permuted FPs. The voltage-sensing domain is fused with cpFPs in a way that is much closer to the chromophore, resulting in more significant changes in fluorescence. ASAP1, a fusion construct of an extracellular cpGFP to the VSP of *Gallus gallus*, has much better kinetics and sensitivity compared to VSP-based sensors, including Arclight.[189]

By engineering the linker site of ASAP1 with one mutation and one deletion, A147S and ΔA148 respectively, the new sensor of the ASAP family, named ASAP2f, shows fluorescence changes about 14% bigger than the previous version.[190] Through further optimization, ASAP3 has enough speed and sensitivity to detect the individual voltage spike up to 100 Hz in acute brain slices.[191] Much effort has also been put into expanding the spectrum accessibility of GEVIs. A red-shifted variant, FlicR1, was created by fusing the Ci-VSP domain with cpmApple.[192]

The second type of GEVI is based on rhodopsin, which was first discovered in marine bacteria.[193] Rhodopsin is a voltage-dependent chromophore which features near-infrared fluorescence. The first rhodopsin-based sensor, PROPS, can detect electrical spikes in *E. Coli* at up to 1 Hz. Unfortunately, PROPS cannot be localized onto the membrane of eukaryotic cells.[194] By engineering archaerhodopsin, which is known to be targeted to cell membranes, Hochbaum et al. were able to develop QuasArs, which demonstrates rapid sub-millisecond kinetics and much better sensitivity than Arch.[195] Archon families were developed through engineering the opsin core of QuasAr2.[196] Archon1 shows increased brightness and improved sensitivity to detect subthreshold voltage events at only 5 mV, with a slight decline in kinetics.

Although rhodopsin-based GEVIs feature a shift toward longer wavelength, fast

kinetics, and robust response to changes in membrane potentials, one significant drawback for rhodopsin-based GEVIs is their low quantum efficiency, which makes them only ~3% as bright as GFP.[195]

Combining FPs and rhodopsin yields the third type of GEVI, FRET-opsin-based reporters. They retain the advantages of quantum efficiency from FPs and fast kinetics from rhodopsin. Fusing a rhodopsin variant from *Acetabularia acetabulum* (Ace2N) with mNeonGreen yielded a sensor with 1 ms response time and a 14% change in fluorescence intensity.[197] However, Ace2N-mNeon does not exhibit a robust response *in vivo*.[198] A new FRET-opsin-based GEVI, named VARNAM, can redshift the fluorescence by fusing Ace with mRuby3.[38]

Besides combining FPs with rhodopsin, there are some unique methods in the engineering of FRET-opsin-based GEVIs. Xu et al. created a hybrid GEVI using a site-specific modification of rhodopsin with organic fluorophores through click chemistry.[37] Unfortunately, because of the toxicity of the click reaction, they could not apply such indicators in neurons or brain slices. Another unique strategy of the FRET-opsin-based GEVI yielded an indicator named Voltron. It replaces the fluorescent protein FRET donor with a fluorescent dye mobilized by HaloTag. In the Voltron family, Voltron525 shows a sensitivity of about -23%,[199] which is the most sensitive GEVI to date.

1.5.6 Neurotransmitters

Neurotransmitters are essential chemicals that enable neuron communication. Mapping out the sophisticated neurological system requires real-time monitoring of neurotransmitters at the synaptic level. Early works focused on engineering FRET-based

sensors for neurotransmitters.[145, 200] However, such sensors are limited to cultured cells because of the low signal-to-noise ratio for *in vivo* imaging. Recently, genetically encoded neurotransmitter indicators with high resolution and specificity have been developed. These sensors can be divided into two major groups: those based on binding proteins and those based on G-protein-coupled receptors (GPCRs).

Binding proteins of several neurotransmitters can be found in bacteria and other living creatures. Among them, bacterial periplasmic binding proteins (PBPs) are the most widely used for engineering neurotransmitter sensors. The PBP family shares similarity in structure and significant conformational change upon binding with the analyte of interest.[80] By fusing PBPs and cpFP, sensors with high dynamic ranges have been developed for glutamate,[82, 161] GABA,[201] acetylcholine,[202] and nicotine.[203]

Recently, a new type of sensors based on GPCR has drawn great attention. GPCRs belong to a large superfamily of membrane proteins. Although each GPCR has different functions, they are highly conserved in terms of 3D structures.[204] The structure of a GPCR has three parts: (1) the extracellular region, consisting of the N-terminus and three extracellular loops; (2) the TM region, composed of seven α-helices; and (3) the intracellular region, consisting of three intracellular loops. When the ligands bind with the binding pocket of the TM region, the conformational change leads to a change in the fluorescence intensity of cpFP fused with the GPCR.

In 2018, Patriarchi et al. developed the dLight series, the first reported genetically encoded sensors for detecting and imaging dopamine in live animals based on the fusion of GPCR and cpFP.[84] The dLight series exhibits fast kinetics (10 ms on and 100 ms off) and a broad dynamic range, enabling the detection of individual and subthreshold release

of dopamine *in vivo*. In addition, Sun et al. created a family of genetically encoded dopamine sensors using a similar strategy.[85] These sensors also exhibit high magnitudes of fluorescent responses, but they are slower in kinetics (130 ms on and 2.5 s off).

Besides a dopamine sensor based on GPCR, Li's lab has developed sensors for acetylcholine and NE using similar strategies.[205, 206]

There are many excellent reviews of genetically encoded indicators. For the most comprehensive and up-to-date review, please refer to the work of Greenwald et al.[207]

1.6. SUMMARY

While genetically encoded biosensors, such as calmodulin–M13 based Ca^{2+} sensors [87, 208, 209] have proven useful for studying biological processes *in vivo*, there are several areas in which genetically encoded biosensor-based fluorescence imaging is highly desirable yet lags far behind. First is the achievement of multiplexed sensor imaging. Signaling networks in living creatures are full of complexity and connectivity, often involved with several different pathways. The ability to monitor multiple activities simultaneously would, therefore, be tremendously useful for understanding these sophisticated networks. Multiplexed sensor imaging requires expanded types as well as palette of sensors, while a variety of biosensors with specific binding affinity and different fluorescence wavelengths are yet to be developed. Second is to apply genetically encoded sensors to more complex biological systems. To date, a majority of the sensors developed for fluorescence imaging have utilized genetically encoded biosensors in *ex vivo* settings. It is crucial to apply fluorescent biosensors to monitor cellular processes *in vivo*, which can

provide a better understanding of signaling under physiological conditions. To achieve that, fluorescent biosensors have to overcome several challenges, such as absorption and scattering of the light source and fluorescence signal, autofluorescence from endogenous cellular components, photobleaching of the fluorescent biosensor, and phototoxicity in live fluorescence microscopy. As aforementioned, mammalian cells and tissues exhibit much less absorption and scattering of light in the near-infrared region, FPs that are excited and emit in this spectral range would be much favored in live animal imaging. Therefore, this thesis is focused on the development of genetically encoded sensors on a new target of interest, serotonin; application of fluorescent biosensors to more complex biological systems, such as brain tissues and islets; and expanding the fluorescent biosensors in the redder region of the spectrum.

REFERENCES

1. Chudakov, D. M.; Matz, M. V.; Lukyanov, S.; Lukyanov, K. A., Fluorescent proteins and their applications in imaging living cells and tissues. Physiological reviews **2010,** 90 (3), 1103-63.
2. Pédelacq, J.-D.; Cabantous, S.; Tran, T.; Terwilliger, T. C.; Waldo, G. S., Engineering and characterization of a superfolder green fluorescent protein. Nature Biotechnology **2006,** 24 (1), 79-88.
3. Ai, H.-w.; Shaner, N. C.; Cheng, Z.; Tsien, R. Y.; Campbell, R. E., Exploration of New Chromophore Structures Leads to the Identification of Improved Blue Fluorescent Proteins. Biochemistry **2007,** 46 (20), 5904-5910.
4. Heim, R.; Prasher, D. C.; Tsien, R. Y., Wavelength mutations and posttranslational autoxidation of green fluorescent protein. Proceedings of the National Academy of Sciences **1994,** 91 (26), 12501.
5. Kremers, G.-J.; Goedhart, J.; van Munster, E. B.; Gadella, T. W. J., Cyan and Yellow Super Fluorescent Proteins with Improved Brightness, Protein Folding, and FRET Förster Radius. Biochemistry **2006,** 45 (21), 6570-6580.
6. Chu, J.; Haynes, R. D.; Corbel, S. Y.; Li, P.; González-González, E.; Burg, J. S.; Ataie, N. J.; Lam, A. J.; Cranfill, P. J.; Baird, M. A.; Davidson, M. W.; Ng, H.-L.;

Garcia, K. C.; Contag, C. H.; Shen, K.; Blau, H. M.; Lin, M. Z., Non-invasive intravital imaging of cellular differentiation with a bright red-excitable fluorescent protein. Nature methods **2014,** 11 (5), 572-578.
7. Chu, J.; Oh, Y.; Sens, A.; Ataie, N.; Dana, H.; Macklin, J. J.; Laviv, T.; Welf, E. S.; Dean, K. M.; Zhang, F.; Kim, B. B.; Tang, C. T.; Hu, M.; Baird, M. A.; Davidson, M. W.; Kay, M. A.; Fiolka, R.; Yasuda, R.; Kim, D. S.; Ng, H.-L.; Lin, M. Z., A bright cyan-excitable orange fluorescent protein facilitates dual-emission microscopy and enhances bioluminescence imaging in vivo. Nature Biotechnology **2016,** 34 (7), 760-767.
8. Bajar, B. T.; Lam, A. J.; Badiee, R. K.; Oh, Y.-H.; Chu, J.; Zhou, X. X.; Kim, N.; Kim, B. B.; Chung, M.; Yablonovitch, A. L.; Cruz, B. F.; Kulalert, K.; Tao, J. J.; Meyer, T.; Su, X.-D.; Lin, M. Z., Fluorescent indicators for simultaneous reporting of all four cell cycle phases. Nature methods **2016,** 13 (12), 993-996.
9. Costantini, L. M.; Snapp, E. L., Fluorescent Proteins in Cellular Organelles: Serious Pitfalls and Some Solutions. DNA and Cell Biology **2013,** 32 (11), 622-627.
10. Costantini, L. M.; Baloban, M.; Markwardt, M. L.; Rizzo, M.; Guo, F.; Verkhusha, V. V.; Snapp, E. L., A palette of fluorescent proteins optimized for diverse cellular environments. Nature communications **2015,** 6, 7670.
11. Tomosugi, W.; Matsuda, T.; Tani, T.; Nemoto, T.; Kotera, I.; Saito, K.; Horikawa, K.; Nagai, T., An ultramarine fluorescent protein with increased photostability and pH insensitivity. Nature methods **2009,** 6, 351.
12. Shinoda, H.; Ma, Y.; Nakashima, R.; Sakurai, K.; Matsuda, T.; Nagai, T., Acid-Tolerant Monomeric GFP from Olindias formosa. Cell chemical biology **2018,** 25 (3), 330-338.e7.
13. Fan, L. Z.; Lin, M. Z., Optical control of biological processes by light-switchable proteins. Wiley interdisciplinary reviews. Developmental biology **2015,** 4 (5), 545-54.
14. Chapman, S.; Faulkner, C.; Kaiserli, E.; Garcia-Mata, C.; Savenkov, E. I.; Roberts, A. G.; Oparka, K. J.; Christie, J. M., The photoreversible fluorescent protein iLOV outperforms GFP as a reporter of plant virus infection. Proceedings of the National Academy of Sciences **2008,** 105 (50), 20038.
15. Drepper, T.; Eggert, T.; Circolone, F.; Heck, A.; Krauß, U.; Guterl, J.-K.; Wendorff, M.; Losi, A.; Gärtner, W.; Jaeger, K.-E., Reporter proteins for in vivo fluorescence without oxygen. Nature Biotechnology **2007,** 25, 443.
16. Christie, J. M.; Hitomi, K.; Arvai, A. S.; Hartfield, K. A.; Mettlen, M.; Pratt, A. J.; Tainer, J. A.; Getzoff, E. D., Structural tuning of the fluorescent protein iLOV for improved photostability. The Journal of biological chemistry **2012,** 287 (26), 22295-304.
17. Buckley, A. M.; Jukes, C.; Candlish, D.; Irvine, J. J.; Spencer, J.; Fagan, R. P.; Roe, A. J.; Christie, J. M.; Fairweather, N. F.; Douce, G. R., Lighting Up Clostridium Difficile: Reporting Gene Expression Using Fluorescent Lov Domains. Scientific Reports **2016,** 6, 23463.
18. Shu, X.; Lev-Ram, V.; Deerinck, T. J.; Qi, Y.; Ramko, E. B.; Davidson, M. W.; Jin, Y.; Ellisman, M. H.; Tsien, R. Y., A genetically encoded tag for correlated light and electron microscopy of intact cells, tissues, and organisms. PLoS biology **2011,** 9 (4), e1001041.
19. Hayashi, S.; Toda, Y., A novel fluorescent protein purified from eel muscle. Fisheries Science **2009,** 75 (6), 1461.

20. Kumagai, A.; Ando, R.; Miyatake, H.; Greimel, P.; Kobayashi, T.; Hirabayashi, Y.; Shimogori, T.; Miyawaki, A., A bilirubin-inducible fluorescent protein from eel muscle. Cell **2013,** 153 (7), 1602-11.
21. Wagner, J. R.; Zhang, J.; von Stetten, D.; Gunther, M.; Murgida, D. H.; Mroginski, M. A.; Walker, J. M.; Forest, K. T.; Hildebrandt, P.; Vierstra, R. D., Mutational analysis of Deinococcus radiodurans bacteriophytochrome reveals key amino acids necessary for the photochromicity and proton exchange cycle of phytochromes. The Journal of biological chemistry **2008,** 283 (18), 12212-26.
22. Shu, X.; Royant, A.; Lin, M. Z.; Aguilera, T. A.; Lev-Ram, V.; Steinbach, P. A.; Tsien, R. Y., Mammalian Expression of Infrared Fluorescent Proteins Engineered from a Bacterial Phytochrome. Science **2009,** 324 (5928), 804.
23. Filonov, G. S.; Piatkevich, K. D.; Ting, L.-M.; Zhang, J.; Kim, K.; Verkhusha, V. V., Bright and stable near-infrared fluorescent protein for in vivo imaging. Nature Biotechnology **2011,** 29, 757.
24. Yu, D.; Gustafson, W. C.; Han, C.; Lafaye, C.; Noirclerc-Savoye, M.; Ge, W.-P.; Thayer, D. A.; Huang, H.; Kornberg, T. B.; Royant, A.; Jan, L. Y.; Jan, Y. N.; Weiss, W. A.; Shu, X., An improved monomeric infrared fluorescent protein for neuronal and tumour brain imaging. Nature communications **2014,** 5, 3626.
25. Yu, D.; Baird, M. A.; Allen, J. R.; Howe, E. S.; Klassen, M. P.; Reade, A.; Makhijani, K.; Song, Y.; Liu, S.; Murthy, Z.; Zhang, S.-Q.; Weiner, O. D.; Kornberg, T. B.; Jan, Y.-N.; Davidson, M. W.; Shu, X., A naturally monomeric infrared fluorescent protein for protein labeling in vivo. Nature methods **2015,** 12, 763.
26. Rodriguez, E. A.; Tran, G. N.; Gross, L. A.; Crisp, J. L.; Shu, X.; Lin, J. Y.; Tsien, R. Y., A far-red fluorescent protein evolved from a cyanobacterial phycobiliprotein. Nature methods **2016,** 13, 763.
27. Birkner, A.; Tischbirek, C. H.; Konnerth, A., Improved deep two-photon calcium imaging in vivo. Cell Calcium **2017,** 64, 29-35.
28. Mo, G. C. H.; Ross, B.; Hertel, F.; Manna, P.; Yang, X.; Greenwald, E.; Booth, C.; Plummer, A. M.; Tenner, B.; Chen, Z.; Wang, Y.; Kennedy, E. J.; Cole, P. A.; Fleming, K. G.; Palmer, A.; Jimenez, R.; Xiao, J.; Dedecker, P.; Zhang, J., Genetically encoded biosensors for visualizing live-cell biochemical activity at super-resolution. Nature methods **2017,** 14, 427.
29. Bindels, D. S.; Haarbosch, L.; van Weeren, L.; Postma, M.; Wiese, K. E.; Mastop, M.; Aumonier, S.; Gotthard, G.; Royant, A.; Hink, M. A.; Gadella Jr, T. W. J., mScarlet: a bright monomeric red fluorescent protein for cellular imaging. Nature methods **2016,** 14, 53.
30. Miyawaki, A.; Llopis, J.; Heim, R.; McCaffery, J. M.; Adams, J. A.; Ikura, M.; Tsien, R. Y., Fluorescent indicators for Ca2+based on green fluorescent proteins and calmodulin. Nature **1997,** 388 (6645), 882-887.
31. Hires, S. A.; Zhu, Y.; Tsien, R. Y., Optical measurement of synaptic glutamate spillover and reuptake by linker optimized glutamate-sensitive fluorescent reporters. Proceedings of the National Academy of Sciences **2008,** 105 (11), 4411.
32. Vinkenborg, J. L.; Nicolson, T. J.; Bellomo, E. A.; Koay, M. S.; Rutter, G. A.; Merkx, M., Genetically encoded FRET sensors to monitor intracellular Zn2+ homeostasis. Nature methods **2009,** 6, 737.

33. Hessels, A. M.; Chabosseau, P.; Bakker, M. H.; Engelen, W.; Rutter, G. A.; Taylor, K. M.; Merkx, M., eZinCh-2: A Versatile, Genetically Encoded FRET Sensor for Cytosolic and Intraorganelle Zn2+ Imaging. ACS Chemical Biology **2015,** 10 (9), 2126-2134.
34. Gong, Y.; Huang, C.; Li, J. Z.; Grewe, B. F.; Zhang, Y.; Eismann, S.; Schnitzer, M. J., High-speed recording of neural spikes in awake mice and flies with a fluorescent voltage sensor. Science **2015,** 350 (6266), 1361.
35. Gong, Y.; Wagner, M. J.; Zhong Li, J.; Schnitzer, M. J., Imaging neural spiking in brain tissue using FRET-opsin protein voltage sensors. Nature communications **2014,** 5, 3674.
36. Zou, P.; Zhao, Y.; Douglass, A. D.; Hochbaum, D. R.; Brinks, D.; Werley, C. A.; Harrison, D. J.; Campbell, R. E.; Cohen, A. E., Bright and fast multicoloured voltage reporters via electrochromic FRET. Nature communications **2014,** 5, 4625.
37. Xu, Y.; Peng, L.; Wang, S.; Wang, A.; Ma, R.; Zhou, Y.; Yang, J.; Sun, D.-e.; Lin, W.; Chen, X.; Zou, P., Hybrid Indicators for Fast and Sensitive Voltage Imaging. Angewandte Chemie International Edition **2018,** 57 (15), 3949-3953.
38. Kannan, M.; Vasan, G.; Huang, C.; Haziza, S.; Li, J. Z.; Inan, H.; Schnitzer, M. J.; Pieribone, V. A., Fast, in vivo voltage imaging using a red fluorescent indicator. Nature methods **2018,** 15 (12), 1108-1116.
39. Komatsu, N.; Aoki, K.; Yamada, M.; Yukinaga, H.; Fujita, Y.; Kamioka, Y.; Matsuda, M., Development of an optimized backbone of FRET biosensors for kinases and GTPases. Molecular Biology of the Cell **2011,** 22 (23), 4647-4656.
40. Ouyang, M.; Sun, J.; Chien, S.; Wang, Y., Determination of hierarchical relationship of Src and Rac at subcellular locations with FRET biosensors. Proceedings of the National Academy of Sciences **2008,** 105 (38), 14353.
41. Neininger, A.; Thielemann, H.; Gaestel, M., FRET-based detection of different conformations of MK2. EMBO reports **2001,** 2 (8), 703.
42. Kawai, Y.; Sato, M.; Umezawa, Y., Single Color Fluorescent Indicators of Protein Phosphorylation for Multicolor Imaging of Intracellular Signal Flow Dynamics. Analytical Chemistry **2004,** 76 (20), 6144-6149.
43. Tsou, P.; Zheng, B.; Hsu, C.-H.; Sasaki, Atsuo T.; Cantley, Lewis C., A Fluorescent Reporter of AMPK Activity and Cellular Energy Stress. Cell Metabolism **2011,** 13 (4), 476-486.
44. Yoshizaki, H.; Mochizuki, N.; Gotoh, Y.; Matsuda, M., Akt–PDK1 Complex Mediates Epidermal Growth Factor-induced Membrane Protrusion through Ral Activation. Molecular Biology of the Cell **2006,** 18 (1), 119-128.
45. Depry, C.; Mehta, S.; Li, R.; Zhang, J., Visualization of Compartmentalized Kinase Activity Dynamics Using Adaptable BimKARs. Chemistry & Biology **2015,** 22 (11), 1470-1479.
46. van Unen, J.; Stumpf, A. D.; Schmid, B.; Reinhard, N. R.; Hordijk, P. L.; Hoffmann, C.; Gadella, T. W., Jr.; Goedhart, J., A New Generation of FRET Sensors for Robust Measurement of Galphai1, Galphai2 and Galphai3 Activation Kinetics in Single Cells. PloS one **2016,** 11 (1), e0146789.

47. Ziegler, N.; Batz, J.; Zabel, U.; Lohse, M. J.; Hoffmann, C., FRET-based sensors for the human M1-, M3-, and M5-acetylcholine receptors. Bioorganic & medicinal chemistry **2011,** 19 (3), 1048-54.
48. Markovic, D.; Holdich, J.; Al-Sabah, S.; Mistry, R.; Krasel, C.; Mahaut-Smith, M. P.; Challiss, R. A., FRET-based detection of M1 muscarinic acetylcholine receptor activation by orthosteric and allosteric agonists. PloS one **2012,** 7 (1), e29946.
49. Köhnke, M.; Schmitt, S.; Ariotti, N.; Piggott, Andrew M.; Parton, Robert G.; Lacey, E.; Capon, Robert J.; Alexandrov, K.; Abankwa, D., Design and Application of In Vivo FRET Biosensors to Identify Protein Prenylation and Nanoclustering Inhibitors. Chemistry & Biology **2012,** 19 (7), 866-874.
50. Najumudeen, A. K.; Kohnke, M.; Solman, M.; Alexandrov, K.; Abankwa, D., Cellular FRET-Biosensors to Detect Membrane Targeting Inhibitors of N-Myristoylated Proteins. PloS one **2013,** 8 (6), e66425.
51. Zlobovskaya, O. A.; Sergeeva, T. F.; Shirmanova, M. V.; Dudenkova, V. V.; Sharonov, G. V.; Zagaynova, E. V.; Lukyanov, K. A., Genetically encoded far-red fluorescent sensors for caspase-3 activity. BioTechniques **2016,** 60 (2), 62-68.
52. Cameron, W. D.; Bui, C. V.; Hutchinson, A.; Loppnau, P.; Gräslund, S.; Rocheleau, J. V., Apollo-NADP+: a spectrally tunable family of genetically encoded sensors for NADP+. Nature methods **2016,** 13, 352.
53. Hoff, K. G.; Goodlitt, R.; Li, R.; Smolke, C. D.; Silberg, J. J., Fluorescence Detection of a Protein-Bound 2Fe2S Cluster. Chembiochem : a European journal of chemical biology **2009,** 10 (4), 667-670.
54. Warren, C. S.; Margineanu, A.; Katan, M.; Dunsby, C.; French, M. P., Homo-FRET Based Biosensors and Their Application to Multiplexed Imaging of Signalling Events in Live Cells. International Journal of Molecular Sciences **2015,** 16 (7).
55. Chen, S.; Chen, Z.-j.; Ren, W.; Ai, H.-w., Reaction-Based Genetically Encoded Fluorescent Hydrogen Sulfide Sensors. Journal of the American Chemical Society **2012,** 134 (23), 9589-9592.
56. Chen, Z.-j.; Ren, W.; Wright, Q. E.; Ai, H.-w., Genetically Encoded Fluorescent Probe for the Selective Detection of Peroxynitrite. Journal of the American Chemical Society **2013,** 135 (40), 14940-14943.
57. Kneen, M.; Farinas, J.; Li, Y.; Verkman, A. S., Green Fluorescent Protein as a Noninvasive Intracellular pH Indicator. Biophysical Journal **1998,** 74 (3), 1591-1599.
58. Llopis, J.; McCaffery, J. M.; Miyawaki, A.; Farquhar, M. G.; Tsien, R. Y., Measurement of cytosolic, mitochondrial, and Golgi pH in single living cells with green fluorescent proteins. Proceedings of the National Academy of Sciences **1998,** 95 (12), 6803.
59. Miesenböck, G.; De Angelis, D. A.; Rothman, J. E., Visualizing secretion and synaptic transmission with pH-sensitive green fluorescent proteins. Nature **1998,** 394 (6689), 192-195.
60. Li, Y.; Tsien, R. W., pHTomato, a red, genetically encoded indicator that enables multiplex interrogation of synaptic activity. Nature Neuroscience **2012,** 15, 1047.
61. Hanson, G. T.; McAnaney, T. B.; Park, E. S.; Rendell, M. E. P.; Yarbrough, D. K.; Chu, S.; Xi, L.; Boxer, S. G.; Montrose, M. H.; Remington, S. J., Green Fluorescent

Protein Variants as Ratiometric Dual Emission pH Sensors. 1. Structural Characterization and Preliminary Application. Biochemistry **2002,** 41 (52), 15477-15488.
62. Mahon, M. J., pHluorin2: an enhanced, ratiometric, pH-sensitive green florescent protein. Advances in bioscience and biotechnology (Print) **2011,** 2 (3), 132-137.
63. Poburko, D.; Santo-Domingo, J.; Demaurex, N., Dynamic Regulation of the Mitochondrial Proton Gradient during Cytosolic Calcium Elevations. Journal of Biological Chemistry **2011,** 286 (13), 11672-11684.
64. Wachter, R. M.; Yarbrough, D.; Kallio, K.; Remington, S. J., Crystallographic and energetic analysis of binding of selected anions to the yellow variants of green fluorescent protein11Edited by D. C. Rees. Journal of Molecular Biology **2000,** 301 (1), 157-171.
65. Lei, C.; Wang, Z.; Nie, Z.; Deng, H.; Hu, H.; Huang, Y.; Yao, S., Resurfaced Fluorescent Protein as a Sensing Platform for Label-Free Detection of Copper(II) Ion and Acetylcholinesterase Activity. Analytical Chemistry **2015,** 87 (3), 1974-1980.
66. Ravikumar, Y.; Nadarajan, S. P.; Lee, C. S.; Rhee, J. K.; Yun, H. D., A New-Generation Fluorescent-Based Metal Sensor - iLOV Protein. Journal of microbiology and biotechnology **2015,** 25 (4), 503-10.
67. Yu, X.; Strub, M.-P.; Barnard, T. J.; Noinaj, N.; Piszczek, G.; Buchanan, S. K.; Taraska, J. W., An engineered palette of metal ion quenchable fluorescent proteins. PloS one **2014,** 9 (4), e95808-e95808.
68. Ayyadurai, N.; Saravanan Prabhu, N.; Deepankumar, K.; Lee, S.-G.; Jeong, H.-H.; Lee, C.-S.; Yun, H., Development of a Selective, Sensitive, and Reversible Biosensor by the Genetic Incorporation of a Metal-Binding Site into Green Fluorescent Protein. Angewandte Chemie International Edition **2011,** 50 (29), 6534-6537.
69. Gu, Z.; Zhao, M.; Sheng, Y.; Bentolila, L. A.; Tang, Y., Detection of Mercury Ion by Infrared Fluorescent Protein and Its Hydrogel-Based Paper Assay. Analytical Chemistry **2011,** 83 (6), 2324-2329.
70. Jiang, T.; Guo, D.; Wang, Q.; Wu, X.; Li, Z.; Zheng, Z.; Yin, B.; Xia, L.; Tang, J.; Luo, W.; Xia, N.; Jiang, Y., Developing a genetically encoded green fluorescent protein mutant for sensitive light-up fluorescent sensing and cellular imaging of Hg(II). Analytica Chimica Acta **2015,** 876, 77-82.
71. Ravikumar, Y.; Nadarajan, S. P.; Lee, C. S.; Jung, S.; Bae, D. H.; Yun, H., FMN-Based Fluorescent Proteins as Heavy Metal Sensors Against Mercury Ions. Journal of microbiology and biotechnology **2016,** 26 (3), 530-9.
72. To, T.-L.; Fadul, M. J.; Shu, X., Singlet oxygen triplet energy transfer-based imaging technology for mapping protein–protein proximity in intact cells. Nature communications **2014,** 5, 4072.
73. Chen, Z.-j.; Ai, H.-w., A Highly Responsive and Selective Fluorescent Probe for Imaging Physiological Hydrogen Sulfide. Biochemistry **2014,** 53 (37), 5966-5974.
74. Youssef, S.; Zhang, S.; Ai, H.-w., A Genetically Encoded, Ratiometric Fluorescent Biosensor for Hydrogen Sulfide. ACS sensors **2019**.
75. Nagai, T.; Sawano, A.; Park, E. S.; Miyawaki, A., Circularly permuted green fluorescent proteins engineered to sense Ca2+. Proceedings of the National Academy of Sciences of the United States of America **2001,** 98 (6), 3197-202.
76. Nakai, J.; Ohkura, M.; Imoto, K., A high signal-to-noise Ca2+ probe composed of a single green fluorescent protein. Nature Biotechnology **2001,** 19 (2), 137-141.

77. Dana, H.; Sun, Y.; Mohar, B.; Hulse, B. K.; Kerlin, A. M.; Hasseman, J. P.; Tsegaye, G.; Tsang, A.; Wong, A.; Patel, R.; Macklin, J. J.; Chen, Y.; Konnerth, A.; Jayaraman, V.; Looger, L. L.; Schreiter, E. R.; Svoboda, K.; Kim, D. S., High-performance calcium sensors for imaging activity in neuronal populations and microcompartments. Nature methods **2019**.
78. Zhao, Y.; Araki, S.; Wu, J.; Teramoto, T.; Chang, Y. F.; Nakano, M.; Abdelfattah, A. S.; Fujiwara, M.; Ishihara, T.; Nagai, T.; Campbell, R. E., An expanded palette of genetically encoded Ca(2)(+) indicators. Science **2011,** 333 (6051), 1888-91.
79. Qian, Y.; Piatkevich, K. D.; Mc Larney, B.; Abdelfattah, A. S.; Mehta, S.; Murdock, M. H.; Gottschalk, S.; Molina, R. S.; Zhang, W.; Chen, Y.; Wu, J.; Drobizhev, M.; Hughes, T. E.; Zhang, J.; Schreiter, E. R.; Shoham, S.; Razansky, D.; Boyden, E. S.; Campbell, R. E., A genetically encoded near-infrared fluorescent calcium ion indicator. Nature methods **2019,** 16 (2), 171-174.
80. Dwyer, M. A.; Hellinga, H. W., Periplasmic binding proteins: a versatile superfamily for protein engineering. Current Opinion in Structural Biology **2004,** 14 (4), 495-504.
81. Marvin, J. S.; Borghuis, B. G.; Tian, L.; Cichon, J.; Harnett, M. T.; Akerboom, J.; Gordus, A.; Renninger, S. L.; Chen, T.-W.; Bargmann, C. I.; Orger, M. B.; Schreiter, E. R.; Demb, J. B.; Gan, W.-B.; Hires, S. A.; Looger, L. L., An optimized fluorescent probe for visualizing glutamate neurotransmission. Nature methods **2013,** 10, 162.
82. Marvin, J. S.; Scholl, B.; Wilson, D. E.; Podgorski, K.; Kazemipour, A.; Müller, J. A.; Schoch, S.; Quiroz, F. J. U.; Rebola, N.; Bao, H.; Little, J. P.; Tkachuk, A. N.; Cai, E.; Hantman, A. W.; Wang, S. S. H.; DePiero, V. J.; Borghuis, B. G.; Chapman, E. R.; Dietrich, D.; DiGregorio, D. A.; Fitzpatrick, D.; Looger, L. L., Stability, affinity, and chromatic variants of the glutamate sensor iGluSnFR. Nature methods **2018,** 15 (11), 936-939.
83. Jing, M.; Zhang, P.; Wang, G.; Feng, J.; Mesik, L.; Zeng, J.; Jiang, H.; Wang, S.; Looby, J. C.; Guagliardo, N. A.; Langma, L. W.; Lu, J.; Zuo, Y.; Talmage, D. A.; Role, L. W.; Barrett, P. Q.; Zhang, L. I.; Luo, M.; Song, Y.; Zhu, J. J.; Li, Y., A genetically encoded fluorescent acetylcholine indicator for in vitro and in vivo studies. Nature Biotechnology **2018,** 36, 726.
84. Patriarchi, T.; Cho, J. R.; Merten, K.; Howe, M. W.; Marley, A.; Xiong, W.-H.; Folk, R. W.; Broussard, G. J.; Liang, R.; Jang, M. J.; Zhong, H.; Dombeck, D.; von Zastrow, M.; Nimmerjahn, A.; Gradinaru, V.; Williams, J. T.; Tian, L., Ultrafast neuronal imaging of dopamine dynamics with designed genetically encoded sensors. Science **2018,** 360 (6396), eaat4422.
85. Sun, F.; Zeng, J.; Jing, M.; Zhou, J.; Feng, J.; Owen, S. F.; Luo, Y.; Li, F.; Wang, H.; Yamaguchi, T.; Yong, Z.; Gao, Y.; Peng, W.; Wang, L.; Zhang, S.; Du, J.; Lin, D.; Xu, M.; Kreitzer, A. C.; Cui, G.; Li, Y., A Genetically Encoded Fluorescent Sensor Enables Rapid and Specific Detection of Dopamine in Flies, Fish, and Mice. Cell **2018,** 174 (2), 481-496.e19.
86. Carlson, H. J.; Campbell, R. E., Circular permutated red fluorescent proteins and calcium ion indicators based on mCherry. Protein Engineering, Design and Selection **2013,** 26 (12), 763-772.

87. Dana, H.; Mohar, B.; Sun, Y.; Narayan, S.; Gordus, A.; Hasseman, J. P.; Tsegaye, G.; Holt, G. T.; Hu, A.; Walpita, D.; Patel, R.; Macklin, J. J.; Bargmann, C. I.; Ahrens, M. B.; Schreiter, E. R.; Jayaraman, V.; Looger, L. L.; Svoboda, K.; Kim, D. S., Sensitive red protein calcium indicators for imaging neural activity. eLife **2016,** 5, e12727.
88. Tantama, M.; Hung, Y. P.; Yellen, G., Imaging Intracellular pH in Live Cells with a Genetically Encoded Red Fluorescent Protein Sensor. Journal of the American Chemical Society **2011,** 133 (26), 10034-10037.
89. Baird, G. S.; Zacharias, D. A.; Tsien, R. Y., Circular permutation and receptor insertion within green fluorescent proteins. Proceedings of the National Academy of Sciences **1999,** 96 (20), 11241.
90. Nadler, D. C.; Morgan, S.-A.; Flamholz, A.; Kortright, K. E.; Savage, D. F., Rapid construction of metabolite biosensors using domain-insertion profiling. Nature communications **2016,** 7, 12266.
91. Badura, A.; Sun, X. R.; Giovannucci, A.; Lynch, L. A.; Wang, S. S. H., Fast calcium sensor proteins for monitoring neural activity. Neurophotonics **2014,** 1 (2), 025008-025008.
92. Choi, W.-G.; Swanson, S. J.; Gilroy, S., High-resolution imaging of Ca2+, redox status, ROS and pH using GFP biosensors. The Plant Journal **2012,** 70 (1), 118-128.
93. Suzuki, J.; Kanemaru, K.; Iino, M., Genetically Encoded Fluorescent Indicators for Organellar Calcium Imaging. Biophysical Journal **2016,** 111 (6), 1119-1131.
94. Waldeck-Weiermair, M.; Bischof, H.; Blass, S.; Deak, A. T.; Klec, C.; Graier, T.; Roller, C.; Rost, R.; Eroglu, E.; Gottschalk, B.; Hofmann, N. A.; Graier, W. F.; Malli, R., Generation of Red-Shifted Cameleons for Imaging Ca^{2+} Dynamics of the Endoplasmic Reticulum. Sensors (Basel, Switzerland) **2015,** 15 (6), 13052-13068.
95. Wu, J.; Prole, D. L.; Shen, Y.; Lin, Z.; Gnanasekaran, A.; Liu, Y.; Chen, L.; Zhou, H.; Chen, S. R. W.; Usachev, Y. M.; Taylor, C. W.; Campbell, R. E., Red fluorescent genetically encoded Ca2+ indicators for use in mitochondria and endoplasmic reticulum. Biochem J **2014,** 464 (1), 13-22.
96. Inoue, M.; Takeuchi, A.; Manita, S.; Horigane, S.-i.; Sakamoto, M.; Kawakami, R.; Yamaguchi, K.; Otomo, K.; Yokoyama, H.; Kim, R.; Yokoyama, T.; Takemoto-Kimura, S.; Abe, M.; Okamura, M.; Kondo, Y.; Quirin, S.; Ramakrishnan, C.; Imamura, T.; Sakimura, K.; Nemoto, T.; Kano, M.; Fujii, H.; Deisseroth, K.; Kitamura, K.; Bito, H., Rational Engineering of XCaMPs, a Multicolor GECI Suite for In Vivo Imaging of Complex Brain Circuit Dynamics. Cell **2019,** 177 (5), 1346-1360.e24.
97. Heim, N.; Griesbeck, O., Genetically Encoded Indicators of Cellular Calcium Dynamics Based on Troponin C and Green Fluorescent Protein. Journal of Biological Chemistry **2004,** 279 (14), 14280-14286.
98. Mank, M.; Reiff, D. F.; Heim, N.; Friedrich, M. W.; Borst, A.; Griesbeck, O., A FRET-Based Calcium Biosensor with Fast Signal Kinetics and High Fluorescence Change. Biophysical Journal **2006,** 90 (5), 1790-1796.
99. Shen, Y.; Dana, H.; Abdelfattah, A. S.; Patel, R.; Shea, J.; Molina, R. S.; Rawal, B.; Rancic, V.; Chang, Y.-F.; Wu, L.; Chen, Y.; Qian, Y.; Wiens, M. D.; Hambleton, N.; Ballanyi, K.; Hughes, T. E.; Drobizhev, M.; Kim, D. S.; Koyama, M.; Schreiter, E.

R.; Campbell, R. E., A genetically encoded Ca2+ indicator based on circularly permutated sea anemone red fluorescent protein eqFP578. BMC Biology **2018,** 16 (1), 9.
100. Qian, Y.; Piatkevich, K. D.; Mc Larney, B.; Abdelfattah, A. S.; Mehta, S.; Murdock, M. H.; Gottschalk, S.; Molina, R. S.; Zhang, W.; Chen, Y.; Wu, J.; Drobizhev, M.; Hughes, T. E.; Zhang, J.; Schreiter, E. R.; Shoham, S.; Razansky, D.; Boyden, E. S.; Campbell, R. E., A genetically encoded near-infrared fluorescent calcium ion indicator. Nature methods **2019,** 16 (2), 171-174.
101. Tang, S.; Wong, H.-C.; Wang, Z.-M.; Huang, Y.; Zou, J.; Zhuo, Y.; Pennati, A.; Gadda, G.; Delbono, O.; Yang, J. J., Design and application of a class of sensors to monitor Ca²⁺ dynamics in high Ca²⁺ concentration cellular compartments. Proceedings of the National Academy of Sciences **2011,** 108 (39), 16265.
102. Fosque, B. F.; Sun, Y.; Dana, H.; Yang, C.-T.; Ohyama, T.; Tadross, M. R.; Patel, R.; Zlatic, M.; Kim, D. S.; Ahrens, M. B.; Jayaraman, V.; Looger, L. L.; Schreiter, E. R., Labeling of active neural circuits in vivo with designed calcium integrators. Science **2015,** 347 (6223), 755.
103. Moeyaert, B.; Holt, G.; Madangopal, R.; Perez-Alvarez, A.; Fearey, B. C.; Trojanowski, N. F.; Ledderose, J.; Zolnik, T. A.; Das, A.; Patel, D.; Brown, T. A.; Sachdev, R. N. S.; Eickholt, B. J.; Larkum, M. E.; Turrigiano, G. G.; Dana, H.; Gee, C. E.; Oertner, T. G.; Hope, B. T.; Schreiter, E. R., Improved methods for marking active neuron populations. Nature communications **2018,** 9 (1), 4440.
104. Dittmer, P. J.; Miranda, J. G.; Gorski, J. A.; Palmer, A. E., Genetically encoded sensors to elucidate spatial distribution of cellular zinc. The Journal of biological chemistry **2009,** 284 (24), 16289-16297.
105. Qin, Y.; Dittmer, P. J.; Park, J. G.; Jansen, K. B.; Palmer, A. E., Measuring steady-state and dynamic endoplasmic reticulum and Golgi Zn²⁺ with genetically encoded sensors. Proceedings of the National Academy of Sciences **2011,** 108 (18), 7351.
106. Miranda, J. G.; Weaver, A. L.; Qin, Y.; Park, J. G.; Stoddard, C. I.; Lin, M. Z.; Palmer, A. E., New alternately colored FRET sensors for simultaneous monitoring of Zn^{2+} in multiple cellular locations. PloS one **2012,** 7 (11), e49371-e49371.
107. Lindenburg, L. H.; Hessels, A. M.; Ebberink, E. H. T. M.; Arts, R.; Merkx, M., Robust red FRET sensors using self-associating fluorescent domains. ACS chemical biology **2013,** 8 (10), 2133-2139.
108. Wegner, S. V.; Arslan, H.; Sunbul, M.; Yin, J.; He, C., Dynamic Copper(I) Imaging in Mammalian Cells with a Genetically Encoded Fluorescent Copper(I) Sensor. Journal of the American Chemical Society **2010,** 132 (8), 2567-2569.
109. Lindenburg, L. H.; Vinkenborg, J. L.; Oortwijn, J.; Aper, S. J. A.; Merkx, M., MagFRET: the first genetically encoded fluorescent Mg2+ sensor. PloS one **2013,** 8 (12), e82009-e82009.
110. Bischof, H.; Rehberg, M.; Stryeck, S.; Artinger, K.; Eroglu, E.; Waldeck-Weiermair, M.; Gottschalk, B.; Rost, R.; Deak, A. T.; Niedrist, T.; Vujic, N.; Lindermuth, H.; Prassl, R.; Pelzmann, B.; Groschner, K.; Kratky, D.; Eller, K.; Rosenkranz, A. R.; Madl, T.; Plesnila, N.; Graier, W. F.; Malli, R., Novel genetically

encoded fluorescent probes enable real-time detection of potassium in vitro and in vivo. Nature communications **2017,** 8 (1), 1422.
111. Shen, Y.; Wu, S.-Y.; Rancic, V.; Aggarwal, A.; Qian, Y.; Miyashita, S.-I.; Ballanyi, K.; Campbell, R. E.; Dong, M., Genetically encoded fluorescent indicators for imaging intracellular potassium ion concentration. Communications Biology **2019,** 2 (1), 18.
112. Chen, Z.; Ai, H. W., Single Fluorescent Protein-Based Indicators for Zinc Ion (Zn(2+)). Anal Chem **2016,** 88 (18), 9029-36.
113. Qin, Y.; Sammond, D. W.; Braselmann, E.; Carpenter, M. C.; Palmer, A. E., Development of an Optical Zn(2+) Probe Based on a Single Fluorescent Protein. ACS chemical biology **2016,** 11 (10), 2744-2751.
114. Fudge, D. H.; Black, R.; Son, L.; LeJeune, K.; Qin, Y., Optical Recording of Zn2+ Dynamics in the Mitochondrial Matrix and Intermembrane Space with the GZnP2 Sensor. ACS Chemical Biology **2018,** 13 (7), 1897-1905.
115. Chen, M.; Zhang, S.; Xing, Y.; Li, X.; He, Y.; Wang, Y.; Oberholzer, J.; Ai, H.-w., Genetically Encoded, Photostable Indicators to Image Dynamic Zn2+ Secretion of Pancreatic Islets. Analytical Chemistry **2019,** 91 (19), 12212-12219.
116. Minckley, T. F.; Zhang, C.; Fudge, D. H.; Dischler, A. M.; LeJeune, K. D.; Xu, H.; Qin, Y., Sub-nanomolar sensitive GZnP3 reveals TRPML1-mediated neuronal Zn2+ signals. Nature communications **2019,** 10 (1), 4806.
117. Liu, J.; Karpus, J.; Wegner, S. V.; Chen, P. R.; He, C., Genetically Encoded Copper(I) Reporters with Improved Response for Use in Imaging. Journal of the American Chemical Society **2013,** 135 (8), 3144-3149.
118. Grimley, J. S.; Li, L.; Wang, W.; Wen, L.; Beese, L. S.; Hellinga, H. W.; Augustine, G. J., Visualization of synaptic inhibition with an optogenetic sensor developed by cell-free protein engineering automation. The Journal of neuroscience : the official journal of the Society for Neuroscience **2013,** 33 (41), 16297-16309.
119. Zhong, S.; Navaratnam, D.; Santos-Sacchi, J., A genetically-encoded YFP sensor with enhanced chloride sensitivity, photostability and reduced ph interference demonstrates augmented transmembrane chloride movement by gerbil prestin (SLC26a5). PloS one **2014,** 9 (6), e99095-e99095.
120. Qian, Y.; Rancic, V.; Wu, J.; Ballanyi, K.; Campbell, R. E., A Bioluminescent Ca2+ Indicator Based on a Topological Variant of GCaMP6s. Chembiochem : a European journal of chemical biology **2019,** 20 (4), 516-520.
121. Aper, S. J. A.; Dierickx, P.; Merkx, M., Dual Readout BRET/FRET Sensors for Measuring Intracellular Zinc. ACS Chemical Biology **2016,** 11 (10), 2854-2864.
122. Oh, Y.; Park, Y.; Cho, J. H.; Wu, H.; Paulk, N. K.; Liu, L. X.; Kim, N.; Kay, M. A.; Wu, J. C.; Lin, M. Z., An orange calcium-modulated bioluminescent indicator for non-invasive activity imaging. Nature Chemical Biology **2019,** 15 (5), 433-436.
123. Llopis, J.; McCaffery, J. M.; Miyawaki, A.; Farquhar, M. G.; Tsien, R. Y., Measurement of cytosolic, mitochondrial, and Golgi pH in single living cells with green fluorescent proteins. Proceedings of the National Academy of Sciences of the United States of America **1998,** 95 (12), 6803-6808.

124. Griesbeck, O.; Baird, G. S.; Campbell, R. E.; Zacharias, D. A.; Tsien, R. Y., Reducing the Environmental Sensitivity of Yellow Fluorescent Protein: MECHANISM AND APPLICATIONS. Journal of Biological Chemistry **2001,** 276 (31), 29188-29194.
125. Shaner, N. C.; Lin, M. Z.; McKeown, M. R.; Steinbach, P. A.; Hazelwood, K. L.; Davidson, M. W.; Tsien, R. Y., Improving the photostability of bright monomeric orange and red fluorescent proteins. Nature methods **2008,** 5 (6), 545-551.
126. Shcherbo, D.; Murphy, C. S.; Ermakova, G. V.; Solovieva, E. A.; Chepurnykh, T. V.; Shcheglov, A. S.; Verkhusha, V. V.; Pletnev, V. Z.; Hazelwood, K. L.; Roche, P. M.; Lukyanov, S.; Zaraisky, A. G.; Davidson, M. W.; Chudakov, D. M., Far-red fluorescent tags for protein imaging in living tissues. Biochem J **2009,** 418 (3), 567-574.
127. Poëa-Guyon, S.; Ammar, M. R.; Erard, M.; Amar, M.; Moreau, A. W.; Fossier, P.; Gleize, V.; Vitale, N.; Morel, N., The V-ATPase membrane domain is a sensor of granular pH that controls the exocytotic machinery. J Cell Biol **2013,** 203 (2), 283-298.
128. Shen, Y.; Rosendale, M.; Campbell, R. E.; Perrais, D., pHuji, a pH-sensitive red fluorescent protein for imaging of exo- and endocytosis. J Cell Biol **2014,** 207 (3), 419-432.
129. Li, Y.; Tsien, R. W., pHTomato, a red, genetically encoded indicator that enables multiplex interrogation of synaptic activity. Nature neuroscience **2012,** 15 (7), 1047-1053.
130. DiPilato, L. M.; Cheng, X.; Zhang, J., Fluorescent indicators of cAMP and Epac activation reveal differential dynamics of cAMP signaling within discrete subcellular compartments. Proceedings of the National Academy of Sciences of the United States of America **2004,** 101 (47), 16513-16518.
131. Zhang, J.; Ma, Y.; Taylor, S. S.; Tsien, R. Y., Genetically encoded reporters of protein kinase A activity reveal impact of substrate tethering. Proceedings of the National Academy of Sciences **2001,** 98 (26), 14997.
132. Everett, K. L.; Cooper, D. M. F., An improved targeted cAMP sensor to study the regulation of adenylyl cyclase 8 by Ca2+ entry through voltage-gated channels. PloS one **2013,** 8 (9), e75942-e75942.
133. Honda, A.; Adams, S. R.; Sawyer, C. L.; Lev-Ram, V.; Tsien, R. Y.; Dostmann, W. R. G., Spatiotemporal dynamics of guanosine 3′,5′-cyclic monophosphate revealed by a genetically encoded, fluorescent indicator. Proceedings of the National Academy of Sciences **2001,** 98 (5), 2437.
134. Honda, A.; Sawyer, C. L.; Cawley, S. M.; Dostmann, W. R. G., Cygnets. In Phosphodiesterase Methods and Protocols, Lugnier, C., Ed. Humana Press: Totowa, NJ, 2005; pp 27-43.
135. Klarenbeek, J. B.; Goedhart, J.; Hink, M. A.; Gadella, T. W. J.; Jalink, K., A mTurquoise-based cAMP sensor for both FLIM and ratiometric read-out has improved dynamic range. PloS one **2011,** 6 (4), e19170-e19170.
136. Klarenbeek, J.; Goedhart, J.; van Batenburg, A.; Groenewald, D.; Jalink, K., Fourth-generation epac-based FRET sensors for cAMP feature exceptional brightness, photostability and dynamic range: characterization of dedicated sensors for FLIM, for ratiometry and with high affinity. PloS one **2015,** 10 (4), e0122513-e0122513.
137. Nikolaev, V. O.; Bünemann, M.; Hein, L.; Hannawacker, A.; Lohse, M. J., Novel Single Chain cAMP Sensors for Receptor-induced Signal Propagation. Journal of Biological Chemistry **2004,** 279 (36), 37215-37218.

138. Ponsioen, B.; Zhao, J.; Riedl, J.; Zwartkruis, F.; van der Krogt, G.; Zaccolo, M.; Moolenaar, W. H.; Bos, J. L.; Jalink, K., Detecting cAMP-induced Epac activation by fluorescence resonance energy transfer: Epac as a novel cAMP indicator. EMBO reports **2004,** 5 (12), 1176-1180.
139. van der Krogt, G. N. M.; Ogink, J.; Ponsioen, B.; Jalink, K., A comparison of donor-acceptor pairs for genetically encoded FRET sensors: application to the Epac cAMP sensor as an example. PloS one **2008,** 3 (4), e1916-e1916.
140. Thunemann, M.; Wen, L.; Hillenbrand, M.; Vachaviolos, A.; Feil, S.; Ott, T.; Han, X.; Fukumura, D.; Jain, R. K.; Russwurm, M.; de Wit, C.; Feil, R., Transgenic mice for cGMP imaging. Circ Res **2013,** 113 (4), 365-371.
141. Lager, I.; Looger, L. L.; Hilpert, M.; Lalonde, S.; Frommer, W. B., Conversion of a Putative Agrobacterium Sugar-binding Protein into a FRET Sensor with High Selectivity for Sucrose. Journal of Biological Chemistry **2006,** 281 (41), 30875-30883.
142. Takanaga, H.; Chaudhuri, B.; Frommer, W. B., GLUT1 and GLUT9 as major contributors to glucose influx in HepG2 cells identified by a high sensitivity intramolecular FRET glucose sensor. Biochim Biophys Acta **2008,** 1778 (4), 1091-1099.
143. San Martín, A.; Ceballo, S.; Baeza-Lehnert, F.; Lerchundi, R.; Valdebenito, R.; Contreras-Baeza, Y.; Alegría, K.; Barros, L. F., Imaging mitochondrial flux in single cells with a FRET sensor for pyruvate. PloS one **2014,** 9 (1), e85780-e85780.
144. Kikuta, S.; Hou, B.-H.; Sato, R.; Frommer, W. B.; Kikawada, T., FRET sensor-based quantification of intracellular trehalose in mammalian cells. Bioscience, Biotechnology, and Biochemistry **2016,** 80 (1), 162-165.
145. Okumoto, S.; Looger, L. L.; Micheva, K. D.; Reimer, R. J.; Smith, S. J.; Frommer, W. B., Detection of glutamate release from neurons by genetically encoded surface-displayed FRET nanosensors. Proceedings of the National Academy of Sciences of the United States of America **2005,** 102 (24), 8740-8745.
146. Hires, S. A.; Zhu, Y.; Tsien, R. Y., Optical measurement of synaptic glutamate spillover and reuptake by linker optimized glutamate-sensitive fluorescent reporters. Proceedings of the National Academy of Sciences of the United States of America **2008,** 105 (11), 4411-4416.
147. Mohsin, M.; Abdin, M. Z.; Nischal, L.; Kardam, H.; Ahmad, A., Genetically encoded FRET-based nanosensor for in vivo measurement of leucine. Biosensors and Bioelectronics **2013,** 50, 72-77.
148. Mohsin, M.; Ahmad, A., Genetically-encoded nanosensor for quantitative monitoring of methionine in bacterial and yeast cells. Biosensors and Bioelectronics **2014,** 59, 358-364.
149. Whitfield, J. H.; Zhang, W. H.; Herde, M. K.; Clifton, B. E.; Radziejewski, J.; Janovjak, H.; Henneberger, C.; Jackson, C. J., Construction of a robust and sensitive arginine biosensor through ancestral protein reconstruction. Protein Sci **2015,** 24 (9), 1412-1422.
150. Ameen, S.; Ahmad, M.; Mohsin, M.; Qureshi, M. I.; Ibrahim, M. M.; Abdin, M. Z.; Ahmad, A., Designing, construction and characterization of genetically encoded FRET-based nanosensor for real time monitoring of lysine flux in living cells. J Nanobiotechnology **2016,** 14 (1), 49-49.

151. Imamura, H.; Nhat, K. P. H.; Togawa, H.; Saito, K.; Iino, R.; Kato-Yamada, Y.; Nagai, T.; Noji, H., Visualization of ATP levels inside single living cells with fluorescence resonance energy transfer-based genetically encoded indicators. Proceedings of the National Academy of Sciences of the United States of America **2009,** 106 (37), 15651-15656.
152. Tsuyama, T.; Kishikawa, J.-i.; Han, Y.-W.; Harada, Y.; Tsubouchi, A.; Noji, H.; Kakizuka, A.; Yokoyama, K.; Uemura, T.; Imamura, H., In Vivo Fluorescent Adenosine 5′-Triphosphate (ATP) Imaging of Drosophila melanogaster and Caenorhabditis elegans by Using a Genetically Encoded Fluorescent ATP Biosensor Optimized for Low Temperatures. Analytical Chemistry **2013,** 85 (16), 7889-7896.
153. Zhao, F.-L.; Zhang, C.; Zhang, C.; Tang, Y.; Ye, B.-C., A genetically encoded biosensor for in vitro and in vivo detection of NADP+. Biosensors and Bioelectronics **2016,** 77, 901-906.
154. Mehta, S.; Zhang, Y.; Roth, R. H.; Zhang, J.-f.; Mo, A.; Tenner, B.; Huganir, R. L.; Zhang, J., Single-fluorophore biosensors for sensitive and multiplexed detection of signalling activities. Nature Cell Biology **2018,** 20 (10), 1215-1225.
155. Berg, J.; Hung, Y. P.; Yellen, G., A genetically encoded fluorescent reporter of ATP:ADP ratio. Nature methods **2009,** 6 (2), 161-166.
156. Tantama, M.; Martínez-François, J. R.; Mongeon, R.; Yellen, G., Imaging energy status in live cells with a fluorescent biosensor of the intracellular ATP-to-ADP ratio. Nature communications **2013,** 4, 2550-2550.
157. Zhao, Y.; Hu, Q.; Cheng, F.; Su, N.; Wang, A.; Zou, Y.; Hu, H.; Chen, X.; Zhou, H.-M.; Huang, X.; Yang, K.; Zhu, Q.; Wang, X.; Yi, J.; Zhu, L.; Qian, X.; Chen, L.; Tang, Y.; Loscalzo, J.; Yang, Y., SoNar, a Highly Responsive NAD+/NADH Sensor, Allows High-Throughput Metabolic Screening of Anti-tumor Agents. Cell metabolism **2015,** 21 (5), 777-789.
158. Tao, R.; Zhao, Y.; Chu, H.; Wang, A.; Zhu, J.; Chen, X.; Zou, Y.; Shi, M.; Liu, R.; Su, N.; Du, J.; Zhou, H.-M.; Zhu, L.; Qian, X.; Liu, H.; Loscalzo, J.; Yang, Y., Genetically encoded fluorescent sensors reveal dynamic regulation of NADPH metabolism. Nature methods **2017,** 14 (7), 720-728.
159. Bianchi-Smiraglia, A.; Rana, M. S.; Foley, C. E.; Paul, L. M.; Lipchick, B. C.; Moparthy, S.; Moparthy, K.; Fink, E. E.; Bagati, A.; Hurley, E.; Affronti, H. C.; Bakin, A. V.; Kandel, E. S.; Smiraglia, D. J.; Feltri, M. L.; Sousa, R.; Nikiforov, M. A., Internally ratiometric fluorescent sensors for evaluation of intracellular GTP levels and distribution. Nature methods **2017,** 14 (10), 1003-1009.
160. Lobas, M. A.; Tao, R.; Nagai, J.; Kronschläger, M. T.; Borden, P. M.; Marvin, J. S.; Looger, L. L.; Khakh, B. S., A genetically encoded single-wavelength sensor for imaging cytosolic and cell surface ATP. Nature communications **2019,** 10 (1), 711.
161. Marvin, J. S.; Borghuis, B. G.; Tian, L.; Cichon, J.; Harnett, M. T.; Akerboom, J.; Gordus, A.; Renninger, S. L.; Chen, T.-W.; Bargmann, C. I.; Orger, M. B.; Schreiter, E. R.; Demb, J. B.; Gan, W.-B.; Hires, S. A.; Looger, L. L., An optimized fluorescent probe for visualizing glutamate neurotransmission. Nature methods **2013,** 10 (2), 162-170.
162. Wang, Y.; Botvinick, E. L.; Zhao, Y.; Berns, M. W.; Usami, S.; Tsien, R. Y.; Chien, S., Visualizing the mechanical activation of Src. Nature **2005,** 434 (7036), 1040-1045.

163. Paster, W.; Paar, C.; Eckerstorfer, P.; Jakober, A.; Drbal, K.; Schütz, G. J.; Sonnleitner, A.; Stockinger, H., Genetically Encoded Förster Resonance Energy Transfer Sensors for the Conformation of the Src Family Kinase Lck. The Journal of Immunology **2009,** 182 (4), 2160.
164. Seong, J.; Lu, S.; Wang, Y., Live Cell Imaging of Src/FAK Signaling by FRET. Cell Mol Bioeng **2011,** 2 (4), 138-147.
165. Ouyang, M.; Sun, J.; Chien, S.; Wang, Y., Determination of hierarchical relationship of Src and Rac at subcellular locations with FRET biosensors. Proceedings of the National Academy of Sciences of the United States of America **2008,** 105 (38), 14353-14358.
166. Ting, A. Y.; Kain, K. H.; Klemke, R. L.; Tsien, R. Y., Genetically encoded fluorescent reporters of protein tyrosine kinase activities in living cells. Proceedings of the National Academy of Sciences of the United States of America **2001,** 98 (26), 15003-15008.
167. Ostergaard, H.; Henriksen, A.; Hansen, F. G.; Winther, J. R., Shedding light on disulfide bond formation: engineering a redox switch in green fluorescent protein. EMBO J **2001,** 20 (21), 5853-5862.
168. Hanson, G. T.; Aggeler, R.; Oglesbee, D.; Cannon, M.; Capaldi, R. A.; Tsien, R. Y.; Remington, S. J., Investigating Mitochondrial Redox Potential with Redox-sensitive Green Fluorescent Protein Indicators. Journal of Biological Chemistry **2004,** 279 (13), 13044-13053.
169. Fan, Y.; Chen, Z.; Ai, H.-w., Monitoring Redox Dynamics in Living Cells with a Redox-Sensitive Red Fluorescent Protein. Analytical Chemistry **2015,** 87 (5), 2802-2810.
170. Sugiura, K.; Nagai, T.; Nakano, M.; Ichinose, H.; Nakabayashi, T.; Ohta, N.; Hisabori, T., Redox sensor proteins for highly sensitive direct imaging of intracellular redox state. Biochemical and biophysical research communications **2015,** 457 (3), 242-248.
171. Abraham, B. G.; Santala, V.; Tkachenko, N. V.; Karp, M., Fluorescent protein-based FRET sensor for intracellular monitoring of redox status in bacteria at single cell level. Analytical and bioanalytical chemistry **2014,** 406 (28), 7195-7204.
172. Yano, T.; Oku, M.; Akeyama, N.; Itoyama, A.; Yurimoto, H.; Kuge, S.; Fujiki, Y.; Sakai, Y., A novel fluorescent sensor protein for visualization of redox states in the cytoplasm and in peroxisomes. Mol Cell Biol **2010,** 30 (15), 3758-3766.
173. Markvicheva, K. N.; Bilan, D. S.; Mishina, N. M.; Gorokhovatsky, A. Y.; Vinokurov, L. M.; Lukyanov, S.; Belousov, V. V., A genetically encoded sensor for H2O2 with expanded dynamic range. Bioorganic & medicinal chemistry **2011,** 19 (3), 1079-1084.
174. Kolossov, V. L.; Spring, B. Q.; Clegg, R. M.; Henry, J. J.; Sokolowski, A.; Kenis, P. J. A.; Gaskins, H. R., Development of a high-dynamic range, GFP-based FRET probe sensitive to oxidative microenvironments. Exp Biol Med (Maywood) **2011,** 236 (6), 681-691.
175. Ermakova, Y. G.; Bilan, D. S.; Matlashov, M. E.; Mishina, N. M.; Markvicheva, K. N.; Subach, O. M.; Subach, F. V.; Bogeski, I.; Hoth, M.; Enikolopov, G.; Belousov, V. V., Red fluorescent genetically encoded indicator for intracellular hydrogen peroxide. Nature communications **2014,** 5, 5222-5222.

176. Bilan, D. S.; Pase, L.; Joosen, L.; Gorokhovatsky, A. Y.; Ermakova, Y. G.; Gadella, T. W. J.; Grabher, C.; Schultz, C.; Lukyanov, S.; Belousov, V. V., HyPer-3: A Genetically Encoded H2O2 Probe with Improved Performance for Ratiometric and Fluorescence Lifetime Imaging. ACS Chemical Biology **2013,** 8 (3), 535-542.
177. Banach-Latapy, A.; He, T.; Dardalhon, M.; Vernis, L.; Chanet, R.; Huang, M.-E., Redox-sensitive YFP sensors for monitoring dynamic compartment-specific glutathione redox state. Free Radical Biology and Medicine **2013,** 65, 436-445.
178. Kolossov, V. L.; Leslie, M. T.; Chatterjee, A.; Sheehan, B. M.; Kenis, P. J. A.; Gaskins, H. R., Förster resonance energy transfer-based sensor targeting endoplasmic reticulum reveals highly oxidative environment. Exp Biol Med (Maywood) **2012,** 237 (6), 652-662.
179. Meyer, A. J.; Brach, T.; Marty, L.; Kreye, S.; Rouhier, N.; Jacquot, J.-P.; Hell, R., Redox-sensitive GFP in Arabidopsis thaliana is a quantitative biosensor for the redox potential of the cellular glutathione redox buffer. The Plant Journal **2007,** 52 (5), 973-986.
180. Shokhina, A. G.; Kostyuk, A. I.; Ermakova, Y. G.; Panova, A. S.; Staroverov, D. B.; Egorov, E. S.; Baranov, M. S.; van Belle, G. J.; Katschinski, D. M.; Belousov, V. V.; Bilan, D. S., Red fluorescent redox-sensitive biosensor Grx1-roCherry. Redox Biology **2019,** 21, 101071.
181. Fan, Y.; Makar, M.; Wang, M. X.; Ai, H.-w., Monitoring thioredoxin redox with a genetically encoded red fluorescent biosensor. Nature Chemical Biology **2017,** 13 (9), 1045-1052.
182. Eroglu, E.; Gottschalk, B.; Charoensin, S.; Blass, S.; Bischof, H.; Rost, R.; Madreiter-Sokolowski, C. T.; Pelzmann, B.; Bernhart, E.; Sattler, W.; Hallström, S.; Malinski, T.; Waldeck-Weiermair, M.; Graier, W. F.; Malli, R., Development of novel FP-based probes for live-cell imaging of nitric oxide dynamics. Nature communications **2016,** 7 (1), 10623.
183. Siegel, M. S.; Isacoff, E. Y., A Genetically Encoded Optical Probe of Membrane Voltage. Neuron **1997,** 19 (4), 735-741.
184. Ataka, K.; Pieribone, V. A., A genetically targetable fluorescent probe of channel gating with rapid kinetics. Biophysical journal **2002,** 82 (1 Pt 1), 509-516.
185. Storace, D. A.; Braubach, O. R.; Jin, L.; Cohen, L. B.; Sung, U., Monitoring Brain Activity with Protein Voltage and Calcium Sensors. Scientific Reports **2015,** 5 (1), 10212.
186. Murata, Y.; Iwasaki, H.; Sasaki, M.; Inaba, K.; Okamura, Y., Phosphoinositide phosphatase activity coupled to an intrinsic voltage sensor. Nature **2005,** 435 (7046), 1239-1243.
187. Jin, L.; Han, Z.; Platisa, J.; Wooltorton, J. R. A.; Cohen, L. B.; Pieribone, V. A., Single action potentials and subthreshold electrical events imaged in neurons with a fluorescent protein voltage probe. Neuron **2012,** 75 (5), 779-785.
188. Lee, S.; Geiller, T.; Jung, A.; Nakajima, R.; Song, Y.-K.; Baker, B. J., Improving a genetically encoded voltage indicator by modifying the cytoplasmic charge composition. Scientific Reports **2017,** 7 (1), 8286.
189. St-Pierre, F.; Marshall, J. D.; Yang, Y.; Gong, Y.; Schnitzer, M. J.; Lin, M. Z., High-fidelity optical reporting of neuronal electrical activity with an ultrafast fluorescent voltage sensor. Nature neuroscience **2014,** 17 (6), 884-889.

190. Yang, H. H.; St-Pierre, F.; Sun, X.; Ding, X.; Lin, M. Z.; Clandinin, T. R., Subcellular Imaging of Voltage and Calcium Signals Reveals Neural Processing In Vivo. Cell **2016,** 166 (1), 245-257.
191. Chavarha, M.; Villette, V.; Dimov, I. K.; Pradhan, L.; Evans, S. W.; Shi, D.; Yang, R.; Chamberland, S.; Bradley, J.; Mathieu, B.; St-Pierre, F.; Schnitzer, M. J.; Bi, G.; Toth, K.; Ding, J.; Dieudonné, S.; Lin, M. Z., Fast two-photon volumetric imaging of an improved voltage indicator reveals electrical activity in deeply located neurons in the awake brain. bioRxiv **2018**, 445064.
192. Abdelfattah, A. S.; Farhi, S. L.; Zhao, Y.; Brinks, D.; Zou, P.; Ruangkittisakul, A.; Platisa, J.; Pieribone, V. A.; Ballanyi, K.; Cohen, A. E.; Campbell, R. E., A Bright and Fast Red Fluorescent Protein Voltage Indicator That Reports Neuronal Activity in Organotypic Brain Slices. The Journal of Neuroscience **2016,** 36 (8), 2458.
193. Béjà, O.; Spudich, E. N.; Spudich, J. L.; Leclerc, M.; DeLong, E. F., Proteorhodopsin phototrophy in the ocean. Nature **2001,** 411 (6839), 786-789.
194. Kralj, J. M.; Hochbaum, D. R.; Douglass, A. D.; Cohen, A. E., Electrical Spiking in Escherichia coli Probed with a Fluorescent Voltage-Indicating Protein. Science **2011,** 333 (6040), 345.
195. Hochbaum, D. R.; Zhao, Y.; Farhi, S. L.; Klapoetke, N.; Werley, C. A.; Kapoor, V.; Zou, P.; Kralj, J. M.; Maclaurin, D.; Smedemark-Margulies, N.; Saulnier, J. L.; Boulting, G. L.; Straub, C.; Cho, Y. K.; Melkonian, M.; Wong, G. K.-S.; Harrison, D. J.; Murthy, V. N.; Sabatini, B. L.; Boyden, E. S.; Campbell, R. E.; Cohen, A. E., All-optical electrophysiology in mammalian neurons using engineered microbial rhodopsins. Nature methods **2014,** 11 (8), 825-833.
196. Piatkevich, K. D.; Jung, E. E.; Straub, C.; Linghu, C.; Park, D.; Suk, H.-J.; Hochbaum, D. R.; Goodwin, D.; Pnevmatikakis, E.; Pak, N.; Kawashima, T.; Yang, C.-T.; Rhoades, J. L.; Shemesh, O.; Asano, S.; Yoon, Y.-G.; Freifeld, L.; Saulnier, J. L.; Riegler, C.; Engert, F.; Hughes, T.; Drobizhev, M.; Szabo, B.; Ahrens, M. B.; Flavell, S. W.; Sabatini, B. L.; Boyden, E. S., A robotic multidimensional directed evolution approach applied to fluorescent voltage reporters. Nature chemical biology **2018,** 14 (4), 352-360.
197. Gong, Y.; Huang, C.; Li, J. Z.; Grewe, B. F.; Zhang, Y.; Eismann, S.; Schnitzer, M. J., High-speed recording of neural spikes in awake mice and flies with a fluorescent voltage sensor. Science (New York, N.Y.) **2015,** 350 (6266), 1361-1366.
198. Bando, Y.; Sakamoto, M.; Kim, S.; Ayzenshtat, I.; Yuste, R., Comparative Evaluation of Genetically Encoded Voltage Indicators. Cell Reports **2019,** 26 (3), 802-813.e4.
199. Abdelfattah, A. S.; Kawashima, T.; Singh, A.; Novak, O.; Liu, H.; Shuai, Y.; Huang, Y.-C.; Campagnola, L.; Seeman, S. C.; Yu, J.; Zheng, J.; Grimm, J. B.; Patel, R.; Friedrich, J.; Mensh, B. D.; Paninski, L.; Macklin, J. J.; Murphy, G. J.; Podgorski, K.; Lin, B.-J.; Chen, T.-W.; Turner, G. C.; Liu, Z.; Koyama, M.; Svoboda, K.; Ahrens, M. B.; Lavis, L. D.; Schreiter, E. R., Bright and photostable chemigenetic indicators for extended in vivo voltage imaging. Science **2019,** 365 (6454), 699.
200. Masharina, A.; Reymond, L.; Maurel, D.; Umezawa, K.; Johnsson, K., A Fluorescent Sensor for GABA and Synthetic GABAB Receptor Ligands. Journal of the American Chemical Society **2012,** 134 (46), 19026-19034.

201. Marvin, J. S.; Shimoda, Y.; Magloire, V.; Leite, M.; Kawashima, T.; Jensen, T. P.; Kolb, I.; Knott, E. L.; Novak, O.; Podgorski, K.; Leidenheimer, N. J.; Rusakov, D. A.; Ahrens, M. B.; Kullmann, D. M.; Looger, L. L., A genetically encoded fluorescent sensor for in vivo imaging of GABA. Nature methods **2019,** 16 (8), 763-770.
202. Kazemipour, A.; Novak, O.; Flickinger, D.; Marvin, J. S.; Abdelfattah, A. S.; King, J.; Borden, P. M.; Kim, J. J.; Al-Abdullatif, S. H.; Deal, P. E.; Miller, E. W.; Schreiter, E. R.; Druckmann, S.; Svoboda, K.; Looger, L. L.; Podgorski, K., Kilohertz frame-rate two-photon tomography. Nature methods **2019,** 16 (8), 778-786.
203. Shivange, A. V.; Borden, P. M.; Muthusamy, A. K.; Nichols, A. L.; Bera, K.; Bao, H.; Bishara, I.; Jeon, J.; Mulcahy, M. J.; Cohen, B.; Riordan, S. L.; Kim, C.; Dougherty, D. A.; Chapman, E. R.; Marvin, J. S.; Looger, L. L.; Lester, H. A., Determining the pharmacokinetics of nicotinic drugs in the endoplasmic reticulum using biosensors. The Journal of General Physiology **2019,** 151 (6), 738.
204. Venkatakrishnan, A. J.; Deupi, X.; Lebon, G.; Tate, C. G.; Schertler, G. F.; Babu, M. M., Molecular signatures of G-protein-coupled receptors. Nature **2013,** 494 (7436), 185-194.
205. Jing, M.; Zhang, P.; Wang, G.; Feng, J.; Mesik, L.; Zeng, J.; Jiang, H.; Wang, S.; Looby, J. C.; Guagliardo, N. A.; Langma, L. W.; Lu, J.; Zuo, Y.; Talmage, D. A.; Role, L. W.; Barrett, P. Q.; Zhang, L. I.; Luo, M.; Song, Y.; Zhu, J. J.; Li, Y., A genetically encoded fluorescent acetylcholine indicator for in vitro and in vivo studies. Nature Biotechnology **2018,** 36 (8), 726-737.
206. Feng, J.; Zhang, C.; Lischinsky, J. E.; Jing, M.; Zhou, J.; Wang, H.; Zhang, Y.; Dong, A.; Wu, Z.; Wu, H.; Chen, W.; Zhang, P.; Zou, J.; Hires, S. A.; Zhu, J. J.; Cui, G.; Lin, D.; Du, J.; Li, Y., A Genetically Encoded Fluorescent Sensor for Rapid and Specific In Vivo Detection of Norepinephrine. Neuron **2019,** 102 (4), 745-761.e8.
207. Greenwald, E. C.; Mehta, S.; Zhang, J., Genetically Encoded Fluorescent Biosensors Illuminate the Spatiotemporal Regulation of Signaling Networks. Chemical Reviews **2018,** 118 (24), 11707-11794.
208. Chen, T.-W.; Wardill, T. J.; Sun, Y.; Pulver, S. R.; Renninger, S. L.; Baohan, A.; Schreiter, E. R.; Kerr, R. A.; Orger, M. B.; Jayaraman, V.; Looger, L. L.; Svoboda, K.; Kim, D. S., Ultrasensitive fluorescent proteins for imaging neuronal activity. Nature **2013,** 499 (7458), 295-300.
209. Dana, H.; Sun, Y.; Mohar, B.; Hulse, B. K.; Kerlin, A. M.; Hasseman, J. P.; Tsegaye, G.; Tsang, A.; Wong, A.; Patel, R.; Macklin, J. J.; Chen, Y.; Konnerth, A.; Jayaraman, V.; Looger, L. L.; Schreiter, E. R.; Svoboda, K.; Kim, D. S., High-performance calcium sensors for imaging activity in neuronal populations and microcompartments. Nature methods **2019,** 16 (7), 649-657.

Chapter 2

Genetically Encoded, Photostable Indicators for Zn^{2+}

The results of this chapter have been partially published. A part of this chapter is thus converted from the paper (Anal. Chem. 2019, 91, 19, 12212-12219). Shen Zhang developed the biosensors, including library construction and screening, and *in vitro* characterization of ZIBG1, ZIBG2 and frGEZI0.2. Dr. Minghai Chen conducted experiments on culturing and imaging cells and islets. Dr. Yuan Xing, Dr. Xinyu Li, and Ms. Yi He isolated islets and assisted in the culturing and imaging of islets. Prof. Yong Wang and Prof. José Oberholzer supervised some parts of this project, such as experiments related to islet isolation and culture. Prof. Hui-wang Ai supervised and managed the overall project.

ABSTRACT

As an essential element for living organisms, zinc (Zn^{2+}) exerts its biological functions both intracellularly and extracellularly. Previous studies have reported a number of genetically encoded Zn^{2+} indicators (GEZIs), which have been widely used to monitor Zn^{2+} in the cytosol and intracellular organelles. However, it is challenging to localize existing GEZIs to the extracellular space to detect secreted Zn^{2+}. Herein, we report two photostable, green fluorescent protein (GFP) based indicators, ZIBG1 and ZIBG2, which respond to Zn^{2+} selectively and have affinities suited for detecting Zn^{2+} secretion from intracellular vesicles. In particular, ZIBG2 can be effectively targeted to the extracellular

side of the plasma membrane. We applied cell surface-localized ZIBG2 to monitor glucose-induced dynamic Zn^{2+} secretion from mouse insulinoma MIN6 cells and primary mouse and human pancreatic islets. Because Zn^{2+} is co-released with insulin from β-cells, the fluorescence of cell surface-localized ZIBG2 was shown to be a strong indicator of the functional potency of islets. Our work here has thus expanded the use of GEZIs to image dynamic Zn^{2+} secretion in live tissue. Because it is convenient to use genetically encoded indicators for expression over extended periods and for *in vivo* delivery, we envision future applications of ZIBG2 in the development of induced β-cells or islets to advance cell replacement therapies for diabetes and in direct imaging of Zn^{2+} secretion dynamics *in vivo*.

2.1. INTRODUCTION

Zinc (Zn^{2+}) is a ubiquitous element existing in all forms of life and the second most abundant transition metal in the human body.[1] Zn^{2+} deficiency and dysregulation can cause various diseases, including Alzheimer's disease (AD),[2] epilepsy,[3] cancer,[4] and cerebral ischemia.[5] Mammalian cells sequester high levels of Zn^{2+} from the extracellular space. Meanwhile, Zn^{2+} can be secreted to the extracellular space. In pancreatic β-cells, Zn^{2+} is required in the processes of insulin biosynthesis, maturation, storage, and secretion.[6] In insulin granules, two Zn^{2+} ions coordinate with six insulin monomers to form a hexametric-structure. Zn^{2+} is thus co-released with insulin during the fusion of intracellular vesicles with cytoplasm membrane.[6] Zn^{2+} is also essential for brain development and function.[7, 8] Existence of labile Zn^{2+} and Zn^{2+}-containing presynaptic vesicles has been known for decades.[9] A subset of glutamatergic neurons, which is mainly found in the cerebral cortex

or the limbic structures of the forebrain, can accumulate Zn^{2+} in vesicles by zinc transporters and release Zn^{2+} following electric stimulation.[10] Synaptically released Zn^{2+} can interact with a myriad of cell-surface channels, transporters, and receptors to modulate their activities, or enter postsynaptic neurons via cation-permeable channels to trigger intracellular signaling cascades.[11] Because Zn^{2+} plays essential biological roles intracellularly and extracellularly, it is highly desired to monitor Zn^{2+} both inside and outside cells.

Type 1 diabetes (T1D) is a devastating disease affecting 1.25 million Americans, including 200,000 youth.[12] It is expected to affect 5 million Americans (including 600,000 youth) by 2050. T1D costs the U.S. roughly $14.4 billion annually in medical expenses and lost incomes. Although it is still considered experimental by the U.S. Food and Drug Administration (FDA), allotransplant of islets from deceased donors to T1D patients is the only cell-based therapy able to achieve glycemic control without exogenous insulin.[13] It has been suggested that Zn^{2+} secretion from β-cells in islets could be an indicator for insulin secretion and the functional potency of islets.[14, 15] In this context, there is a strong interest in monitoring secreted Zn^{2+} in pancreatic islets.

Over the past several decades, a wide variety of Zn^{2+} indicators have been developed, including small molecule sensors,[16-19] genetically encoded sensors,[20-23] and hybrid sensors.[24, 25] In particular, genetically encoded indicators have attracted much attention, because of their high specificity and modulable affinity, convenience for precise subcellular localization, and genetic delivery capability to readily achieve transient or long-term expression in live cells and organisms. There are a large number of genetically encoded Zn^{2+} indicators (GEZIs) based on Förster resonance energy transfer (FRET) of

two fluorescent proteins (FPs).[26] These ratiometric GEZIs, such as eCALWY[27] and ZapCY[28] variants, are powerful tools for imaging Zn^{2+} in intracellular space and organelles. In addition, single FP-based, intensiometric GEZIs, which have narrower fluorescence excitation and emission profiles to facilitate multicolor or/and multiplexed imaging, have been recently reported.[20, 21] We previously developed green fluorescent, Zn^{2+}-turn-off indicators, ZnGreen1 and ZnGreen2, with 26.3-fold and 8.7-fold dynamic ranges (F_0/F_{min}), respectively, in addition to a red fluorescent sensor, ZnRed, showing a 3.8-fold (F_{max}/F_0) fluorescence turn-on by Zn^{2+}.[21] Meanwhile, Palmer and coworkers fused a circularly permuted green FP (cpGFP) with the zinc fingers of the transcription factor Zap1, resulting in a green fluorescent GZnP1 indicator showing 2.6-fold (F_{max}/F_0) fluorescence turn-on and 58 pM Zn^{2+} affinity.[20] Furthermore, a GZnP2 sensor with an improved dynamic range

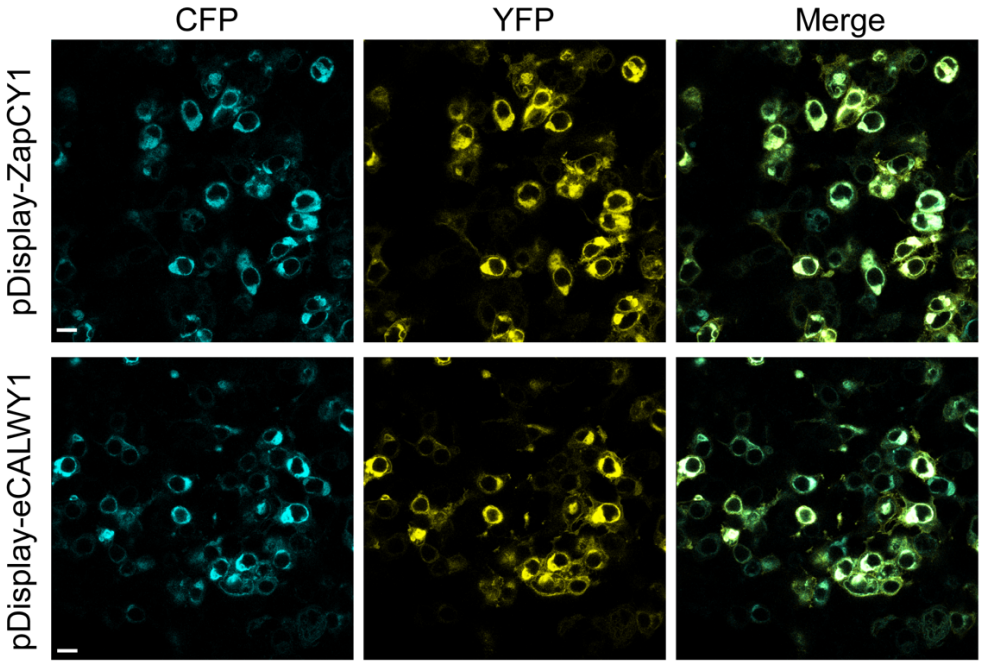

Figure 1. Representative images of pDisplay-ZapCY1 and pDisplay-eCALWY1 in HEK 293T cells (scale bars: 20 μm), showing insufficient cell surface localization. This experiment was repeated three times.

was recently developed.[29] Despite the progress, there is still a lack of GEZIs with properties well-suited for monitoring Zn^{2+} secretion from intracellular vesicles, because the Zn^{2+} affinities of most existing GEZIs, such as eCALWYs, ZapCYs, and GZnPs, are too high. Moreover, GEZIs based on Zn^{2+}-binding elements from Zap1 or ATOX1/WD4 cannot be effectively routed to the extracellular side of the plasma membrane by using the pDisplay vector (**Figure 1**). We previously utilized pDisplay-ZnGreen1 to detect glucose-stimulated Zn^{2+} secretion in insulin-secreting pancreatic β-cells, but a large portion of ZnGreen1 was intracellular.[21] Moreover, our previously reported ZnGreen1 and ZnGreen2 have nonoptimal photostability (**Figure 2**). It is thus challenging to interpret results because both

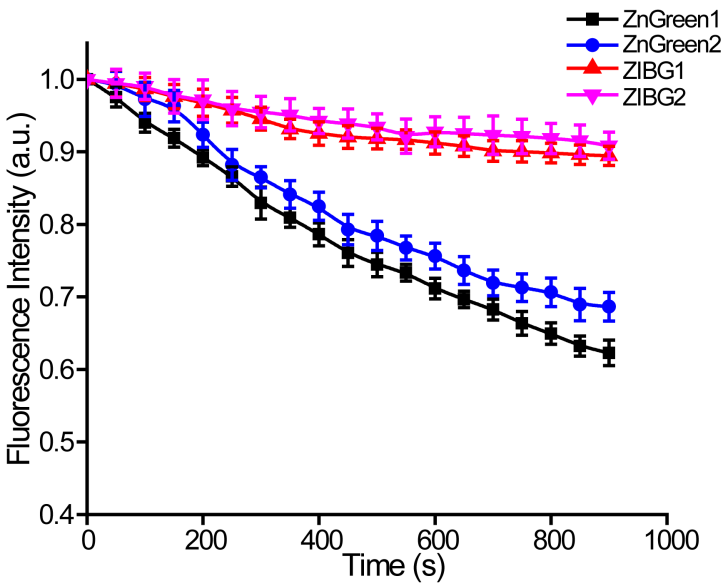

Figure 2. Photostability of ZIBG1 and ZIBG2 compared with our previously reported Zn^{2+} indicators, ZnGreen1 and ZnGreen2. HEK 293T cells expressing individual indicators were illuminated on a wide-field microscope equipped with a GFP filter cube and a Leica EL6000 mercury metal halide lamp (10% intensity). The exposure time was 100 ms and the acquisition interval was 5 s. The excitation shutter was closed between acquisitions. One image every 50 s was used to analyze fluorescence intensities, which were further normalized to values at t = 0 s. Data are presented as mean and s.d. of 10 cells from three independent replicates.

photobleaching and Zn^{2+} decrease the fluorescence of ZnGreen1 and ZnGreen2. There is still a remaining need for photostable, Zn^{2+}-turn-on GEZIs that can effectively traffic to the surface of mammalian cells and display moderate Zn^{2+} affinity for imaging of extracellular Zn^{2+} secreted from vesicles. Meanwhile, far-red fluorescent proteins have advantages in the development of genetically encoded sensors and labelling for bio-imaging *in vivo* since fluorescence in the long-wavelength region would have low photo-toxicity, better deep tissue penetration and minimal auto-fluorescence caused by bio-molecules. And thus, another aim was to develop a genetically encoded Zn^{2+} indicators that features far-red fluorescence (**Table 1**).

Table 1. Summary of single FP-based GEZIs.

sensor name	binding domain	FP	K_D	on/off	Dynamic range	reference
GZnP1	Zap1	cpGFP	58pM	on	2.6 fold	[20]
GZnP2	Zap1	cpGFP	352pM	on	6 fold	[30]
ZnGreen1	Zap1	mTFP1	633nM	off	26.3 fold	[21]
ZnGreen2	Zn hook	cpmTFP1	20μM	off	8.7 fold	[21]
ZnRed	Zap1	mApple	166nM/20μM	on	3.8 fold	[21]
ZIBG1	Zap1	GFP	2.81μM	on	2.5 fold	This work
ZIBG2	Zn hook	cpGFP	282nM	on	7 fold	This work
frGEZI0.2	Zn hook	cpmMaroon	10.6μM	on	2.5 fold	This work

In this chapter, we report two photostable Zn^{2+} indicators based on GFP, namely ZIBG1 and ZIBG2, with high nanomolar to low micromolar Zn^{2+} affinities. These two indicators are excitation-ratiometric but have an adequate dynamic range when their Zn^{2+}-turn-on fluorescence is intensiometrically monitored by using ~ 480 nm excitation. In particular, ZIBG2 can be effectively targeted to the extracellular side of the plasma membrane for monitoring glucose-induced dynamic Zn^{2+} secretion from mouse insulinoma

MIN6 cells, in addition to mouse and human pancreatic islets. These photostable GEZIs are expected to be valuable tools for understanding Zn^{2+} biology and may find translational applications in evaluation of donor islets for transplant, stem cell reprogramming and β-cell engineering, and high-throughput assays for chemicals or genetic elements to protect transplanted islets from hypoxia, immune rejection, or immunosuppressant-induced toxicity.[13, 31, 32] We also report one far-red genetically encoded Zn^{2+} indicator, namely frGEZI0.2, with low micromolar affinity and ~2.5-fold of dynamic range. It emits fluorescence in the far-red region and can be robustly expressed in the extracellular surface of mammalian cells.

2.2. EXPERIMENTAL SECTION

2.2.1. General Materials and Methods

All chemicals were purchased from Fisher Scientific or Sigma-Aldrich. Synthetic DNA oligos were purchased from Eurofins Genomics. Restriction endonucleases were purchased from New England Biolabs or Thermo Scientific. DNA sequences were analyzed by Eurofins Genomics. Absorbance and fluorescence spectroscopy data were collected by using a monochromator-based BioTek Synergy Mx Microplate Reader.

2.2.2 Library Construction

To develop ZIBG1, the cpGFP fragment from G-GECO1[33] was amplified and converted back to the wild-type FP topology. The two zinc fingers of Zap1 was then inserted to the site initially used for the circular permutation. The PCR product was cloned

into a pTorPE vector[33] by using restriction enzymes SalI and HindIII to obtain ZIBG0.1, which served as the template for further optimization. The two linkers between the Zap1 domain and GFP fragments were subjected to the randomization of length and composition (**Table 2**). To develop ZIBG2, a Rad50 zinc hook peptide (AKGKCPVCGAELTD) was fused to both of the N- and C-termini of cpGFP derived from G-GECO1. The resultant variant was also inserted into pTorPE and randomized for linker length and residue sequences (**Table 2**). To develop cpmMaroon1.1, the synthetic DNA oligonucleotides of wild type mMaroon1 was purchased from Integrated DNA Technologies (IDT). Circular mutated mMaroon1 was cloned through overlap PCR and several rounds of random mutagenesis through error-prone PCR. The same Rad50 zinc hook peptide (AKGKCPVCGAELTD) was fused to both of the N- and C-termini of cpmMaroon1.1. The library was cloned into pTorpe plasmid for the screening of linker lengths and composition.

Table 2. List of mutants and libraries made to derive the Zn^{2+} indicators with green fluorescence.

	Library	Identified mutant		Note
		1st linker sequence	2nd linker sequence	
Zap1 fusions	direct fuse	LEYNDLKC	NCQHVYIKAD	dim fluorescence; no fluorescence change
	N' 2NNK, C' 2NNK	LEYXXLKC	NCQXXYIKAD	no obvious change was observed; no mutant was sequenced
	1NNK inserted at N' and C'	LEYNGDLKC	NCQHAVYIKAD	30% fluorescence increase
	2NNK inserted at N' and C'	LEYNMVDLKC	NCQHSAVYIKAD	40% fluorescence increase
	2NNK at N', 1 NNK at C'	LEYNQSDLKC	NCQHSVYIKAD	150% fluorescence increase; dim fluorescence
	3NNK at N', 1 NNK at C'	LEYNMYGDLKC	NCQHSVYIKAD	ZlBG1
Zinc hook fusions	direct fuse	AELTDVYIKAD	LEYNAKGKC	dim fluorescence; 20% fluorescence increase
	1NNK inserted at N' and C'	AELTDCVYIKAD	LEYNAAKGKC	100% fluorescence increase
	2NNK at C'	AELTDCVYIKAD	LEYNPSAKGKC	ZlBG2

2.2.3. Library Screening and *In Vitro* Characterization

DH10B electrocompetent cells were transformed with the aforementioned gene libraries and plated on 2xYT agar plates supplemented with 100 μg/mL ampicillin and 0.002% (w/v) L-arabinose. The plates were incubated at 37 °C overnight and then at room temperature for an additional 24 hours before the fluorescence of individual colonies was examined. A digital fluorescence image of each plate was acquired before a 1 mM EDTA solution was sprayed by using a conventional fine mist sprayer. The EDTA solution was allowed to soak into the agar plate. This procedure of spraying and drying was repeated two additional times. A second digital fluorescence image was then acquired and the two

images were registered and processed for fluorescence intensity ratios using ImageJ by following a previously described method.[34] The fluorescence ratio for each colony was obtained and colonies with high ratios were further selected and cultured in 1 mL liquid 2xYT media supplemented with 100 μg/mL ampicillin and 0.002% (w/v) L-arabinose in 96-well deep-well bacterial culture plates. Plates were incubated at 37 °C, 250 rpm overnight and then at 25°C for an additional 24 hours. These 96-well culture plates were centrifuged at 4700 rpm for 10 minutes and pellets from each well were lysed with 300 μL of B-PER Bacterial Protein Extraction Reagents (Pierce). After centrifugation at 4700 rpm for 15 min, 100 μL of clear supernatant in each well was transferred into two identical 96-well fluorescence assay plates (50 μL each). 50 μL of Zn^{2+} buffer (50 mM Tris-HCl, 200 μM $ZnCl_2$, pH 7.4) or EDTA buffer (50 mM Tris-HCl, 200 μM EDTA, pH 7.4) were added to the two replicate 96-well plates to evaluate Zn^{2+} responsiveness of each mutant. Mutants showing large fluorescence changes between the Zn^{2+}-treated and EDTA-treated plates were chosen. Plasmids of these mutants were isolated from the remaining cell lysates and debris. Proteins of promising mutants were prepared and their Zn^{2+} responsiveness was further characterized by following a previously described procedure.[21] Zn^{2+} titration was performed with 0.2 μM sensor protein in a HEPES-based buffer (150 mM HEPES, 100 mM NaCl, 0.5 mM TCEP and 10% glycerol, pH 7.4). Solutions with free Zn^{2+} concentrations from nanomolar to micromolar were prepared by a "pH titration method",[35] which uses EDTA as the Zn^{2+} chelator and Mg^{2+}, Ca^{2+}, or Sr^{2+} as competing ions. Compositions of these solutions were exactly the same as reported by Palmer and coworkers.[28] An alkaline denaturation method[36] was used to determine the molar extinction

coefficients of the sensors. Quantum yields were determined by following a previously described procedure[20] and using fluorescein as the reference.[37, 38]

2.2.4. Culture and Plasmid Transfection of Cells and Islets

Human Embryonic Kidney (HEK) 293T cells were cultured in Dulbecco's Modified Eagle's Medium (DMEM) supplemented with 10% fetal bovine serum (FBS), 100 U/mL penicillin, and 100 μg/ mL streptomycin. MIN6 cells were cultured in DMEM supplemented with 10% FBS, 10 mM HEPES, 2 mM L-glutamine, 1 mM sodium pyruvate, and 0.05 mM 2-mercaptoethanol. All cells were incubated at 37°C with 5% CO_2 in a humidified incubator. At 70−80% confluence, cells were transfected with 2 μg of plasmid DNA and 10 μg of PEI (polyethylenimine, linear, 25 kDa). Transfected cells were then cultured in complete DMEM medium for another 24 h. Mouse pancreatic islets were isolated from the pancreata of 10-12 week-old C57/B6 mice (Jackson Laboratory, MA) and cultured as previously described.[39] In brief, the pancreata were injected with 0.375 mg/mL of Collagenase P (Roche Applied Science) and then digested at 37°C for 15 min. Islets were purified through a discontinuous Ficoll gradient (Mediatech) and then cultured in RPMI 1640 medium supplemented with 10% fetal bovine serum (Hyclone) and 1% penicillin/streptomycin (Mediatech) at 37°C with 5% CO_2. All procedures were approved by the Animal Care and Use Committee at the University of Virginia. Human islets were isolated and purified using the standard Edmonton protocol[40] at the University of Virginia after obtaining informed research consent. In each 35-mm culture dish, ~ 200 islets were transfected with 2 μg of plasmid DNA and 10 μg of PEI, and further cultured in complete RPMI 1640 media for 24 h before imaging analysis.

2.2.5. Fluorescence Imaging and Analysis

Images were acquired by using a 40× oil immersion objective lens on a Leica DMi8 microscope equipped with a Leica SPE-II spectral confocal module and a Photometrics Prime 95B Scientific CMOS camera. The confocal module was used to compare localization. In particular, a 488-nm laser was used for excitation of ZIBGs and the emission was collected at 500-560 nm; a 635-nm laser was used for excitation of a far-red FP mMaroon1 and the emission was collected at 655-800 nm. For time-lapse imaging, the wide-field Prime 95B camera and a GFP filter cube with a 470/40 nm bandpass excitation filter and a 525/50 nm bandpass emission filter were used to image ZIBGs; a Cy5 filter cube with a 628/40 nm bandpass excitation filter and a 692/40 nm bandpass emission filter was used to image mMaroon1. All images were processed by using the Leica LAS X software or ImageJ.

Transfected HEK 293T cells were washed three times with the Krebs Ringer Buffer (KRB; 135 mM NaCl, 5 mM KCl, 1 mM $MgSO_4$, 0.4 mM K_2HPO4, 1 mM $CaCl_2$, and 20 mM HEPES, pH 7.4) supplemented with 5 mM glucose before imaging. To test sensor responses to Zn^{2+}, time-lapse imaging was performed with an acquisition interval of 10 s and stimulating chemicals were added between acquisitions. The EDTA solution was freshly prepared and diluted with the KRB buffer to desired concentrations. $ZnCl_2$ was prepared as a stock solution in slightly acidic water and further diluted with the KRB buffer before use.

To image zinc release in MIN6 cells, transfected MIN6 cells expressing pDisplay-ZIBG1 or pDisplay-ZIBG2 were first incubated with the KRB buffer supplemented with 2.5 mM glucose and 10 μM EDTA for 1 h. After starvation and removing prebound Zn^{2+},

cells were washed three times with KRB containing 2.5 mM glucose and then retained in the buffer for imaging. Time-lapse images were acquired every 10 s. Following the initial ~2 min of image acquisition, MIN6 cells were stimulated with KRB containing 30 mM glucose[41, 42] and fluorescence imaging continued for another ~8 min. Samples were then rinsed with KRB containing 2 mM glucose injected through a syringe pump. Dual-color imaging of ZIBG2 and R-GECO1 in MIN6 cells were performed similarly. The localization of R-GECO1 was imaged with the confocal module. A 532 nm laser was used for excitation and the emission was collected from 550 nm to 700 nm. Time-lapse images for R-GECO1 were acquired by using a filter cube containing a 545/25 nm bandpass filter for excitation and a 605/70 nm bandpass filter for emission collection. Dual-color images in the two channels were acquired sequentially.

Dynamic stimulation of islets was achieved by exposing transfected islets to designated solutions within a microfluidic perfusion chamber and the stimulation process was carried out according to the previous protocol.[43, 44] In brief, the transfected islets were incubated in 2 mL KRB supplemented with 2.5 mM glucose for 30 minutes and then loaded into a temperature-equilibrated microfluidic device mounted on an inverted epifluorescence microscope. Solution exchange was achieved by using a syringe pump controlled with a computational program. Time-lapse imaging was sequentially performed between the two channels. The intervals between acquisitions were 2 s. Fluorescence signals were expressed as “change-in-percentage” after being normalized against basal intensity levels established before stimulation.

2.3. RESULTS AND DISCUSSION

2.3.1. Development of green fluorescent Zn^{2+}-turn-on indicators

Our previously reported Zn^{2+}-turn-off indicators, ZnGreen1 and ZnGreen2, have relatively poor photostability (**Figure 2**). This issue may be caused by the circularly permuted mTFP1 scaffold used in both ZnGreen1 and ZnGreen2.[21, 45] To address this shortcoming, we decided to examine a different FP scaffold.[33] We amplified a cpGFP fragment from G-GECO1[33] and converted it back to the wild-type FP topology. We inserted the two zinc fingers of Zap1 to the site initially used for circular permutation (**Figure 3a**). The Zn^{2+}-binding domain from Zap1 was selected because it performed well in previously developed Zn^{2+} indicators.[20, 21] We randomized the two linkers at both ends of the Zn^{2+}-binding domain. After library screening, we derived ZIBG1, a variant showing a 2.5-fold excitation-ratiometric fluorescence response to Zn^{2+} (**Figure 3b**). Meanwhile, we explored another strategy to construct Zn^{2+} sensors. We chose a minimal zinc hook peptide from Pyrococcus furiosus Rad 50, which can form homodimer in response to Zn^{2+} binding,[46] and fused the zinc hook peptide to each of the N- and C-termini of cpGFP derived from G-GECO1 (**Figure 3a**) .[33] We performed optimization on both linkers based on Zn^{2+}-induced responses and derived ZIBG2, which has a 7-fold excitation-ratiometric fluorescence response to Zn^{2+} (**Figure 3c**). When illuminated near their major absorbance peak at ~ 480 nm, both ZIBG1 and ZIBG2 displayed fluorescence turn-on response to Zn^{2+}, and ZIBG2 outperformed ZIBG1 in terms of the dynamic range.

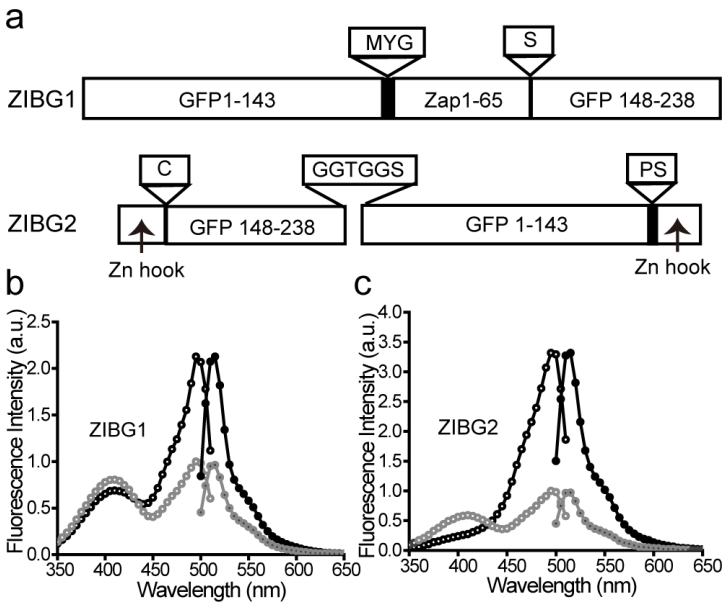

Figure 3. Engineering of GFP-based GEZIs, ZIBG1 and ZIBG2. (a) Domain arrangements of ZIBG1 and ZIBG2. Important linker sequences are shown in individual boxes. (b) Fluorescence excitation (open circle) and emission (filled circle) spectra of ZIBG1 and ZIBG2, in the presence (blank lines, treated with 100 μM $ZnCl_2$) and absence (gray lines, treated with 100 μM EDTA) of Zn^{2+}.

2.3.2. Development of far-red fluorescent Zn^{2+} indicators

As mentioned in Chapter 1, a large number of fluorescent proteins that emit in the far-red or near-infrared region have blossomed recently. Among them, we determined mMaroon1 as a potential template for engineering far-red fluorescent Zn^{2+} indicators because of its high maturation efficiency, brightness, and identity between mMarron1 and GFP. Residue 148, which is the traditional site to introduce circular permutation, was selected at initial attempts. Unfortunately, no colony showing bright far-red fluorescence was obtained after several rounds of screening. Then we turned our eyes to other loops located in the β-barrel of mMaroon1. In 2009, Sunita et al. identified residue 180 as the

most promising site for circular permutation of mKate.[47] Through sequence alignment of mKate and mMaroon1, we were able to determine the residue of mMaroon1 for circular permutation. After obtaining the circularly permuted mMaroon1 (cpmMaroon1), the optimization in brightness and maturation was conducted. Through one round of random mutagenesis, cpmMaroon1.1 was identified. It shows a significant improvement in photo properties, compared to the wild type mMaroon1 (**Figure 4**).

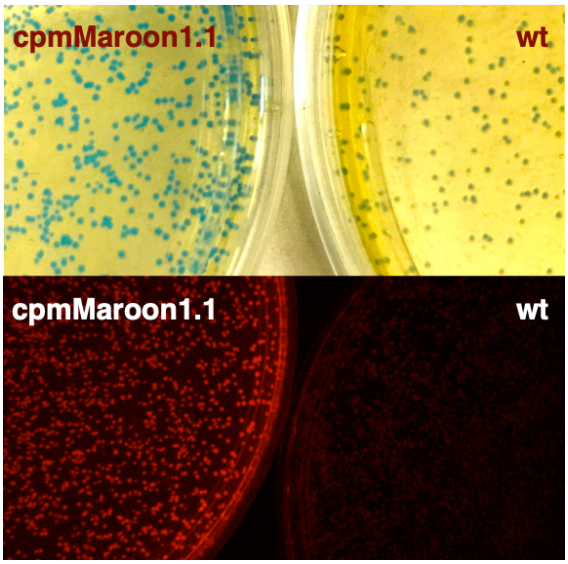

Figure 4. Comparison of cpmMaroon1.1 and wild type (wt) mMaroon1 on colonies. Images were taken either under bright field or far-red fluorescence. cpmMaroon1.1 exhibits large improvement in terms of extinction coefficient and brightness.

Sequence alignment between wild type mMaroon1 and cpmMaroon1.1 revealed one crucial mutation D163Y. This mutation is believed to contribute to the hydrogen-bond interaction between the chromophore and the β-barrel. (**Figure 5**)

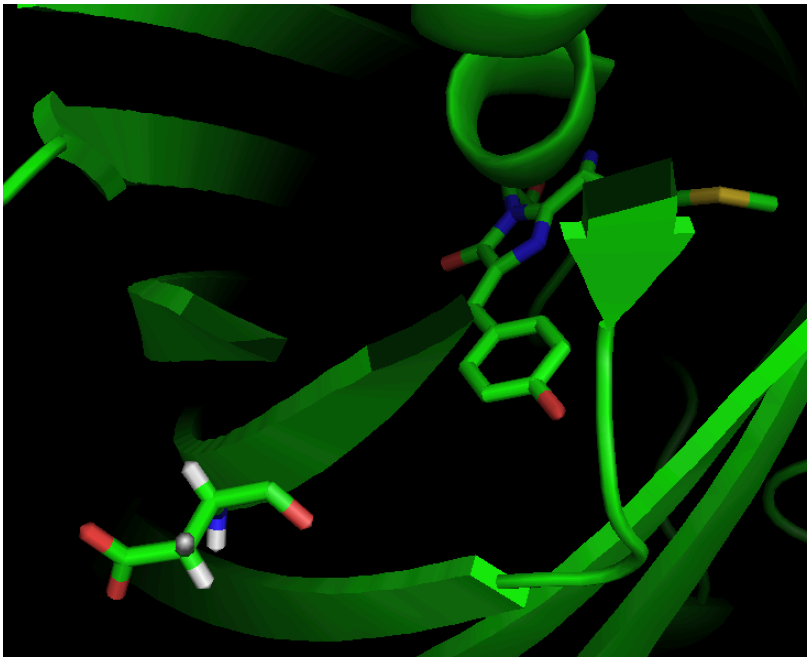

Figure 5. Structure of mCardinal. D163 and the chromophore are shown in sticks. Because of the proximity between D163 and the chromophore, mutation of D163Y might form polar interactions between the β-barrel and the chromophore.

Once the cpmMaroon1.1 featuring high brightness and fast maturation was obtained, we used it as the template in engineering far-red fluorescent genetically encoded Zn^{2+} indicators (frGEZI). The same Rad50 zinc hook peptide used in the development of ZIBG2 was fused to both of the N- and C-termini of cpmMaroon1.1 to develop frGEZI. The resultant variant was inserted into pTorPE and randomized for linker length and residue sequences. Two rounds of random mutagenesis of both N- and C- terminus of linkers yielded frGEZI0.2 that appeared to be bright and showed ~2.5-fold dynamic ranges (F/F_0). (**Figure 6a**)

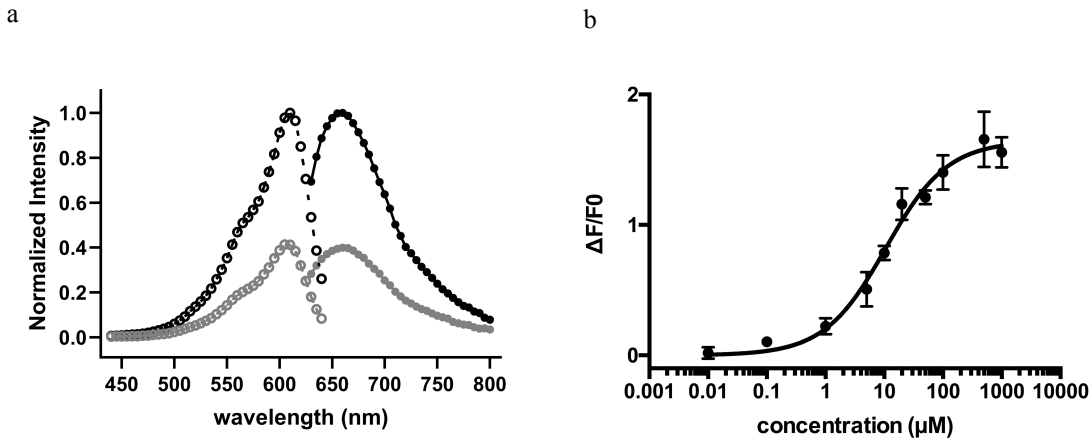

Figure 6. *In vitro* characterization of frGEZI0.2. (a) Fluorescence excitation (open circle) and emission (filled circle) spectra of frGEZI0.2, in the presence (black lines, treated with 100 μM $ZnCl_2$) and absence (gray lines, treated with 100 μM EDTA) of Zn^{2+}. (b) Zn^{2+} titration curves for frGEZI0.2 (black circle).

2.3.3. Characterization and Validation of Zn^{2+} Indicators

We next characterized ZIBG1, ZIBG2, and frGEZI0.2 *in vitro* and further validated their use in living mammalian cells. Key photophysical properties (i.e., molar extinction coefficient, quantum yield, and intrinsic brightness) of these newly developed ZIBGs were determined in the presence and absence of Zn^{2+} (**Table 3**), further confirming the high brightness and excellent dynamic range of ZIBG1 and ZIBG2. Titrating ZIBG1, ZIBG2 and frGEZI0.2 with buffered Zn^{2+} solutions revealed apparent binding affinities (K_d's) of 2.81 ± 1.3 μM and 282.4 ± 32 nM, 10.6 ± 3.1μM respectively (**Figure 7a and Figure 6b**). We also tested the responses to other highly abundant cellular metals for ZIBG1 and ZIBG2, including Mg^{2+}, Mn^{2+}, Ca^{2+}, K^+, and Na^+. These additional metals triggered little to no fluorescence response (**Figure 7b**), confirming the specificity of our newly engineered GEZIs. Moreover, the addition of the Zn^{2+} chelator EDTA to Zn^{2+}-treated

proteins brought their fluorescence back to the original levels, supporting the reversibility of ZIBG1 and ZIBG2 (**Figure 7b**).

Table 3. Summary of Biophysical Characteristics of ZIBG1 and ZIBG2.

	quantum yield (QY)		extinction coefficient (ε) at 495 nm [a]		brightness [b]	
	+ EDTA	+ Zn^{2+}	+ EDTA	+ Zn^{2+}	+ EDTA	+ Zn^{2+}
ZIBG1	0.22±0.04	0.29±0.02	17.1±0.6	29.1±0.5	3.8	8.4
ZIBG2	0.31±0.01	0.41±0.01	10.4±0.6	39.1±1.0	3.2	16.0

[a] Expressed in the units of mM^{-1} cm^{-1}.

[b] Defined as the product of ε and QY.

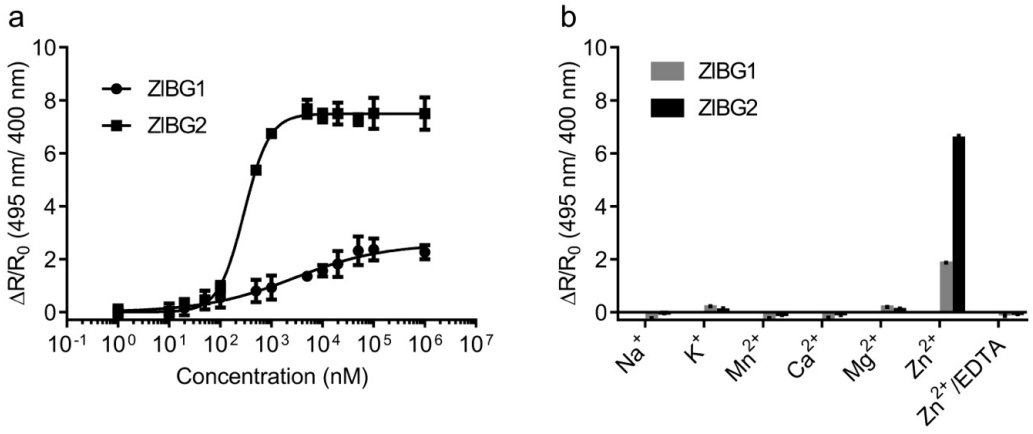

Figure 7. *In vitro* characterizations of engineered Zn^{2+} indicators. (a) Zn^{2+} titration curves for ZIBG1 (black circle) and ZIBG2 (black square). (b) Fluorescence responses of ZIBG1 and ZIBG2 to various metal ions, supporting the excellent specificity of ZIBG1 and ZIBG2 toward Zn^{2+}. Final concentrations were 20 μM for Zn^{2+} and 100 μM for all other metals. Fluorescence intensities were normalized to blank (no metal ion added). Data are presented as mean and s.d. of three independent replicates.

Next, we used a pDisplay vector to localize ZIBG1, ZIBG2, and frGEZI0.2 to the extracellular side of living HEK 293T cells. To simplify experimental procedures, we

imaged ZIBG1 and ZIBG2 by operating them as fluorescence turn-on sensors with excitation at ~ 480 nm. Under similar microscopic illumination conditions, the fluorescence of ZIBG1 and ZIBG2 was largely retained while the fluorescence of ZnGreen1 and ZnGreen2 dropped by ~ 30% in 800 s. The data suggest that the photostability of ZIBG1 and ZIBG2 was significantly improved from that of ZnGreen1 and ZnGreen2. Moreover, in comparison to ZIBG1 and other tested GEZIs, ZIBG2 could be well localized to the cell surface (**Figure 1, Figure 8a**, **and Figure 9**). Extracellular addition of Zn^{2+} triggered the fluorescence increase of both ZIBG1 and ZIBG2, while a subsequent addition of EDTA quickly reverted the fluorescence changes (**Figure 8 and Figure 9a**). We co-transfected cells with ZIBG2 and a far-red FP mMaroon1,[48] and no

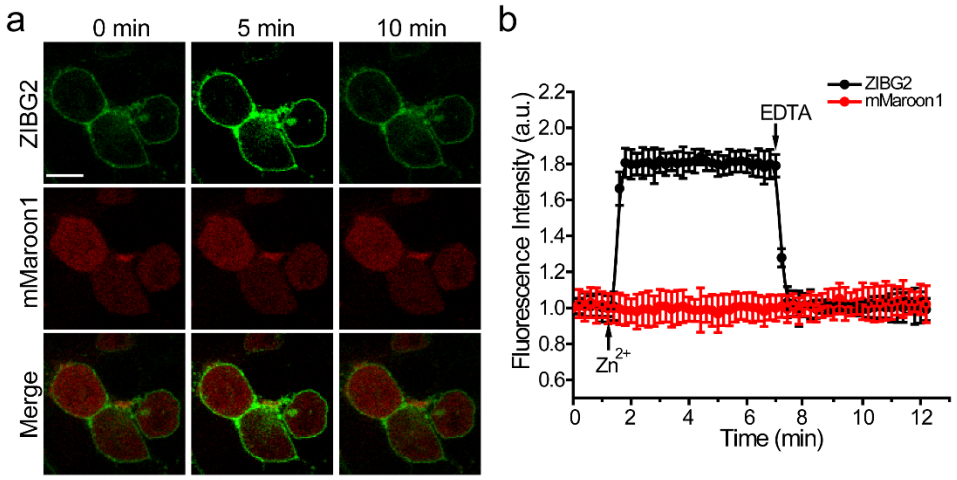

Figure 8. Fluorescence imaging of pDisplay-ZIBG2 in HEK 293T cells. (a) Fluorescence images of HEK 293T cells expressing pDisplay-ZIBG2 before and after sequential addition of $ZnCl_2$ (100 μM) and EDTA (100 μM). Cells were co-transfected with a far-red FP, mMaroon1, which serves as an internal control. Scale bar: 20 μm. (b) Quantitative results presented as mean and s.d. of 20 cells from three independent replicates. The arrows show the time points for addition of $ZnCl_2$ and EDTA.

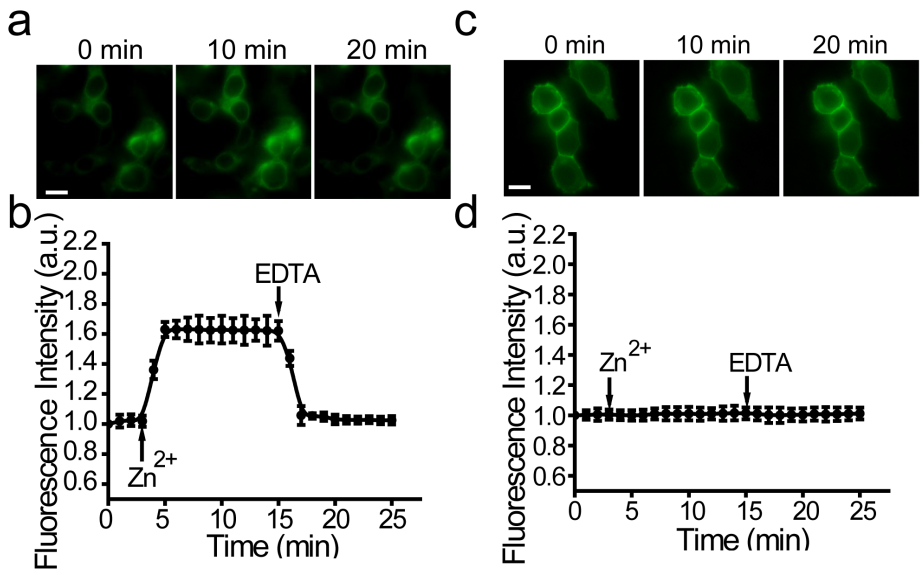

Figure 9. Fluorescence imaging and representative quantification traces of pDisplay-ZIBG1 (ab) and pDisplay-cpGFP (cd) in HEK 293T cells in response to Zn^{2+} and EDTA (scale bars: 20 μm). The arrows indicate time points for addition of Zn^{2+} or EDTA. Data are presented as mean and s.d. of 15 cells from three independent replicates.

noticeable fluorescence change of mMaroon1 was observed upon the stimulations (**Figure 8**). To further confirm that the Zn^{2+}-induced fluorescence increase was not caused by pH fluctuations, we treated HEK 293T cells expressing pDisplay-cpGFP, a Zn^{2+}-irresponsive control indicator, with $ZnCl_2$ and EDTA, and there was no obvious fluorescence response (**Figure 9b**).

Next, we imaged frGEZI0.2 by operating it as fluorescence turn-on sensors with excitation at ~600 nm. Similar to the result of ZIBG2, frGEZI0.2 could be well localized to the cell surface. The extracellular addition of Zn^{2+} could trigger the fluorescence increase of frGEZI0.2 (**Figure 10**).

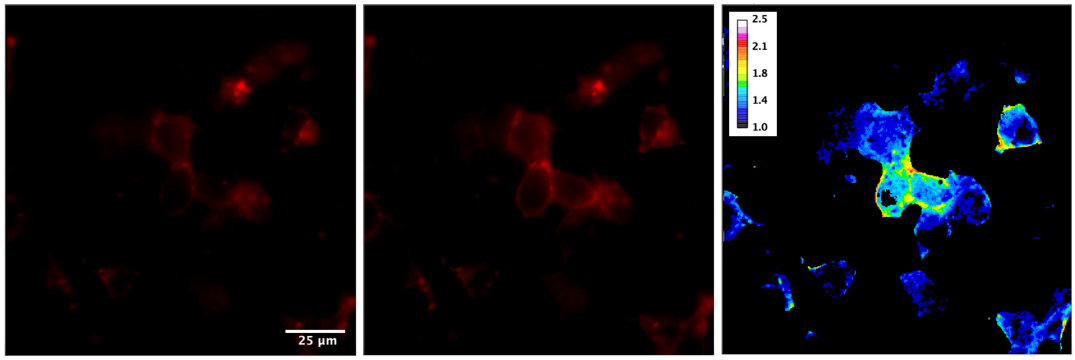

Figure 10. Fluorescence imaging of pDisplay-frGEZI0.2 in HEK 293T cells before (a) and after (b) addition of $ZnCl_2$ (100 µM). (c) Puesdo-colored image of ratio between (a) and (b). Scale bar: 25 µm.

We further explored the Zn^{2+} association and dissociation kinetics of ZIBG2. We placed ZIBG2-expressing HEK 293T cells on an upright microscope and positioned a glass micro pipet close to individual cells. We applied a brief 100-ms puff to spray a small volume of buffered $ZnCl_2$ solution to the cell and monitored the fluorescence of ZIBG2. By averaging several trials, the half-life ($t_{1/2}$) for the fluorescence rise (Zn^{2+} association) was determined to be ~ 45 ms, while the half-life ($t_{1/2}$) for the fluorescence decrease (Zn^{2+} dissociation) was ~ 1.6 s (**Figure 11**). We want to note that these half-lives were likely overestimated due to our hardware limitations, including slow compound application (~ 100 ms) and camera acquisition intervals (~ 150 ms). The rapid response, excellent photostability, and sufficient surface localization of pDisplay- ZIBG2 suggest that it may be an excellent indicator for time-lapse imaging of extracellular Zn^{2+} dynamics.

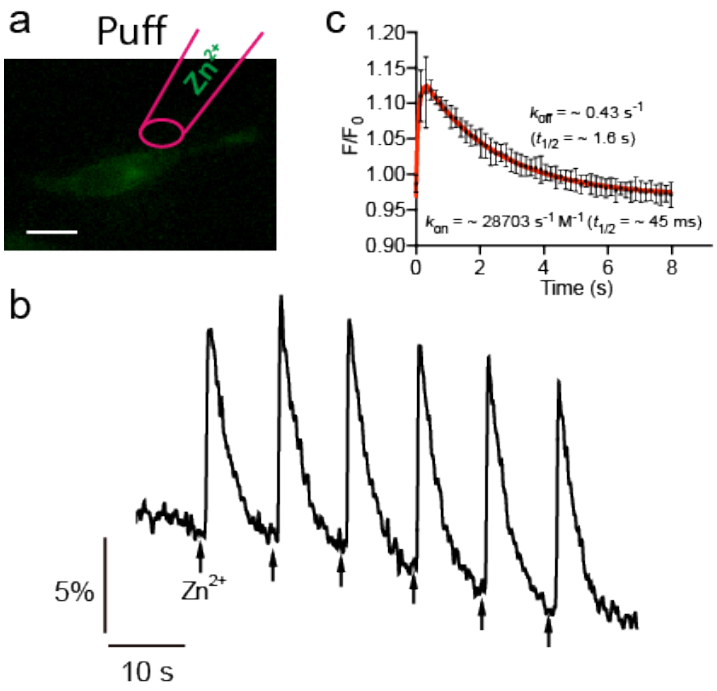

Figure 11. pDisplay-ZIBG2 in the HEK 293T cells in response to a brief 100-ms puff application of Zn^{2+}. (a) Illustration of the experiment. On an upright microscope, a glass micro pipet on a micromanipulator was positioned in proximity to a cell. Pressure is applied with Picospritzer II to spray a buffered 1 mM $ZnCl_2$ to the cell. Fluorescence was acquired simultaneously (scale bar: 20 μm). (b) Representative fluorescence traces. The arrows indicate time points for 100-ms puffs of Zn^{2+}. The experiment was repeated on three different cells (each 6 puffs). (c) Fitting of the averaged data for k_{on} and k_{off} with the "association and then dissociation" model using GraphPad Prism 8. The values are rough estimations and should be treated with cautions due to our hardware limitations including slow compound application (~ 100 ms) and camera acquisition intervals (~ 150 ms).

2.3.4. Live-Cell Imaging of Glucose-Stimulated Zn^{2+} Secretion in MIN6 Cells

To further validate our newly developed Zn^{2+} indicators for monitoring physiologically relevant Zn^{2+} dynamics, we transiently expressed pDisplay-ZIBG1 and pDisplay-ZIBG2 in MIN6 cells, a mouse insulinoma cell line.[49] In pancreatic β-cells, Zn^{2+} is an essential element for the biosynthesis and secretion of insulin and it can form co-crystals with insulin in the vesicular granules to aid the storage of insulin. Following glucose stimulation, Zn^{2+} and insulin are expected to co-release from pancreatic β-cells to the extracellular space. MIN6 cells co-transfected with pDisplay-ZIBG2 and mMaroon1 were first stimulated with high concentrations of extracellular glucose (30 mM) and then washed to reduce glucose to the basal level (2 mM). As expected, we observed a drastic fluorescence increase and then decrease from ZIBG2 (**Figure 12**), further supporting the reversibility of ZIBG2. In particular, ZIBG2 was well localized to the cell surface and its

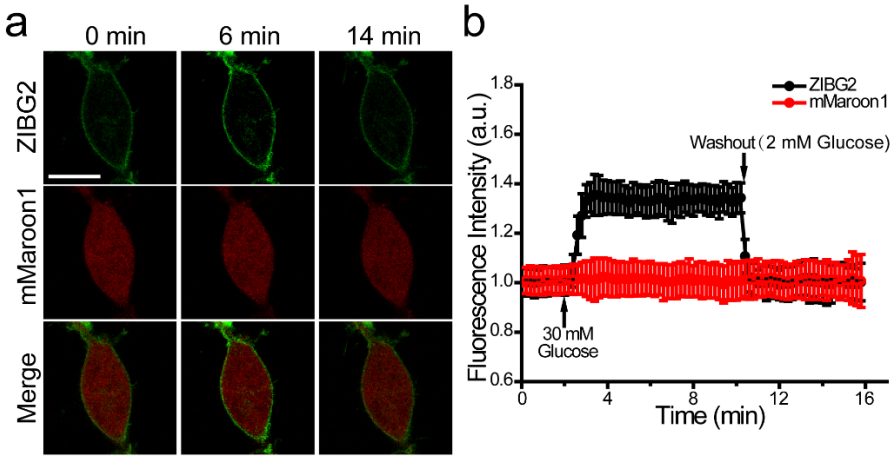

Figure 12. Fluorescence monitoring of glucose-induced Zn^{2+} release in MIN6 cells with pDisplay-ZIBG2. (a) Fluorescence images of cells expressing ZIBG2 in response to high glucose (30 mM) and subsequent washout with low glucose (2 mM). Cells were co-transfected with a far-red FP, mMaroon1, which serves as an internal control. Scale bar: 20 μm. (b) Quantitative results presented as mean and s.d. of 8 cells from three independent replicates. The arrow indicates the time point for addition of glucose.

high fluorescence indicates the active Zn^{2+} release to the extracellular space. No obvious fluorescence change was observed for mMaroon1 (**Figure 12**). In addition, we treated MIN6 cells with high concentrations of sucrose (30 mM) and no noticeable fluorescence change was detected (**Figure 13**). We also detected fluorescence increase and even

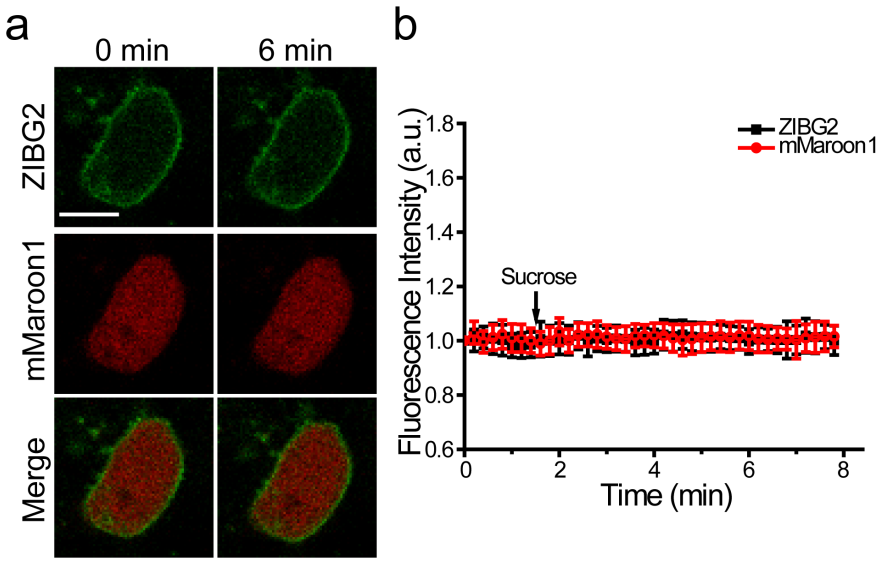

Figure 13. Fluorescence imaging of pDisplay-ZIBG2 in MIN6 cells in response to sucrose. (a) Fluorescence images of cells expressing ZIBG2 before and after addition of 30 mM sucrose. A far-red fluorescent protein mMaroon1 was used to co-transfect cells (scale bar: 20 μm). (b) Quantitative results presented as mean and s.d. of 10 cells from three independent replicates. The arrow indicates the time point for addition of sucrose.

oscillations from pDisplay-ZIBG1-transfected MIN6 cells upon glucose stimulation (**Figure 14**). The observation of oscillations may own to the lower binding affinities of ZIBG1 to Zn^{2+}. It is also possible that the oscillations are intracellular since the majority of ZIBG1 could not traffic to the cell membrane. We further treated HEK 293T cells transfected with pDisplay-ZIBG2 or pDisplay-ZIBG1 and observed no fluorescence

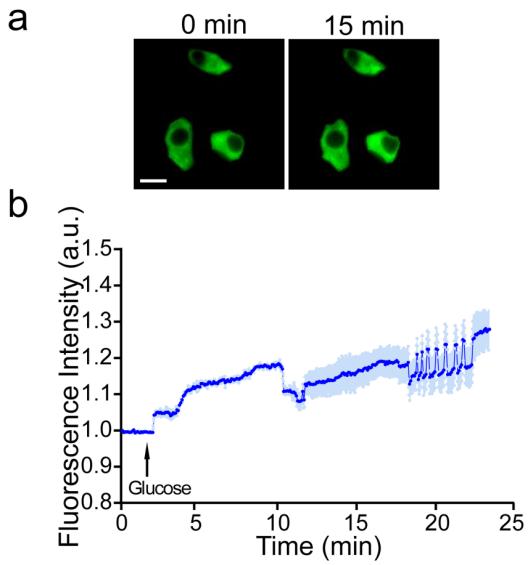

Figure 14. Monitoring of glucose-induced Zn^{2+} dynamics in MIN6 cells with pDisplay-ZIBG1. (a) Fluorescence images of cells expressing ZIBG1 before and after addition of 30 mM glucose, showing insufficient cell surface localization of ZIBG1 in MIN6 cells (scale bar: 20 μm). (b) Quantitative results presented as mean and s.d. of 8 cells from two independent replicates. The arrow indicates the time point for addition of glucose.

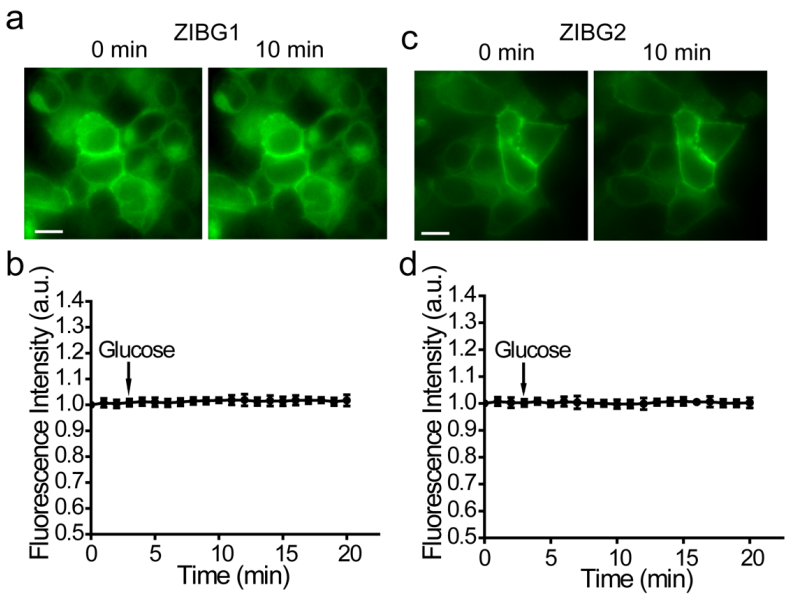

Figure 15. Fluorescence imaging and quantification traces of pDisplay-ZIBG1 (ab) and pDisplay-ZIBG2 (cd) in HEK 293T cells in response to 30 mM glucose (scale bars: 20 μm), showing that glucose does not directly impact the fluorescence of ZIBG1 and ZIBG2. The arrows indicate time points for addition of glucose. Data are presented as mean and s.d. of 15 cells from three independent replicates.

change upon high glucose stimulation (**Figure 15**), suggesting that the fluorescence changes in MIN6 cells were indeed caused by glucose-induced Zn^{2+} dynamics in pancreatic β-cells.

2.3.5. Dual-Color Imaging of Zn^{2+} and Ca^{2+} Dynamics in Live MIN6 Cells

Intracellular Ca^{2+} is an important coupling factor and regulator of insulin release. Briefly, glucose enters β-cells via glucose transporter 2 (GLUT2), and glycolysis leads to the generation of pyruvate, which enters the tricarboxylic acid (TCA) cycle. Newly produced NADH then enters the electron transport chain and generates an electric potential gradient across the mitochondrial membrane, leading to ATP generation. ATP closes ATP-sensitive K^+ (K_{ATP}) channels, initiating plasma membrane depolarization and increasing intracellular Ca^{2+} via voltage-dependent calcium channels (VDCCs). This glucose-induced Ca^{2+} dynamics triggers the fusion of insulin granules with cell membrane and the exocytosis of insulin, C-peptide, proinsulin, and Zn^{2+}. In this context, concurrent imaging of intracellular Ca^{2+} and extracellular Zn^{2+} can provide key information on β-cell function.

We transfected MIN6 cells with pDisplay-ZIBG2 along with a red fluorescent Ca^{2+} sensor, R-GECO1.[33] Under this condition, R-GECO1 was localized to the intracellular space while ZIBG2 was mostly on the cell surface. Stimulation of MIN6 cells with high concentrations of extracellular glucose (30 mM) triggered a transient rise of the fluorescence of R-GECO1 in cells (**Figure 16**). Meanwhile, we observed a sustained high fluorescence of ZIBG2 when cells were bathed in high glucose. The fluorescence of ZIBG2 decreased quickly to the basal level when cells were washed with low glucose (2 mM) solution. The result suggests that either the release of Zn^{2+} from MIN6 is continuous when

the cells are in high glucose solutions, or the affinity or dissociation rate (k_{off}) of ZIBG2 hinders the diffusion of bound Zn^{2+} from ZIBG2 indicator molecules. Nevertheless, the data demonstrated the feasibility of using two genetically encoded indicators to monitor the dynamics of Zn2+ and Ca2+ in β-cells concurrently.

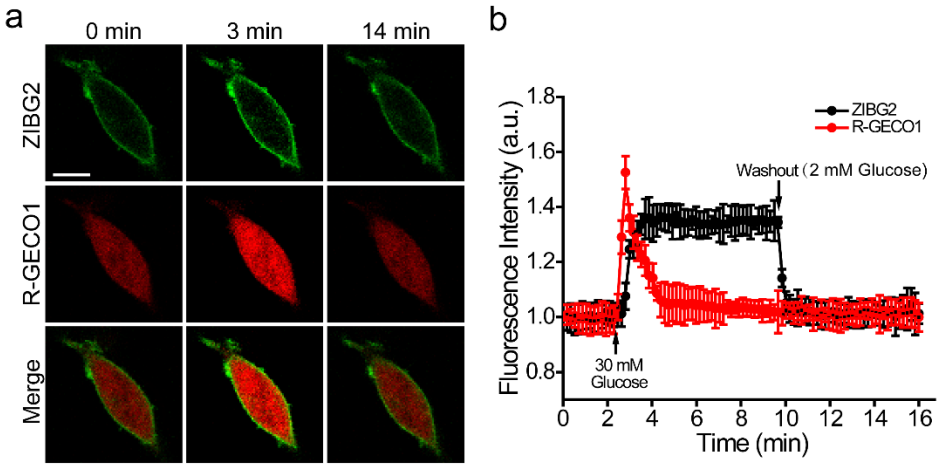

Figure 16. Fluorescence imaging of glucose-induced Zn^{2+} and Ca^{2+} dynamics in MIN6 cells. (a) Fluorescence images of cells expressing ZIBG2 on the cell surface and R-GECO1 intracellularly. Scale bar: 20 μm. (b) Quantitative results for intensity changes of ZIBG2 and R-GECO1 presented as mean and s.d. of 8 cells from three independent replicates. The arrow indicates the time point for addition of high glucose (30 mM) and washout with low glucose (2 mM).

2.3.6. Imaging of Zn^{2+} and Ca^{2+} Dynamics in Mouse and Human Pancreatic islets

Islet transplant is the only minimally invasive cell therapy that is able to achieve glycemic control without exogenous insulin. However, islet transplant shows variable success rates, and inconsistent quality of human islet preparations is a key contributor to this problem.[32] Except for an *in vivo* potency assay in animals which requires several weeks to complete, no reliable method is available to evaluate the functional quality of islets.[50, 51]

In this context, we explored the use of genetically encoded Zn^{2+} and Ca^{2+} indicators to examine the functional potency of mouse and human islets.

We transfected mouse islets with pDisplay-ZIBG2 and R-GECO1. Next, we sequentially perfused the islets trapped in a microfluidic device with a series of solutions. Fluorescence increase of ZIBG2 was observed in response to high glucose (14 mM) or KCl (30 mM). This observation is consistent with our Ca^{2+} imaging result, indicated by the fluorescence of R-GECO1 (**Figure 17ab**). Islet function is known to decrease under hypoxia. When we cultured our transfected islets under a hypoxia condition (1% O_2) for 1

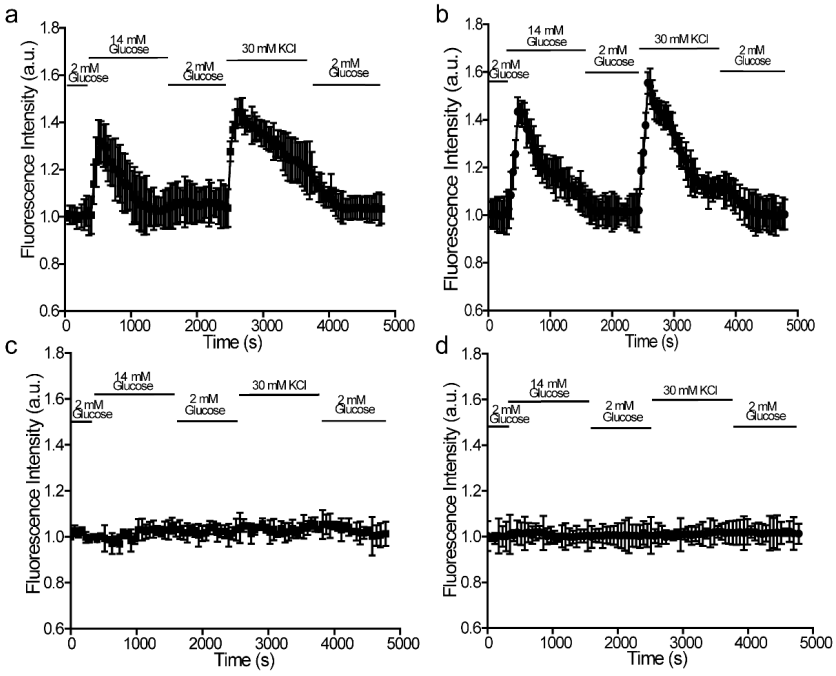

Figure 17. Imaging of Zn^{2+} and Ca^{2+} dynamics in mouse pancreatic islets before (ab) and after (cd) hypoxia treatment. (ac) Temporal Zn^{2+} secretion profiles of C57/B6 mouse islets (indicated by the fluorescence of cell surface-localized ZIBG2) perfused with basal and stimulatory glucose and KCl solutions. (bd) Temporal intracellular Ca^{2+} profiles of C57/B6 mouse islets (indicated by the fluorescence of intracellular R-GECO1) perfused with basal and stimulatory glucose and KCl solutions. Data are presented as mean and s.d. of 8 cells. This experiment was repeated three times.

hour before imaging assays, we observed neither intracellular Ca^{2+} rise nor extracellular Zn^{2+} secretion (**Figure 17cd**). All of these results suggest that Ca^{2+} and Zn^{2+} dynamics may be used as indicators for islet function and potency. Furthermore, we confirmed the function of ZIBG2 in human islets. Upon stimulations with high glucose (25 mM) or KCl (30 mM), a fluorescence increase of ZIBG2 was detected in separate regions of interest within the islets (**Figure 18**). Because islets are big clusters of cells and it is challenging to acquire high-resolution fluorescence images, we dissociated mouse islets into single cells and further examined the localization of ZIBG2. Fluorescence imaging confirmed that ZIBG2 was primarily localized to the cell membrane of primary islets by using pDisplay-ZIBG2 (**Figure 19**).

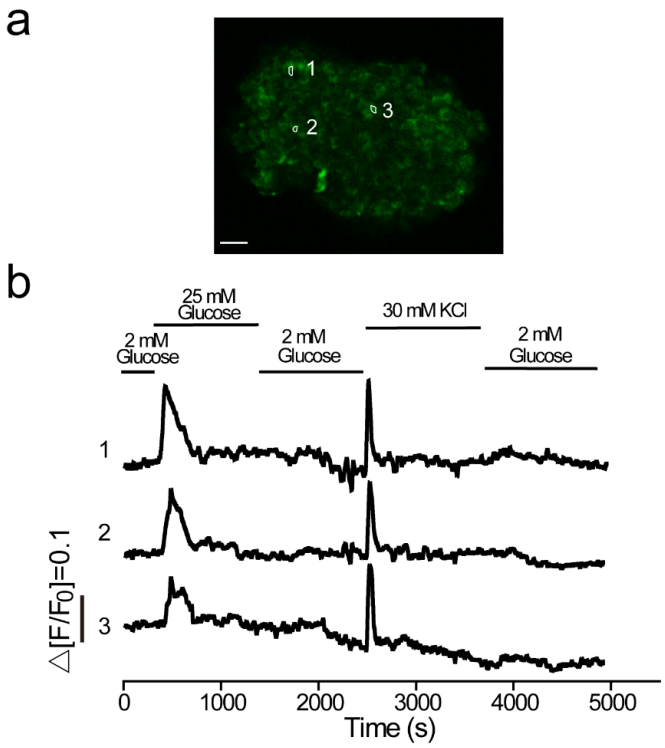

Figure 18. Imaging of temporal Zn^{2+} secretion in human islets perfused with basal and stimulatory glucose and KCl solutions. (a) Fluorescence images of ZIBG2 in a human islet. Scale bar: 50 μm. (b) Quantitative traces for separate regions of interest within the islet in panel a. This experiment was repeated three times.

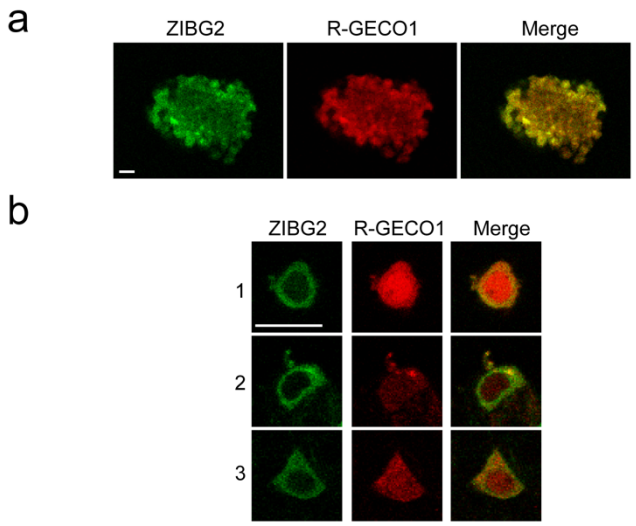

Figure 19. Fluorescence imaging of pDisplay-ZIBG2 in mouse pancreatic islets. (a) An islet cluster co-transfected with ZIBG2 and R-GECO1. (b) Representative single cells dissociated from islet clusters and co-transfected with ZIBG2 and R-GECO1 (scale bars: 50 μm).

2.4. CONCLUSIONS

In this work, we first developed two novel GFP-based GEZIs, ZIBG1 and ZIBG2, which display moderate Zn^{2+} affinity and Zn^{2+}-induced turn-on fluorescence when excited at ~ 480 nm. In particular, ZIBG2 has a dynamic range of 7-fold when operated as an excitation ratiometric indicator and 3-fold when operated as an intensiometric fluorescence turn-on indicator. ZIBG2 can be effectively targeted to the extracellular side of the plasma membrane to detect Zn^{2+} secreted from intracellular vesicles. We have used this photostable ZIBG2 indicator to monitor glucose-induced dynamic Zn^{2+} secretion from mouse insulinoma MIN6 cells, in addition to mouse and human pancreatic islets. Human islet products are widely heterogonous in terms of functionality due to many compounding

factors such as donor characteristics (e.g., age, BMI, gender), organ procurement and transportation (e.g., ischemia time), and isolation factors (e.g., chemical and physical stresses). It is thus only possible to define islet potency and suitability for transplant by examining multiple parameters. We envision the use of genetically encoded Zn^{2+} and Ca^{2+} sensors, in addition to sensors for other insulin secretion coupling factors, to better evaluate islets before transplant. Furthermore, stem-cell-derived β-cells and islets represent a brighter future to make islet transplant widely available. We expect that the sensor genes can be introduced into stem cell lines so that the functional potency of these induced biologics can be evaluated during the differentiation process. We further expect that these powerful screening and optimization tools will be critical for bringing induced islet biologics from laboratories to bedsides. Moreover, in contrast to small molecule-based or hybrid Zn^{2+} sensors, ZIBG2 is fully genetically encoded, so it may be used in tissues or *in vivo* models for long-term monitoring of Zn^{2+} dynamics.

Meanwhile, we further expanded the palette of genetically encoded Zn^{2+} indicators (GEZI) by developing a novel GEZI, frGEZI0.2, with far-red emission. Thus, our work is expected to facilitate multiparametric assays. Since frGEZI0.2 shows robust maturation and high brightness when expressed in mammalian cells, it may have good potential for *in vivo* imaging. Our ongoing work is to further improve the dynamic range and brightness of frGEZIs.

REFERENCES

1. Carter, K. P.; Young, A. M.; Palmer, A. E., Fluorescent sensors for measuring metal ions in living systems. Chem Rev **2014,** 114 (8), 4564-601.
2. Bush, A. I.; Pettingell, W. H.; Multhaup, G.; d Paradis, M.; Vonsattel, J. P.; Gusella, J. F.; Beyreuther, K.; Masters, C. L.; Tanzi, R. E., Rapid induction of Alzheimer A beta amyloid formation by zinc. Science **1994,** 265 (5177), 1464-7.
3. Kapur, J.; Macdonald, R. L., Rapid seizure-induced reduction of benzodiazepine and Zn2+ sensitivity of hippocampal dentate granule cell GABAA receptors. J Neurosci **1997,** 17 (19), 7532-40.
4. Costello, L. C.; Feng, P.; Milon, B.; Tan, M.; Franklin, R. B., Role of zinc in the pathogenesis and treatment of prostate cancer: critical issues to resolve. Prostate Cancer Prostatic Dis **2004,** 7 (2), 111-7.
5. Wei, G.; Hough, C. J.; Li, Y.; Sarvey, J. M., Characterization of extracellular accumulation of Zn2+ during ischemia and reperfusion of hippocampus slices in rat. Neuroscience **2004,** 125 (4), 867-877.
6. Li, Y. V., Zinc and insulin in pancreatic beta-cells. Endocrine **2014,** 45 (2), 178-89.
7. Sandstead, H. H.; Frederickson, C. J.; Penland, J. G., History of zinc as related to brain function. Journal of Nutrition **2000,** 130 (2), 496s-502s.
8. Anderson, C. T.; Kumar, M.; Xiong, S. S.; Tzounopoulos, T., Cell-specific gain modulation by synaptically released zinc in cortical circuits of audition. Elife **2017,** 6.
9. Haug, F. M., Electron microscopical localization of the zinc in hippocampal mossy fibre synapses by a modified sulfide silver procedure. Histochemie **1967,** 8 (4), 355-68.
10. Frederickson, C. J.; Koh, J. Y.; Bush, A. I., The neurobiology of zinc in health and disease. Nat Rev Neurosci **2005,** 6 (6), 449-62.
11. Frederickson, C. J.; Suh, S. W.; Silva, D.; Frederickson, C. J.; Thompson, R. B., Importance of zinc in the central nervous system: the zinc-containing neuron. J. Nutr. **2000,** 130 (5S Suppl), 1471s-83s.
12. Maahs, D. M.; West, N. A.; Lawrence, J. M.; Mayer-Davis, E. J., Epidemiology of type 1 diabetes. Endocrinol. Metab. Clin. North Am. **2010,** 39 (3), 481-97.
13. Gangemi, A.; Salehi, P.; Hatipoglu, B.; Martellotto, J.; Barbaro, B.; Kuechle, J. B.; Qi, M.; Wang, Y.; Pallan, P.; Owens, C.; Bui, J.; West, D.; Kaplan, B.; Benedetti, E.; Oberholzer, J., Islet transplantation for brittle type 1 diabetes: the UIC protocol. Am. J. Transplant. **2008,** 8 (6), 1250-61.
14. Gee, K. R.; Zhou, Z. L.; Qian, W. J.; Kennedy, R., Detection and imaging of zinc secretion from pancreatic beta-cells using a new fluorescent zinc indicator. J. Am. Chem. Soc. **2002,** 124 (5), 776-778.
15. Li, D. L.; Chen, S. W.; Bellomo, E. A.; Tarasov, A. I.; Kaut, C.; Rutter, G. A.; Li, W. H., Imaging dynamic insulin release using a fluorescent zinc indicator for monitoring induced exocytotic release (ZIMIR). Proc. Natl. Acad. Sci. U. S. A. **2011,** 108 (52), 21063-21068.

16. Liu, H. M.; Venkatesan, P.; Wu, S. P., A sensitive and selective fluorescent sensor for Zinc(II) and its application to living cell imaging. Sensor Actuat B-Chem **2014,** 203, 719-725.
17. Walkup, G. K.; Burdette, S. C.; Lippard, S. J.; Tsien, R. Y., A new cell-permeable fluorescent probe for Zn2+. J. Am. Chem. Soc. **2000,** 122 (23), 5644-5645.
18. Santhakumar, H.; Nair, R. V.; Philips, D. S.; Shenoy, S. J.; Thekkuveettil, A.; Ajayaghosh, A.; Jayasree, R. S., Real Time Imaging and Dynamics of Hippocampal Zn2+ under Epileptic Condition Using a Ratiometric Fluorescent Probe. Sci Rep-Uk **2018,** 8.
19. Li, D.; Chen, S.; Bellomo, E. A.; Tarasov, A. I.; Kaut, C.; Rutter, G. A.; Li, W. H., Imaging dynamic insulin release using a fluorescent zinc indicator for monitoring induced exocytotic release (ZIMIR). Proc Natl Acad Sci U S A **2011,** 108 (52), 21063-8.
20. Qin, Y.; Sammond, D. W.; Braselmann, E.; Carpenter, M. C.; Palmer, A. E., Development of an Optical Zn(2+) Probe Based on a Single Fluorescent Protein. ACS Chem. Biol. **2016,** 11 (10), 2744-2751.
21. Chen, Z.; Ai, H. W., Single Fluorescent Protein-Based Indicators for Zinc Ion (Zn(2+)). Anal. Chem. **2016,** 88 (18), 9029-36.
22. Lindenburg, L. H.; Hessels, A. M.; Ebberink, E. H. T. M.; Arts, R.; Merkx, M., Robust Red FRET Sensors Using Self-Associating Fluorescent Domains. ACS Chem. Biol. **2013,** 8 (10), 2133-2139.
23. Hessels, A. M.; Chabosseau, P.; Bakker, M. H.; Engelen, W.; Rutter, G. A.; Taylor, K. M.; Merkx, M., eZinCh-2: A Versatile, Genetically Encoded FRET Sensor for Cytosolic and Intraorganelle Zn2+ Imaging. ACS Chem. Biol. **2015,** 10 (9), 2126-2134.
24. Li, D.; Liu, L.; Li, W. H., Genetic targeting of a small fluorescent zinc indicator to cell surface for monitoring zinc secretion. ACS Chem. Biol. **2015,** 10 (4), 1054-63.
25. Tomat, E.; Nolan, E. M.; Jaworski, J.; Lippard, S. J., Organelle-specific zinc detection using zinpyr-labeled fusion proteins in live cells. J. Am. Chem. Soc. **2008,** 130 (47), 15776-7.
26. Hessels, A. M.; Merkx, M., Genetically-encoded FRET-based sensors for monitoring Zn2+ in living cells. Metallomics **2015,** 7 (2), 258-266.
27. Vinkenborg, J. L.; Nicolson, T. J.; Bellomo, E. A.; Koay, M. S.; Rutter, G. A.; Merkx, M., Genetically encoded FRET sensors to monitor intracellular Zn2+ homeostasis. Nat Methods **2009,** 6 (10), 737-40.
28. Qin, Y.; Dittmer, P. J.; Park, J. G.; Jansen, K. B.; Palmer, A. E., Measuring steady-state and dynamic endoplasmic reticulum and Golgi Zn2+ with genetically encoded sensors. Proc Natl Acad Sci U S A **2011,** 108 (18), 7351-6.
29. Fudge, D. H.; Black, R.; Son, L.; LeJeune, K.; Qin, Y., Optical Recording of Zn(2+) Dynamics in the Mitochondrial Matrix and Intermembrane Space with the GZnP2 Sensor. ACS Chem. Biol. **2018,** 13 (7), 1897-1905.
30. Fudge, D. H.; Black, R.; Son, L.; LeJeune, K.; Qjn, Y., Optical Recording of Zn2+ Dynamics in the Mitochondrial Matrix and Intermembrane Space with the GZnP2 Sensor. Acs Chemical Biology **2018,** 13 (7), 1897-1905.
31. Papas, K. K.; Suszynski, T. M.; Colton, C. K., Islet assessment for transplantation. Current opinion in organ transplantation **2009,** 14 (6), 674-82.

32. Dunn, T. B.; Wilhelm, J. J.; Bellin, M. D.; Pruett, T. L., Autologous islet transplantation: challenges and lessons. Current opinion in organ transplantation **2017,** 22 (4), 364-371.
33. Zhao, Y.; Araki, S.; Wu, J.; Teramoto, T.; Chang, Y. F.; Nakano, M.; Abdelfattah, A. S.; Fujiwara, M.; Ishihara, T.; Nagai, T.; Campbell, R. E., An expanded palette of genetically encoded Ca(2)(+) indicators. Science **2011,** 333 (6051), 1888-91.
34. Kardash, E.; Bandemer, J.; Raz, E., Imaging protein activity in live embryos using fluorescence resonance energy transfer biosensors. Nat Protoc **2011,** 6 (12), 1835-1846.
35. Tsien, R. Y., Fluorescent Indicators of Ion Concentrations. Method Cell Biol **1989,** 30, 127-156.
36. Mamontova, A. V.; Solovyev, I. D.; Savitsky, A. P.; Shakhov Acapital Em, C.; Lukyanov, K. A.; Bogdanov, A. M., Bright GFP with subnanosecond fluorescence lifetime. Scientific reports **2018,** 8 (1), 13224.
37. Brouwer, A. M., Standards for photoluminescence quantum yield measurements in solution (IUPAC Technical Report). Pure Appl Chem **2011,** 83 (12), 2213-2228.
38. Shen, J.; Snook, R. D., Thermal Lens Measurement of Absolute Quantum Yields Using Quenched Fluorescent Samples as References. Chem Phys Lett **1989,** 155 (6), 583-586.
39. Avila, J. G.; Wang, Y.; Barbaro, B.; Gangemi, A.; Qi, M.; Kuechle, J.; Doubleday, N.; Doubleday, M.; Churchill, T.; Salehi, P.; Shapiro, J.; Philipson, L. H.; Benedetti, E.; Lakey, J. R.; Oberholzer, J., Improved outcomes in islet isolation and transplantation by the use of a novel hemoglobin-based O2 carrier. Am J Transplant **2006,** 6 (12), 2861-70.
40. Shapiro, A. M.; Lakey, J. R.; Ryan, E. A.; Korbutt, G. S.; Toth, E.; Warnock, G. L.; Kneteman, N. M.; Rajotte, R. V., Islet transplantation in seven patients with type 1 diabetes mellitus using a glucocorticoid-free immunosuppressive regimen. N. Engl. J. Med. **2000,** 343 (4), 230-8.
41. da Silva Xavier, G.; Varadi, A.; Ainscow, E. K.; Rutter, G. A., Regulation of gene expression by glucose in pancreatic beta -cells (MIN6) via insulin secretion and activation of phosphatidylinositol 3'-kinase. J. Biol. Chem. **2000,** 275 (46), 36269-77.
42. Kennedy, H. J.; Rafiq, I.; Pouli, A. E.; Rutter, G. A., Glucose enhances insulin promoter activity in MIN6 beta-cells independently of changes in intracellular Ca2+ concentration and insulin secretion. Biochem. J. **1999,** 342 (Pt 2), 275-80.
43. Mohammed, J. S.; Wang, Y.; Harvat, T. A.; Oberholzer, J.; Eddington, D. T., Microfluidic device for multimodal characterization of pancreatic islets. Lab Chip **2009,** 9 (1), 97-106.
44. Xing, Y.; Nourmohammadzadeh, M.; Elias, J. E.; Chan, M.; Chen, Z.; McGarrigle, J. J.; Oberholzer, J.; Wang, Y., A pumpless microfluidic device driven by surface tension for pancreatic islet analysis. Biomedical microdevices **2016,** 18 (5), 80.
45. Ai, H. W.; Henderson, J. N.; Remington, S. J.; Campbell, R. E., Directed evolution of a monomeric, bright and photostable version of Clavularia cyan fluorescent protein: structural characterization and applications in fluorescence imaging. Biochem. J. **2006,** 400 (3), 531-40.

46. Kochanczyk, T.; Jakimowicz, P.; Krezel, A., Femtomolar Zn(II) affinity of minimal zinc hook peptides--a promising small tag for protein engineering. Chem Commun (Camb) **2013,** 49 (13), 1312-4.
47. Gautam, S.; Perron, A.; Mutoh, H.; Knopfel, T., Exploration of fluorescent protein voltage probes based on circularly permuted fluorescent proteins. Frontiers in Neuroengineering **2009,** 2 (14).
48. Laviv, T.; Kim, B. B.; Chu, J.; Lam, A. J.; Lin, M. Z.; Yasuda, R., Simultaneous dual-color fluorescence lifetime imaging with novel red-shifted fluorescent proteins. Nature Methods **2016,** 13 (12), 989-+.
49. Ishihara, H.; Asano, T.; Tsukuda, K.; Katagiri, H.; Inukai, K.; Anai, M.; Kikuchi, M.; Yazaki, Y.; Miyazaki, J. I.; Oka, Y., Pancreatic beta cell line MIN6 exhibits characteristics of glucose metabolism and glucose-stimulated insulin secretion similar to those of normal islets. Diabetologia **1993,** 36 (11), 1139-45.
50. Bertuzzi, F.; Ricordi, C., Prediction of clinical outcome in islet allotransplantation. Diabetes Care **2007,** 30 (2), 410-7.
51. Ricordi, C.; Scharp, D. W.; Lacy, P. E., Reversal of diabetes in nude mice after transplantation of fresh and 7-day-cultured (24 degrees C) human pancreatic islets. Transplantation **1988,** 45 (5), 994-6.

Chapter 3

A Fast High-Affinity Fluorescent Serotonin Biosensor Engineered from a Tick Lipocalin

This project was carried out by two lab members in Dr. Ai's lab and collaborator Dr. Mikhail Drobizhev from Montana State University. Shen Zhang developed the biosensors, including library construction and screening, and characterization in purified protein, cultured cell lines, primary cultured neurons, and pancreatic islets. Dr. Xinyu Li conducted experiments on acute brain slices and live animal imaging. Dr. Mikhail Drobizhev determined photophysical parameters and recorded two-photon excitation spectra.

ABSTRACT

Serotonin (5-HT) is an important signaling monoamine in and beyond the central nervous system (CNS). Herein, we report structure-guided engineering of a green fluorescent, genetically encoded serotonin sensor (G-GESS) from a 5-HT-binding lipocalin in the soft tick. G-GESS shows fast response kinetics and high affinity, specificity, brightness, and photostability. We used G-GESS to image 5-HT dynamics *in vitro* and in behaving mice, demonstrating the broad utility of this novel biosensor.

3.1. INTRODUCTION

5-HT has been widely recognized as a key neurotransmitter modulating mood, anxiety, appetite, sleep, sexuality, and learning and memory.[1, 2] 5-HT is also a key hormone in peripheral tissues regulating a large array of processes, including gastrointestinal motility, hematopoiesis, vasoconstriction, insulin secretion, and glucose metabolism.[2, 3] Serotonergic dysregulation has been linked to various pathological conditions, such as depression, schizophrenia, diabetes, obesity, and cardiovascular disorders.[2, 3] A further understanding of molecular, cellular, and circuital mechanisms of 5-HT signaling and the development of corresponding disease intervention strategies require the ability to monitor 5-HT dynamics in biological systems with high specificity and spatiotemporal precision.[1-3]

Microdialysis and fast-scan cyclic voltammetry have been widely used to follow 5-HT dynamics, but are limited in temporal resolution, spatial precision, and/or chemical selectivity.[4, 5] Recent studies have reported several synthetic fluorescent sensors,[6, 7] but the need for long-term, cell-specific, and minimally invasive imaging of 5-HT *in vivo* has not yet been addressed. In this context, there is a great interest to develop genetically encoded 5-HT biosensors.

Previously, microbial periplasmic binding proteins (PBPs) or G-protein coupled receptors (GPCRs) have been integrated with circularly permuted green fluorescent protein (cpGFP) to create powerful, fusion protein biosensors typically expressed at cell surface to detect secreted neurotransmitters and neuromodulators including glutamate, GABA, dopamine, acetylcholine, and norepinephrine.[8-10] Although it is possible to develop similar

biosensors for 5-HT from PBPs or GPCRs, we chose to investigate additional 5-HT-binding proteins due to a few reasons. First, none of the natural PBPs has been identified for 5-HT binding and even though it is possible to re-engineer the binding pocket of a PBP to accommodate 5-HT, it is challenging to achieve high affinity and specificity. On the other hand, GPCR-based biosensors often respond to all molecules that interact with the parental GPCR, resulting in artifacts when GPCR antagonists or agonists are concurrently used.[11] Furthermore, there are concerns about the overexpression of GPCRs, which may perturb cell signaling that is highly organized and tightly controlled.[12]

Blood-feeding arthropods can release soluble, monoamine-binding lipocalin proteins to the feeding site of their hosts to neutralize host inflammatory responses and prevent blood clotting, platelet aggregation, and vasoconstriction.[13, 14] Because of their high binding affinity and specificity, we reasoned that these small (17 kDa) and monomeric lipocalins could be explored to develop novel biosensors for monoamine neurotransmitters. Moreover, the ability to express these proteins in a soluble format in *E. coli* should facilitate high-throughput screening and detailed characterization of resultant biosensors. Furthermore, these proteins are not naturally found in common model organisms, thereby minimizing the interference of derived biosensors with endogenous signaling.

3.2. EXPERIMENTAL SECTION

3.2.1. Materials and General Methods

All chemicals were purchased from Fisher Scientific or Sigma-Aldrich and used without further purification. Synthetic DNA oligos and the genes fragments for AM182

and D7r4 were purchased from Eurofins Genomics or Integrated DNA Technologies. Restriction endonucleases and T4 DNA ligase were purchased from Thermo Fisher. DNA sequences were analyzed by Eurofins Genomics. Phusion High-Fidelity DNA polymerase from Thermo Fisher was used for typical DNA amplification and cloning. Taq DNA polymerase from New England Biolabs was used for error-prone PCR. pCMV(MinDis).iGluSnFR (Addgene plasmid #41732),[15] pAAV-hSyn-CheRiff-eGFP (Addgene plasmid #51697),[16] pLenti-ReaChR-Citrine(Addgene plasmid #50956),[17] and pCMV-R-GECO1 (Addgene Plasmid #32444)[18] were gifts from Drs. Loren Looger, Adam Cohen, Roger Tsien, and Robert Campbell, respectively. pAdDeltaF6 (Addgene plasmid #112867) and pAAV2/9n (Addgene plasmid #112865) were gifts from Dr. James M. Wilson. pMD2G (Addgene plasmid #12259) and psPAX2 (Addgene plasmid #12260) were gifts from Dr. Didier Trono. All animal procedures were conducted in accordance with the protocol approved by the Animal Care and Use Committee at the University of Virginia.

3.2.2. Library Design, Construction, and Screening

We followed a procedure previously reported by Marvin et al.[19] to analyze dihedral angle changes and identify promising sites in AM182 and D7r4 for cpGFP insertion. Next, a cpGFP fragment previously used to develop a genetically encoded H_2S sensor[20] was amplified and inserted to the pre-identified sites using overlap PCR. The product was cloned into a pTorPE plasmid[18] between Sal I and Hind III restriction sites for bacterial periplasmic expression. To generate gene libraries, overlap PCR and oligos containing degenerate codons (NNK) were used to randomize residues on the linkers between cpGFP

and AM182 fragments, whereas error-prone PCR was used to randomize the whole sensor gene. The resultant libraries were subjected to *E. coli* colony-based screening. Colonies were imaged before and after spraying a fine mist of 100 μM serotonin using a previously described setup.[21] Colonies exhibiting changes in fluorescence intensity was identified by using an image processing method described by Kardash et al.[22] Selected clones were individually cultured in 1.8 mL liquid Luria-Bertani (LB) medium supplemented with 0.02% L-arabinose and 200 μg/ml ampicillin with 250 rpm shaking at room temperature for 48 h. Cell lysates were then prepared from bacterial pellets using a lab-made solution containing 0.5% octyl glucoside, 0.1 mg/mL chicken egg lysozyme, and 0.2 U/mL Benzonase in 20 mM Tris-HCl, pH 8. A BioTek Synergy Mx microplate reader was next used to test the responses of cell lysates to 10 μM serotonin. Promising clones were selected for further characterization or another round of protein engineering.

3.2.3. Protein Purification and One-Photon Spectroscopic Characterization

G-GESS in pTorPE was cloned into pBAD/His B and used to transform *E. coli* DH10B cells. Protein expression and Ni-NTA based protein purification were performed as previously described.[23] To remove any aggerate, proteins eluted from Ni-NTA beads were subjected to size-exclusion chromatography through a HiPrep Sephacryl S-200 HR gel filtration column (GE Healthcare) by using an elution buffer containing 100 mM NaCl and 50 mM Tris-HCl, pH 7.4. Resultant proteins were further diluted with the aforementioned elution buffer to a final concentration of ~ 100 nM and used for protein-based assays, including one-photon spectroscopy, selectivity, and binding affinity determination, on a monochromator-based BioTek Synergy Mx plate reader. The peak

extinction coefficients and fractional concentrations of the neutral and anionic forms of G-GESS were obtained by following the changes in one-photon absorption spectra (measured with Lambda 950 spectrophotometer, Perkin-Elmer) upon gradual stepwise alkaline titration by following a previously described protocol.[24] Fluorescence quantum yields of anionic forms were measured in dilute solutions (OD < 0.1) with an absolute method, using Quantaurus-QY (Hamamatsu) integrating sphere fluorimeter by scanning the blue part of absorption peak with a 5-nm step. Quantum yields for G-GESS did not depend on excitation wavelength in the region of 460-480 nm and 460-500 nm in the absence and presence of 5-HT, respectively.

3.2.4. Two-photon Spectral Characterization

Our experimental setup for two-photon spectral measurements includes a tunable femtosecond laser InSight DeepSee Dual (Spectra Physics) coupled with a photon counting spectrofluorimeter PC1 (ISS). The two-photon fluorescence excitation (2PE) spectra were measured by automatically stepping laser wavelength and recording total fluorescence intensity at each step. The detailed description of the experimental setup and measurement protocol has been presented previously.[25] A combination of filters, including FF01-770/SP, BSP01-633R (both Semrock), and HQ535/50 (Chroma) was used in the left emission channel of PC1 spectrofluorimeter to eliminate scattered laser light. To scale the two-photon excitation spectra, we define a parameter called two-photon molecular brightness $F_2(\lambda)$. This parameter depends on excitation wavelength λ. Usually, absorption spectra (both one- and two-photon) of cpGFP-based sensors consist of two spectral bands: one for the neutral GFP chromophore (subscript N in the following), and another for the anionic

GFP chromophore (subscript A in the following). The two forms coexist in equilibrium with the relative fractional concentrations ρ_N and ρ_A ($\rho_N + \rho_A = 1$) that can change upon binding a ligand. The $F_2(\lambda)$ value can be presented as follows: $F_2(\lambda) = \rho_A\varphi_A\sigma_{2,A}(\lambda) + \rho_N\varphi_N\sigma_{2,N}(\lambda)$, where φ is the fluorescence quantum yield of form A or N, and σ_2 is the two-photon absorption cross section. Since we collect fluorescence spectrum through a HQ535/50 filter, technically φ_N only comprises a part of fluorescence originating from anionic deprotonated chromophore that appears after the excited-state proton transfer from initially excited neutral form. To obtain the two-photon excitation spectrum in units of molecular brightness, we independently measured ρ_A, φ_A, and $\sigma_{2,A}(\lambda)$ of the anionic form in the presence or absence of 5-HT and normalized the unscaled 2PE spectrum to the product $\rho_A\varphi_A\sigma_{2,A}(\lambda)$. The cross section $\sigma_{2,A}(\lambda)$ was measured at the wavelength where the contribution of the neutral form is negligible (λ = 940 nm). This measurement was performed using Rhodamine 6G in methanol as a well-characterized reference standard ($\sigma_{2,Rh6G}$ = 9 GM at 940nm).[25] First, spectrally-integrated two-photon excited fluorescence signal I was measured as a function of laser power P for both the sample and reference solutions (samples were held in 3x3 mm cuvettes (Starna) with maximum optical density < 0.1). The total (spectrally integrated) fluorescence was collected at 90° to excitation laser beam through FF01-770/SP (Semrock) and HQ535/50 (Chroma) filters, using the left emission channel of a PC1 spectrofluorimeter working in photon counting mode. The power dependences of fluorescence were fit to a quadratic function $I = aP^2$, from which the coefficients a_S and a_R were obtained for the sample (index S) and reference (index R) solutions, respectively. Second, the one-photon excited fluorescence signals were measured for the same samples and in the same registration conditions. In this case, a

strongly attenuated radiation of a 477-nm line (selected with an interference filter Ealing 35-3565, tilted at 46°) of an IMA101040 ALS (Melles Griot) argon ion laser was used for excitation. The fluorescence power dependences for the sample and reference were measured and fit to a linear function: $I = bP$, from which the coefficients b_S and b_R were obtained. The two-photon absorption cross section was then calculated as follows: $\sigma_{2,S}(\lambda_2) = \frac{a_S}{a_R}\frac{b_R}{b_S}\frac{\varepsilon_S(\lambda_1)}{\varepsilon_R(\lambda_1)}\sigma_{2,R}(\lambda_2)$, where λ_1 is the wavelength used for one-photon excitation (477 nm), λ_2 is the wavelength used for two-photon excitation (940 nm), and $\varepsilon_{R,S}(\lambda_1)$ are the corresponding extinction coefficients, measured at λ_1. This approach allows us to automatically correct for the laser beam properties (pulse duration and spatial intensity distribution), fluorescence collection efficiencies for one- and two-photon modes, PMT spectral sensitivity, differences in quantum yields and concentrations between S and R solutions. Molecular brightness of the anionic form was then calculated as a product $F_2 = \rho_A\varphi_A\sigma_{2,A}(\lambda_m)$ with the 2P cross section taken at spectral maximum, λ_m , for both states of the sensor. The quantum yields, extinction coefficients, and fractional concentrations were all determined independently through one-photon measurement. Finally, the two-photon excitation spectra were scaled to the calculated $F_2(940)$ values.

3.2.5. Construction of Mammalian Expression and Viral Packaging Plasmids

The gene of G-GESS was amplified and used to replace the iGluSnFR gene in pCMV(MinDis).iGluSnFR.[15] Next, a gene fragment encoding Kir2.1-derived Golgi export trafficking signal (KGC) and ER export signal (ER2) (KGC-ER2) was purchased from Eurofins Genomics and inserted to the C-terminus of the PDGFRβ transmembrane (TM) domain, resulting in pmDisplay-G-GESS for sensor expression at the extracellular surface

of mammalian cells. Furthermore, the G-GESS gene fragment fused with the TM domain and KGC-ER2 was amplified from pmDisplay-G-GESS and inserted into either pAAV-hSyn-CheRiff-eGFP[16] between Nco I and EcoR I restriction sites for AAV packaging, or pLenti-ReaChR-Citrine[17] between Age I and EcoR I restriction sites for lentiviral packaging.

3.2.6. Culture and Transfection of Mammalian Cell Lines

HEK 293T and SH-SY5Y were purchased from ATCC and MIN6 is a gift from Dr. Shuibing Chen (Weill Cornell). HEK 293T and MIN6 cells were cultured as previously described.[26] SH-SY5Y cells were cultured in DMEM/F-12 supplemented with 10% FBS, 100 U/mL penicillin, and 100 μg/ mL streptomycin. All cell lines were incubated at 37ºC in a humidified incubator containing 5% CO_2. At 70-80% confluency, cells were transfected with 2 μg of plasmid DNA and 5 μg of lipofectamine 2000 (Thermo Fisher). Transfected cells were then cultured in complete medium for 24-36 h before imaging.

3.2.7. Culture and Transfection of Primary Neurons

Freshly extracted E18 mouse brain tissue was used to prepare dissociated neurons, which were next cultured with 2 mL of NbActiv4 medium (BrainBits) in 35-mm glass bottom culture dishes pre-coated with poly-D-lysine. Every two days, half of the cell culture media was replaced with fresh NbActiv4. Neurons were transfected on day 7 by following BrainBits's protocol. Briefly, 1 mL of culture medium was taken out from each 35 mm dish and combined with another 1 mL of fresh NbActiv4. The conditioned medium was incubated at 37°C and 5% CO_2. A total of 4 μg of plasmid DNA and 8 μL of

Lipofectamine 2000 (Thermo Fisher) were mixed in 100 μL of BrainBits Transfection Medium and the resultant mixture was incubated at room temperature for 15 min. Next, 1 mL of warm, conditioned NbActiv4 medium was used to replace the medium in each 35 mm dish and the transfection mixture was then added. After 3 h of incubation at 37°C in a 5% CO_2 incubator, the medium was exchanged again to the conditioned medium. Half of the culture medium was exchanged every two days. Fluorescence imaging was performed between 48 and 72 hours after transfection.

3.2.8. Fluorescence Imaging of Cultured Cells

Unless otherwise noted, images were acquired using a 40× oil immersion objective lens on an inverted Leica DMi8 microscope equipped with a Leica SPE-II spectral confocal module and a Photometrics Prime 95B Scientific CMOS camera. The confocal module was used to analyze localization. A 488-nm laser was used to excite G-GESS, and emission was collected at 500-700 nm. The wide-field Prime 95B camera and a GFP filter cube with a 470/40 nm bandpass excitation filter and a 525/50 nm bandpass emission filter were used for time-lapse imaging. To image the response of G-GESS at the surface of HEK 293T cells to 5-HT, transfected HEK 293T cells were washed three times with Dulbecco's phosphate-buffered saline (DPBS) before imaging. Images were taken prior to or after addition of serotonin. To image serotonin release in MIN6 cells, transfected MIN6 cells were thoroughly washed and incubated with Hank’s balanced salt solution (HBSS) containing 2.5 mM glucose. After starvation for 40 min, cells were rinsed with fresh HBSS containing 2.5 mM glucose and then retained in the buffer for imaging. Time-lapse images were acquired every 2 seconds. Following the initial ~30 seconds of image acquisition,

MIN6 cells were stimulated with 25 mM glucose and fluorescence imaging continued for an additional 4.5 min. To image serotonin release in SH-SY5Y cells, transfected SH-SY5Y cells were washed with DPBS three times and then retained in the buffer for imaging. After approximately 1 min of initial acquisition, SH-SY5Y cells were stimulated with 0.1 μM nonivamide and fluorescence imaging continued for an additional 6 min. To image the direct response of G-GESS at the surface of primary neurons to 5-HT, transfected neurons were washed three times with Tyrode's buffer (119 mM NaCl, 2.5 mM KCl, 2 mM $CaCl_2$, 2 mM $MgCl_2$, 25 mM HEPES, and 30 mM glucose, pH 7.4) and then retained in the buffer for imaging. Images were taken in the presence or absence of 10 μM serotonin. To image endogenous serotonin release in neurons, an excitatory Tyrode's buffer (32 mM NaCl, 90 mM KCl, 2 mM $CaCl_2$, 2 mM $MgCl_2$, 25 mM HEPES, and 30 mM glucose, pH 7.4) was used for stimulation. The photostability and response kinetics of G-GESS was determined on the surface of HEK 293T cells using an upright Scientifica SliceScope Pro 1000 equipped with a Photometrics Prime 95B Scientific CMOS camera and a CoolLed Enhanced pE-300^{white} LED light source. Photostability was examined by time-lapse imaging when excitation light was left continuously on at either 5% or 100% of the overall intensity. To determine the response kinetics of G-GESS, time-lapse imaging was continuously performed with 10 ms exposure and a small amount of 1 μM 5-HT was locally delivered to a cell of interest through a glass micropipette. A Picospritzer II microinjection dispenser was used to deliver the brief, 10-ms puff of 5-HT.

3.2.9. Preparation of Lentivirus and Adeno-Associated Virus (AAV)

We followed a protocol provided by Addgene and used the following plasmids (prepared from maxiprep) for lentivirus production: pMD2G, psPAX2, and pLenti-hSyn-G-GESS. The viral supernatant was filtered through a 0.45 μm PVDF low protein binding filter unit and further concentrated by PEG-8000 precipitation. Briefly, 4× Lentivirus Concentrator Solution (40% PEG-8000 and 1.2 M NaCl) was mixed with the combined viral supernatant and constantly shaken at 60 RPM and 4°C for 4 h. The solution was then spun down at 1600× g and 4°C for 60 min. Supernatant was removed without disturbing the pellet which contains the lentivirus. Next, the viral pellet was thoroughly resuspended with DPBS containing Ca^{2+} and Mg^{2+} at 1/500 of the original supernatant volume. The viral solution was aliquoted, flash frozen, and stored at -80°C. The plasmids (prepared from maxiprep) used in AAV production were as follows: pAdDeltaF6, pAAV2/9n, and pAAV-hSyn-G-GESS. The AAV packing, purification, and tittering protocol were adopted from Rego et al.[27]

3.2.10. Preparation, Stimulation, and Imaging of Acute Brain Slices

Intracranial stereotactic injection was used to deliver AAV-hSyn-G-GESS or Lenti-hSyn-G-GESS virus into the hippocampus of 8 weeks old BALB/cJ mice (The Jackson Laboratory, Cat. #000651). A total of 3 μL virus was injected at a 1 μL/ min flow rate with the following stereotaxic coordinate: from Bregma, AP +1.7mm, ML +1.2mm, and DV +1.5mm.[28] Once injection was completed, the syringe was left in place for 5 min before being retracted. The surgical wound was closed with animal surgical glue and the animal was left to recover. Three weeks after injection, acute hippocampal slices were prepared

for imaging. Freshly extracted mouse brains were sliced into 350 μm thickness in an ice-cold extracellular solution containing 119 mM NaCl, 2.5 mM KCl, 1.3 mM $MgSO_4$, 1 mM NaH_2PO_4, 26 mM $NaHCO_3$, 2 mM $CaCl_2$, and 10 mM glucose. Next, slices were allowed to recover in the aforementioned slicing solution at 34°C for at least 40 min before being used for experiments. All solutions were continuously bubbled with 95% O_2 and 5% CO_2. A Scientifica SliceScope Pro 1000 equipped with a Photometrics Prime 95B Scientific CMOS camera and a CoolLed Enhanced pE-300^{white} LED light source was used to image evoked serotonin transients in brain slices. The excitation light source was set at 5-10% of the overall intensity and exposure time was set to be 10 ms. Stimulation pulses were generated in the Axon pClamp10 software with Molecular Devices Axon Digidata 1550B and Multiclamp 700B, followed by further amplification with an Agilent/HP 6824A to obtain a pulse amplitude of 30 and 50 V. 20 pulses (500 μs per pulse) at the frequencies of 8 Hz, 16 Hz, 32 Hz, and 64 Hz were used to locally stimulate the hippocampal CA1 region via an FHC cluster bipolar microelectrode (Cat. # 30209). No obvious difference was observed for brain slices prepared from AAV or lentivirus, so the data were analyzed collectively.

3.2.11. *In Vivo* Mouse Imaging

Intracranial stereotactic injection was used to deliver Lenti-hSyn-G-GESS virus was used to deliver Lenti-hSyn-G-GESS virus into the prefrontal cortex (PFC) and primary visual cortex (V1) of BALB/cJ mice (The Jackson Laboratory, Cat. #000651, 6-8 weeks of age) or C57BL/6J mice (The Jackson Laboratory, Cat. #000664, 6-8 weeks of age). The stereotaxic coordinate for the V1 was: from Bregma, AP: +0.5 mm, ML: +2.5 mm, DV:

+0.5 mm.[29] The stereotaxic coordinates for PFC were: from Bregma, AP: +2.8 mm, ML: +0.5 mm, DV: +0.5 mm. A total of 3 μL virus was injected into each mouse at a 1 μL/ min flow rate. Once injection was completed, the syringe was left in place for 5 min before being retracted. The surgical wound was closed with animal surgical glue and the animal was left to recover. One week after viral injection, mice were anesthetized and dexamethasone (Dex, 0.02 ml at 4 mg/ml) was administered by intramuscular injection to quadriceps to reduce cortical stress responses and cerebral edema. A chronic cranial imaging window made from a 3×3 mm round cover glass (no. 1 thickness) and a 5×5 mm cover glass (no. 1 thickness) was installed according to a previously reported protocol.[30] Mice were allowed to recover for additional two weeks and Dex was administered once daily in the first seven days after imaging window installation. The mouse was anesthetized, head-fixed on a holder, and placed under a Scientifica SliceScope Pro 1000 for one-photon imaging. Imaging sessions started when the mouse woke up from anesthesia. MDMA was i.p. delivered at a dose of 10 mg per kg of body weight and images were acquired with a 50-ms exposure and 10-s intervals. Fluvoxamine (Flu) was i.p. delivered at a dose of 2 mg per kg of body weight and images were also acquired with a 50-ms exposure and 10-s intervals. Reserpine (Res) was i.p. delivered at a dose of 0.2 mg per kg of body weight near the end of the imaging session. For the cued fear condition experiment, mice were imaged with a 10-ms exposure and 50-ms intervals. To train mice, a dark slide was shown for 5 s, followed by a white slide for another 5 s and a 1-s electric footshock (0.6 mA) during the showing of the white slide. For each training session, the aforementioned procedure was repeated five times. The training was performed in five sequential days. Mice were next used for analyzing responses to different stimulation conditions.

3.2.12. Data and Statistical Analysis

Microsoft Excel, GraphPad Prism, and Affinity Designer were used to analyze data and prepare figures for publication. Two-way ANOVA with Sidak's multiple comparisons test or unpaired two-tailed t-tests was used to determine all P values. No sample was excluded from data analysis, and no blinding or randomization was employed. Sample size and the number of replications for experiments are presented in figure legends. No statistical methods were used to pre-determine the sample size. Unless otherwise indicated, data are shown as mean and standard deviation (s.d.,) and error bars or shaded areas in all figures represent s.d. Fiji (ImageJ) was used to analyze microscopic images. Imaging background was typically subtracted by setting the rolling ball radius to 300 pixels. Time-lapse images were corrected for motion using the StackReg plugin. Images stacks were corrected for photobleaching by using a linear or exponential decay fitting of baselines. F/F_0 was generated using the "T-functions" plugin in the "Cookbook" menu and the processed thresholded images were pseudocolored with a "Ratio" lookup table.

3.3. RESULTS AND DISCUSSION

3.3.1. Development of G-GESS

We surveyed the literature and identified AM182 from the soft tick *Argas monolakensis* and D7r4 from the malaria mosquito *Anopheles gambiae* as two promising candidates because of their reported high affinity to 5-HT and the availability of relevant protein structures.[13, 14] We reasoned that insertion of cpGFP into these proteins at suitable locations may result in allosteric coupling of ligand binding with cpGFP fluorescence

(**Figure 1a**). To maximize the fluorescence change, successful insertion sites should undergo significant local structural rearrangement to be transduced to modulate the fluorescence of cpGFP. We thus analyzed 5-HT-dependent changes in dihedral angle (defined by the C_α atoms spanning every four sequential residues[19]) on the basis of ligand-bound and ligand-free protein structures. The apo and bound structures of D7r4 were both reported, whereas the structure of AM182 was only available in the 5-HT-bound state.[13, 14] Therefore, we analyzed dihedral angle changes for AM10, a histamine-binding protein homologous to AM182, and identified loops 4, 5 and 9 as promising insertion sites (**Figure 2a-c**). Similarly, we identified loop 2 of D7r4 for possible cpGFP insertion (**Figure 2d-f**).

We next experimentally inserted cpGFP into the identified loops. Insertion at loop 9 of AM182 resulted in a prototypic 5-HT biosensor (G-GESS0.1) showing 5-HT-induced 10% fluorescence increase, whereas other insertion sites led to mutants that are either unresponsive or nonspecifically responsive to 5-HT. We used G-GESS0.1 as the template for further engineering by integrating insertion linker optimization and whole-gene random mutagenesis. We screened the resultant libraries by imaging of *E. coli* colonies on culture plates before and after applying 5-HT, followed by plate reader-based characterization of cell lysates of selected promising clones. Through multiple rounds of evolution (**Figure 3**), we derived G-GESS with an overall 12-fold excitation-ratiometric response to 5-HT and nearly 600% ($\Delta F/F_0$) intensiometric fluorescence turn-on near its major absorbance peak at ~500 nm (**Figure 1a, b**).

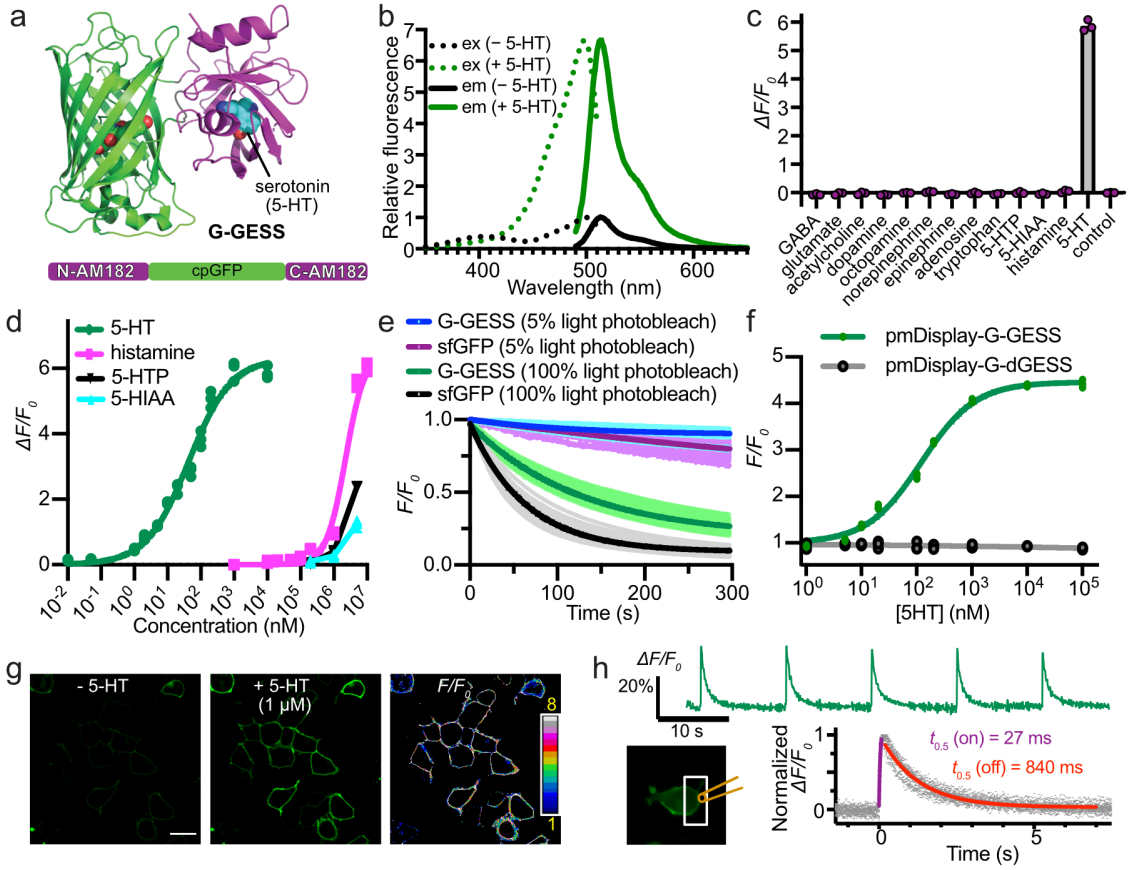

Figure 1. Design and fluorescence characterization of G-GESS.

Figure 1 continued. (**a**) Schematic representation of G-GESS, showing insertion of cpGFP (green) into loop 9 of AM182 (magenta). Also presented at the bottom is the domain arrangement of the primary sequence. (**b**) Excitation (dotted line) and emission (solid line) spectra of purified G-GESS in the presence (green) or absence (black) of 5-HT. Spectra were normalized to the maximal fluorescence of G-GESS in the absence of 10 μM 5-HT. (**c**) Fluorescence of G-GESS in response to the indicated neurotransmitters and other relevant substances (10 μM 5-HT and 100 μM of other molecules), showing high specificity of G-GESS. n =3 for each group. (**d**) Dose-response curve of purified G-GESS, showing nanomolar 5-HT binding (K_d = 43 ± 5 nM) and high selectivity against other structurally similar molecules including histamine (K_d = 2.3 ± 0.4 mM), 5-HTP (K_d > 5 mM), and 5-HIAA (K_d > 5 mM). n =3 for each group. (**e**) Comparison of photobleaching of G-GESS and sfGFP expressed at the surface of HEK 293T on a wide-field microscope equipped with a LED light source at 5% and 100% intensity ($t_{1/2}$ = 126 s for G-GESS and 64 s for sfGFP at 100% intensity). Shown are average and individual traces for 18 cells from 3 cultures for each group. (**f**) Dose-response curve of G-GESS and its dead mutant G-dGESS expressed at the surface of HEK 293T, showing nanomolar binding affinity of G-GESS to 5-HT (K_d = 120 ± 8 nM). n =3 wells of cells per group with 10^5 cells per well. (**g**) Representative fluorescence and pseudocolor ratiometric images of G-GESS expressed at the surface of HEK 293T in the presence or absence of 5-HT. This experiment was repeated three times with similar results using independent cultures. Scale bar, 20 μm. (**h**) Analysis of G-GESS kinetics by puff application of 1 μM 5-HT, showing fast, millisecond-range on and off responses. A representative trace for 5 sequential applications of 5-HT to a single cell is shown at the top. Presented at the bottom are normalized data points for 25 repeats (5 single cells with 5 applications each) fitted for exponential growth and decay.

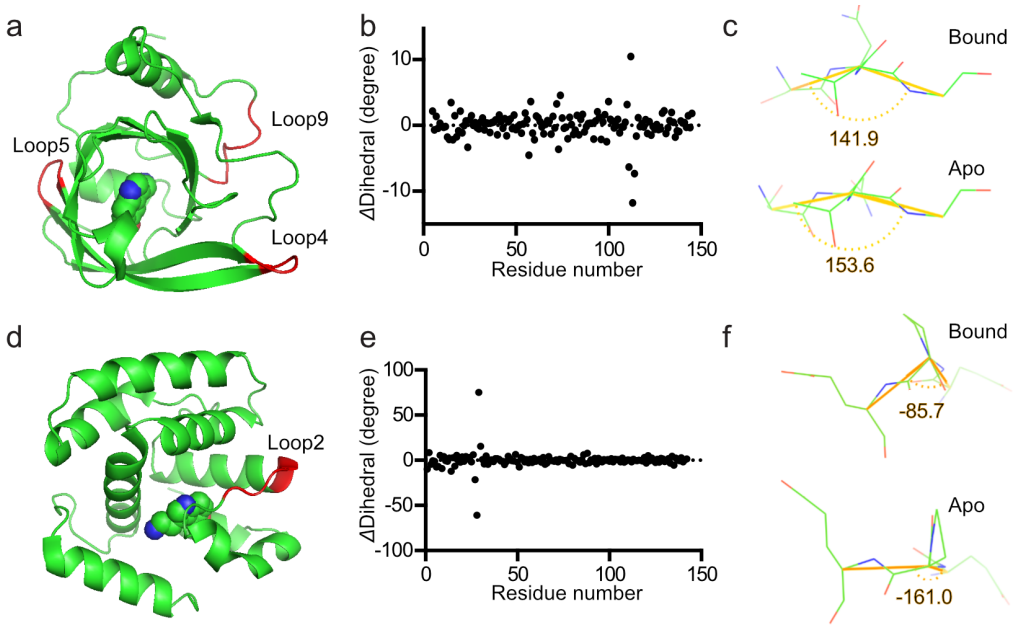

Figure 2. Structural analysis to identify potential cpGFP insertion sites. (**a**) Cartoon presentation of AM10. Loops showing ligand-dependent changes in dihedral angle (defined by the C_α atoms spanning every four sequential residues) are highlighted in red. (**b**) C_α dihedral differences calculated from dihedrals between the ligand-bound (PDB 3BU1) and apo (PDB 3BS2) states of AM10 plotted against residue numbers. (**c**) Dihedral angles for residue 113 of AM10 in the ligand-bound and apo states. (**d**) Cartoon presentation of D7r4. Loop 2 showing a 5-HT-dependent change in dihedral angle is highlighted in red. (**e**) C_α dihedral differences calculated from dihedrals between the ligand-bound (PDB 2QEH) and apo (PDB 2QEV) states of D7r4 plotted against residue numbers. (**f**) Dihedral angles for residue 29 of D7r4 in the ligand-bound and apo states.

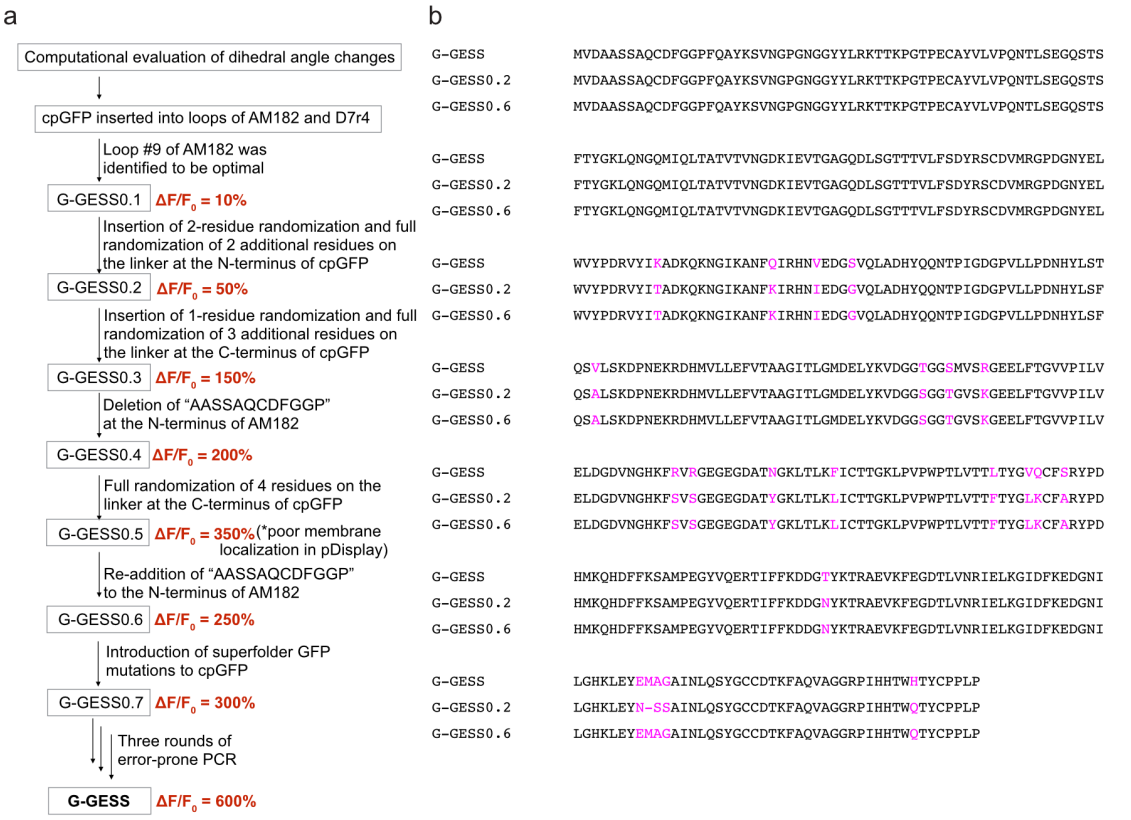

Figure 3. Process to engineer G-GESS.
(**a**) Flowchart to illustrate our integrated, multi-step process to derive G-GESS. $\Delta F/F_0$ for each sensor generation is also presented. From G-GESS0.3 to G-GESS0.4, several N-terminal residues uninvolved in ligand binding were deleted, resulting in increased fluorescence change. However, it was found later in G-GESS0.5 that these residues were important for achieving good cell surface localization, so they were added back to G-GESS0.6. From G-GESS0.6 to G-GESS0.7, superfolder mutations (previously reported for sfGFP) were introduced into the cpGFP fragment of the sensor, resulting in improved brightness and fluorescence change. (**b**) Sequence alignment of G-GESS with two earlier variants.

3.3.2. *In Vitro* Characterization

We determined key photophysical parameters of G-GESS (**Table 1**). When saturated with 5-HT, the intrinsic brightness of G-GESS under one-photon excitation is ~ 70% of EGFP.[31] G-GESS has a broad two-photon excitation with good brightness and large response between 880 and 990 nm (**Table 1** & **Figure 4**). We further tested the specificity of G-GESS against a panel of neurotransmitters and other relevant molecules, and none of these compounds induced a noticeable fluorescence change at physiologically relevant concentrations (**Figure 1c**). Titrating G-GESS with 5-HT revealed a dissociation constant (K_d) of ~ 43 nM with > $5x10^5$-fold selectivity over structurally similar molecules such as histamine, 5-hydroxyindoleacetic acid (5-HIAA), and 5-hydroxytryptophan (5-HTP) (**Figure 1d**).

Table 1. One-photon and two-photon photophysical parameters of G-GESS.

Chromophore charge state	Fluorescence quantum yield φ	Extinction coefficient ε (M^{-1} cm^{-1}) at λ_{max}	Fractional concentration ρ at pH 7.4	One-photon brightness F_1 [a] (10^3 M^{-1} cm^{-1})	2PA cross section σ_2 (GM) at λ_{2Pmax}	Two-photon brightness F_2 [b] (GM)
In the absence of 5-HT						
Neutral	ND [c]	35,400 at 401 nm	0.94	ND [c]	ND [c]	ND [c]
Anionic	0.80	71,000 at 501 nm	0.06	3.4	27 ± 4 at 940 nm	1.51
In the presence of 5-HT						
Neutral	ND [c]	36,100 at 397 nm	0.51	ND [c]	ND [c]	ND [c]
Anionic	0.66	72,900 at 498 nm	0.49	23.6	33 ± 5 at 940 nm	10.7

[a] F_1 is defined as ε×φ×ρ.
[b] F_2 is defined as σ_2 ×φ×ρ.
[c] Not determined.

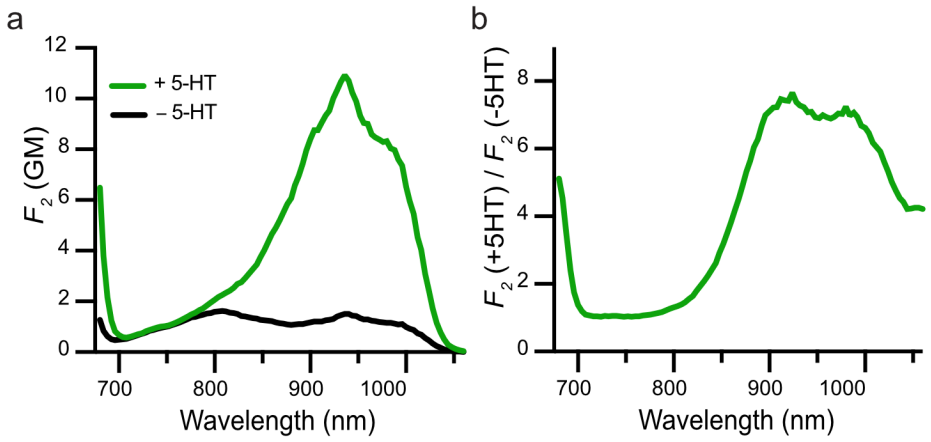

Figure 4. Two-photon fluorescence characterization of G-GESS.

(**a**) Two-photon fluorescence excitation spectra in the presence (green) and absence (black) of 5-HT. (**b**) Ratio of two-photon excitation in the presence over absence of 5-HT plotted against wavelength, suggesting a good performance of G-GESS in two-photon imaging of cells and tissues. G-GESS has high two-photon brightness and large response (ΔF/F = ~ 700%) in a wide spectral range (880-990 nm) matching well with the near-infrared tissue-transparent window.

3.3.3. HEK293T Cells Characterization

We next cloned G-GESS into pmDisplay (**Figure 5**), a modified pDisplay plasmid containing C-terminal Kir2.1-derived Golgi export trafficking signal (KGC) and ER export signal (ER2),[32] and observed excellent localization of G-GESS at the surface of HEK 293T cells (**Figure 6**). G-GESS displayed better photostability than superfolder GFP (sfGFP),[33] and ~ 350% ($\Delta F/F_0$) fluorescence increase in response to 5-HT with a K_d of ~ 120 nM (**Figure 1e-g**). We next monitored the sensor's response to a local application of 5-HT and determined the half-time ($t_{0.5}$) for association and spontaneous dissociation to be 27 ms and 840 ms, respectively (**Figure 1h**). Moreover, we introduced two mutations into G-GESS, resulting in a dead mutant control, G-dGESS (**Figure 7**).

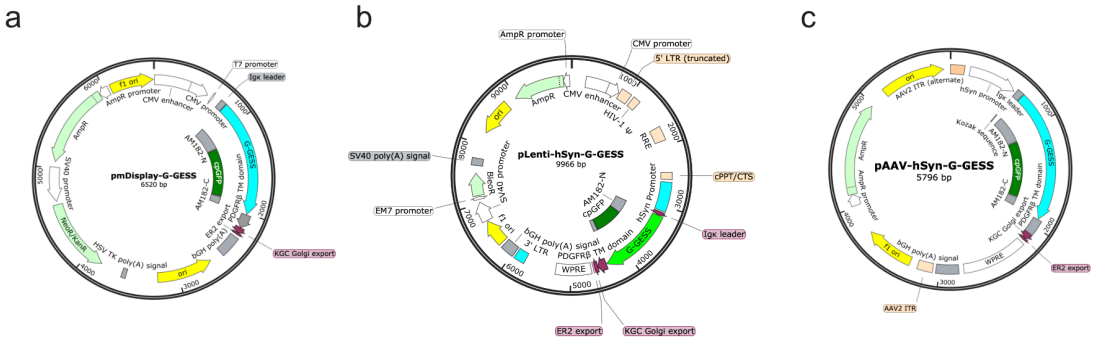

Figure 5. Plasmid maps for mammalian expression of G-GESS.

(**a-c**) Plasmid map for pmDisplay-G-GESS, pLenti-hSyn-G-GESS, pAAV-hSyn-G-GESS, respectively. To localize G-GESS to the extracellular membrane of mammalian cells, an N-terminal IgG κ light chain leader sequence and a C-terminal PDGFRβ transmembrane (TM) domain were appended. In addition, a Kir2.1-derived Golgi export trafficking signal (KGC) and a Kir2.1-derived ER export signal (ER2) were added to the C-terminus. The size of G-GESS is 44 kDa. The minimal element to achieve mammalian membrane localization (G-GESS+PDGFRβ TM) is 50 kDa, whereas the overall size (G-GESS+PDGFRβ TM+KGC+ER2) is 53 kDa, in addition to an autocleavage, 2-kDa IgG κ leader sequence.

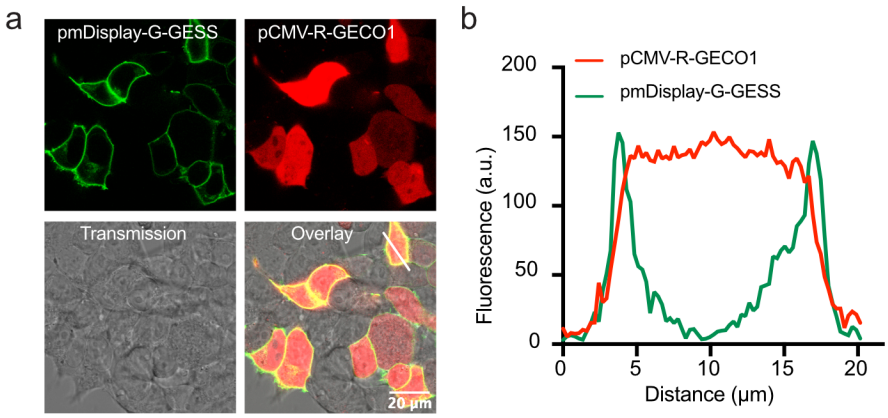

Figure 6. Characterization of pmDisplay-G-GESS membrane localization in HEK 293T cells.

(**a**) Representative fluorescence images of HEK 293T cells co-transfected with pmDisplay-G-GESS and pCMV-R-GECO1, showing excellent membrane localization of G-GESS. Red fluorescent Ca^{2+} sensor R-GECO1 was co-expressed as a whole-cell label. Scale bar, 20 μm. (**b**) Fluorescence intensity measured over the white line shown in the "overlay" image of panel **a**, further confirming excellent membrane localization of G-GESS in mammalian cells. These experiments were repeated three times with similar results using independent cultures.

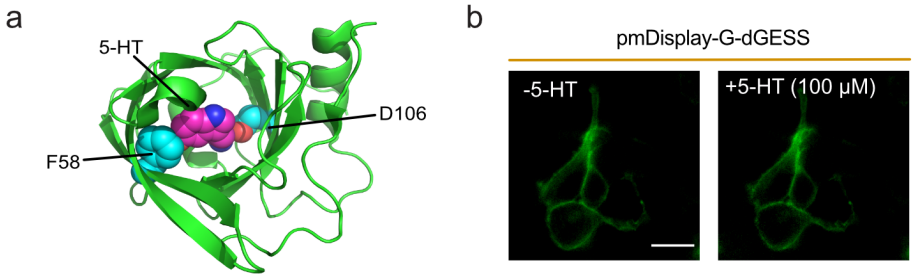

Figure 7. Construction of G-dGESS, a dead mutant of G-GESS.

(**a**) Cartoon presentation of AM182 (PDB 3BRN), highlighting the 5-HT ligand (magenta) and two residues (F58 and D106; colored in cyan and numbered according to PDB 3BRN) important for ligand binding. Mutations corresponding to F58A and D106L were introduced into G-GESS to create a dead mutant named "G-dGESS". (**b**) Representative fluorescence images of G-dGESS expressed at the surface of HEK 293T cells, showing no response to 5-HT. This experiment was repeated three times with similar results using independent cultures. Scale bar, 20 μm.

3.3.4. MIN6 Cells, Neuroblastoma Cells and Cultured Neurons Characterization

We further used G-GESS to monitor physiological 5-HT dynamics. 5-HT is suggested to be synthesized and released from pancreatic β-cells to modulate insulin secretion and islet function.[34] However, it has been challenging to directly observe glucose-induced 5-HT secretion.[35] We expressed G-GESS at the surface of mouse MIN6 β-cells and observed ~ 25% fluorescent increase, indicating a successful detection of 5-HT secretion triggered by high glucose (**Figure 8a,b**). Furthermore, we expressed G-GESS in SH-SY5Y neuroblastoma cells and primary mouse neurons, and imaged 5-HT secretion in response to nonivamide[36] and high potassium induced membrane polarization, respectively (**Figure 8c-f**). G-dGESS was unresponsive under these conditions.

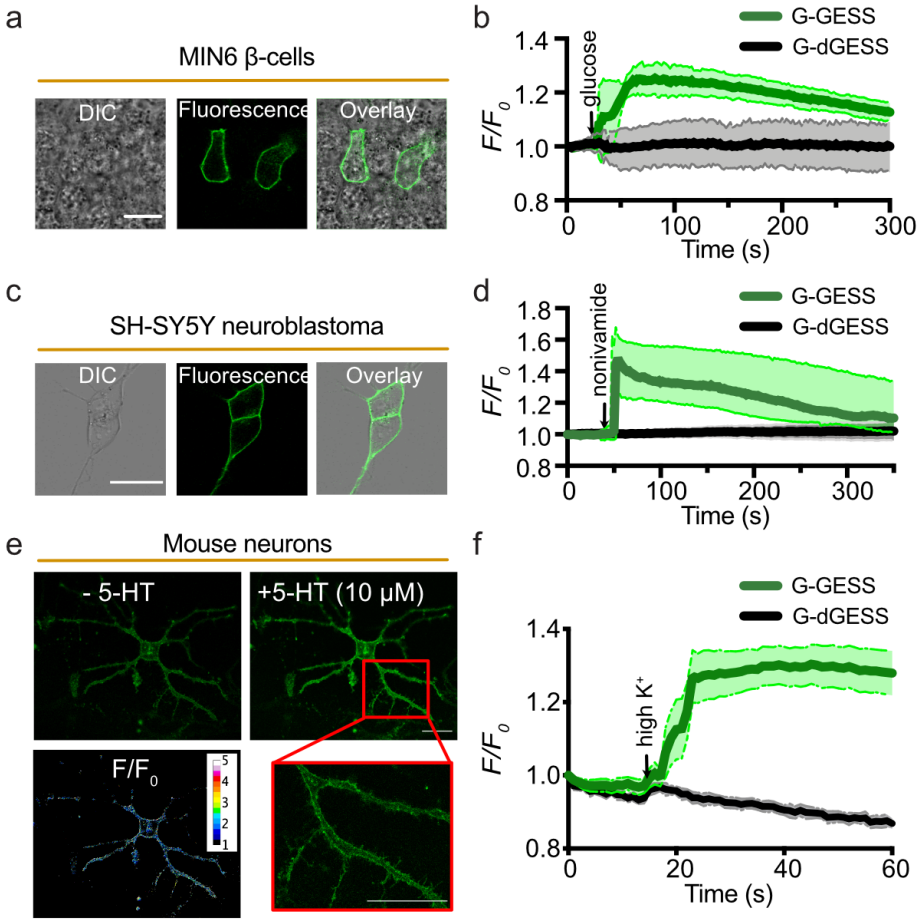

Figure 8. Imaging of 5-HT release in β-cells, neuroblastoma cells, and primary mouse neurons.

(**a**) Representative images of G-GESS expressed at the surface of mouse pancreatic MIN6 β-cells. Scale bar, 20 μm. (**b**) Fluorescence traces of G-GESS in response to high glucose (25 mM), showing glucose-induced 5-HT secretion from β-cells. n=7 cells for G-GESS and 6 cells for G-dGESS from 3 independent repeats. (**c**) Representative images of G-GESS expressed at the surface of SH-SY5Y neuroblastoma cells. Scale bar, 20 μm. (**d**) Fluorescence traces of G-GESS in response to nonivamide (0.1 μM), showing nonivamide-induced 5-HT secretion from neuroblastoma. n=13 cells from 3 repeats for each group. (**e**) Representative images of G-GESS expressed at the surface of primary mouse neurons in response to 5-HT (10 μM). Also shown is a pseudocolor ratiometric image of the neuron in the presence over absence of 5-HT. Scale bar, 20 μm. This experiment was repeated three times with similar results using independent cultures. (**f**) Fluorescence traces of G-GESS at the surface of primary mouse neurons, showing 5-HT secretion in response to high potassium induced membrane polarization. n=19 cells for G-GESS and 12 cells for G-dGESS from 4 repeats. Shaded areas of F/F_0 traces indicate s.d.

3.3.5. Acute Brain Slices Characterization

To examine the function of G-GESS in acute brain slices, we injected G-GESS or G-dGESS lentivirus or adeno-associated virus (AAV) to the mouse hippocampus and prepared acute brain slices three weeks after infection (**Figure. 9a, b**). We detected up to 35% fluorescence increase with excellent signal-to-noise ratio from G-GESS in the hippocampal CA1 region following extracellular field stimulation. The kinetics and magnitude of such responses are dependent on stimulation voltage and frequency (**Figure 9c-f**). In contrast, no fluorescence change was observed for G-dGESS stimulated by the same pulses.

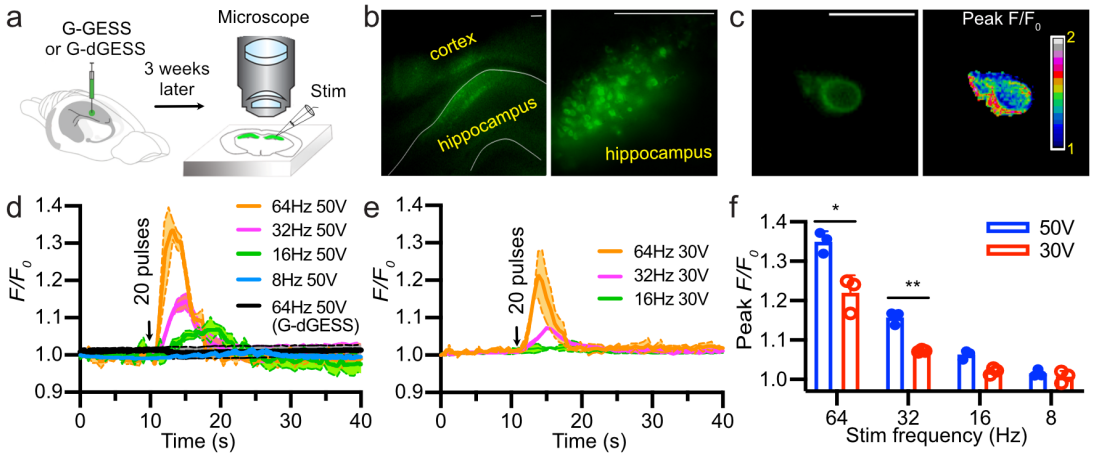

Figure 9. Imaging of 5-HT release in acute mouse brain slices.

(**a**) Schematic diagram illustrating the preparation of acute mouse brain slices with viral expression of G-GESS in the hippocampus. (**b**) Representative fluorescence images of G-GESS-expressing mouse brain slices. Scale bar, 200 μm. (**c**) Representative fluorescence images of G-GESS-expressing hippocampal neurons in mouse brain slices in response to electrical stimuli (20 pulses at 64 Hz). Also shown is a pseudocolor ratiometric image (peak F/F_0) of a representative neuron. Scale bar, 20 μm. (**d**) Fluorescence traces of G-GESS in response to 20 pulses of electric stimuli at 50 V and the indicated frequencies.

Figure 9 continued. (**e**) Fluorescence traces of G-GESS in response to 20 pulses of electric stimuli at 30 V and the indicated frequencies. (**f**) Maximal fluorescence ratio change (peak F/F_0) plotted against stimulation frequency at 50 V or 30 V, showing that the magnitude of the change is dependent on stimulation voltage and frequency (**P*= 0.0015, ***P*= 0.021, significance determined by 2-way ANOVA with Sidak's multiple comparisons test). n=3 slices from 2 mice for each group. Shaded areas of F/F_0 traces indicate s.d.

3.3.6. Live Mice Imaging

To examine whether G-GESS can reveal the spatiotemporal releases of 5-HT in live mice, we expressed G-GESS in the prefrontal cortex (PFC) and i.p. administered methylenedioxymethamphetamine (MDMA), a compound known to stimulate the release of 5-HT in the brain.[37] The fluorescence of G-GESS was followed through a pre-installed cranial imaging window and a robust, 57% fluorescence increase was observed (**Figure 10a-c**). Similarly, we examined the response of G-GESS to fluvoxamine (Flu), a well-established selective serotonin reuptake inhibitor.[38] Flu elicited the rise of G-GESS fluorescence, which can be reversed by reserpine (Res), a vesicular monoamine transporter inhibitor known to deplete extracellular 5-HT (**Figure 10d**).[39] G-dGESS or injection of saline led to no obvious response during these conditions.

Finally, we tested whether G-GESS can detect physiological 5-HT transients in response to behavioral stimuli. G-GESS was expressed in mouse primary visual cortex (V1) and cued fear conditioning was used to induce endogenous 5-HT changes (**Figure 10e-i**). A dark-light transition was established and footshock stress was introduced during the light condition. Expected and unexpected footshock evoked ~16% and ~10% of fluorescence rise, respectively, while visual stimulation alone caused nearly 5% increase.

The response of G-GESS to footshock and visual stimulation during the day 1 training was only ~3%. No response was observed for G-dGESS. These results collectively suggest that the learning process reinforced 5-HT responses in visual cortex and G-GESS can reveal such transient, physiological 5-HT dynamics.

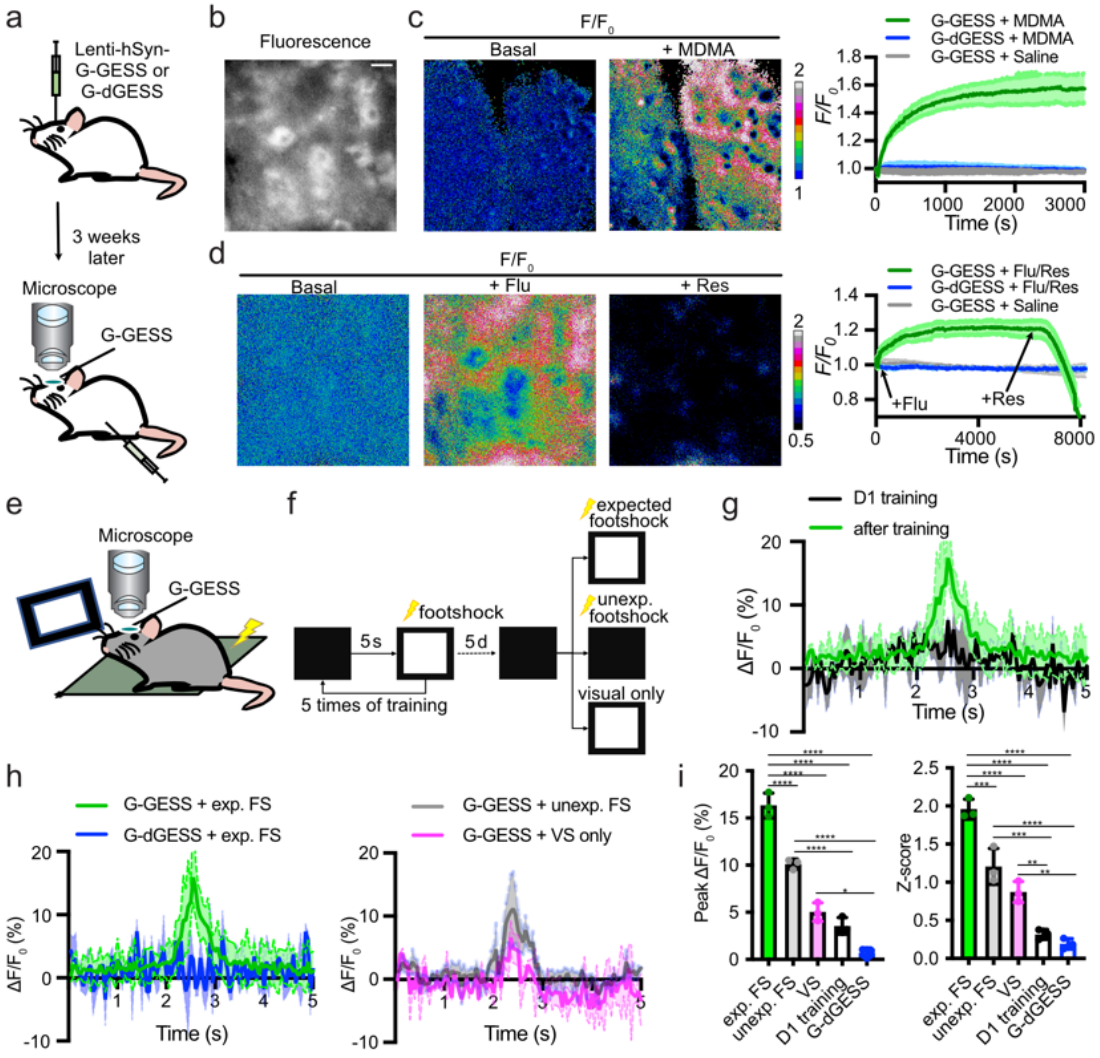

Figure 10. Imaging of endogenous 5-HT dynamics with G-GESS in mice.

Figure 10 continued. (**a**) Schematic diagram illustrating viral expression and *in vivo* imaging of G-GESS in the PFC of head-fixed mice. (**b**) Representative fluorescence image of G-GESS one-photon microscopy. Scale bar, 20 μm. (**c**) Representative ratiometric images and average intensity traces upon MDMA (10 mg/kg, i.p.) administration. G-dGESS and saline injection were used as the control groups. (**d**) Representative ratiometric images and average intensity traces after fluvoxamine (flu, 2 mg/kg, i.p.) and reserpine (Res, 0.2 mg/kg, i.p.) treatments. (**e**) Schematic diagram illustrating a cued fear conditioning experiment, including visual cue (dark-light transition) and footshock stress. (**f**) Schematic diagram illustrating the training and experimental process. During the training, a dark slide was shown to mice for 5 s, followed by a white slide for 5 s during which a 1-s electric footshock was given. After training for 5 days, three conditions were presented to mice. (**g**) Representative average fluorescence traces for G-GESS during Day 1 training and after training. n=3 mice for each group and each mouse for 5 times of stimulation. (**h**) Representative average fluorescence traces for G-GESS and G-dGESS after training in response to the indicated stimulation conditions. n=3 mice for each group and each mouse for 5 times of stimulation. (**i**) Normalized average peak fluorescence change ($\Delta F/F_0$) and Z-score for the indicated 5 experimental groups (****P<0.0001, ***P<0.001, **P<0.01, *P<0.1, significance determined by 1-way ANOVA with Tukey's multiple comparisons test). n=3 mice for each group.

3.4. CONCLUSIONS

In summary, using a structure-guided protein engineering workflow, we developed the first lipocalin-based 5-HT sensor by inserting a cpGFP into a 5-HT-binding protein from the soft tick. G-GESS is a robust sensor with excellent fluorescence change, brightness, photostability, specificity, and fast millisecond-range kinetics and nanomolar affinity. We used G-GESS to image physiological 5-HT changes in β-cells, neuroblastoma, primary neurons, and acute brain slices. We further imaged 5-HT dynamics in the brains of live mice in response to drugs and behavioral triggers. Since 5-HT plays important roles both within and beyond the CNS, G-GESS will enable a large array of studies in various

biological systems. Although we here focus on the use of G-GESS at cell surface to detect secreted 5-HT, we envision that G-GESS can also be targeted to cellular subdomains to monitor intracellular 5-HT because, intrinsically, G-GESS is not a membrane protein. Furthermore, in comparison to PBP- or GPCR-based neurotransmitter biosensors, G-GESS is relatively small in size, facilitating the potential use of viral vectors, often with limited packaging capacities, to deliver multiple genes. In addition, diverse lipocalins exist in nature[40] and the lipocalin scaffold has been exploited in laboratories for engineering of antibody mimetics.[41] Therefore, there is a great opportunity to use the knowledge we gained in this study to drastically expand lipocalin-derived fluorescent biosensors.

To the best of our knowledge, Dr. Lin Tian at UC Davis and Dr. Yulong Li at Peking University are also working on genetically encoded serotonin sensors, with the names of iSeroSnFR (not published) and $GRAB_{5\text{-}HT}$,[42] respectively. Our G-GESS sensors are based on a strategy different from theirs. Thus, we expect that each of these sensors will have different properties, are best suited for different applications, and can complement each other to answer biological questions. Together, this collection of studies will result in a toolbox of genetically encoded biosensors for serotonin.

REFERENCES

1. Gordon, J. A.; Hen, R., The serotonergic system and anxiety. Neuromolecular Med. **2004,** 5 (1), 27-40.
2. Berger, M.; Gray, J. A.; Roth, B. L., The expanded biology of serotonin. Annu. Rev. Med. **2009,** 60, 355-66.
3. Lv, J.; Liu, F., The Role of Serotonin beyond the Central Nervous System during Embryogenesis. Frontiers in cellular neuroscience **2017,** 11, 74.

4. Chefer, V. I.; Thompson, A. C.; Zapata, A.; Shippenberg, T. S., Overview of brain microdialysis. Curr Protoc Neurosci **2009,** Chapter 7, Unit7 1.
5. Puthongkham, P.; Venton, B. J., Recent advances in fast-scan cyclic voltammetry. Analyst **2020,** 145 (4), 1087-1102.
6. Jeong, S.; Yang, D.; Beyene, A. G.; Del Bonis-O'Donnell, J. T.; Gest, A. M. M.; Navarro, N.; Sun, X.; Landry, M. P., High-throughput evolution of near-infrared serotonin nanosensors. Sci Adv **2019,** 5 (12), eaay3771.
7. Hettie, K. S.; Glass, T. E., Turn-On Near-Infrared Fluorescent Sensor for Selectively Imaging Serotonin. ACS chemical neuroscience **2016,** 7 (1), 21-5.
8. Marvin, J. S.; Borghuis, B. G.; Tian, L.; Cichon, J.; Harnett, M. T.; Akerboom, J.; Gordus, A.; Renninger, S. L.; Chen, T. W.; Bargmann, C. I.; Orger, M. B.; Schreiter, E. R.; Demb, J. B.; Gan, W. B.; Hires, S. A.; Looger, L. L., An optimized fluorescent probe for visualizing glutamate neurotransmission. Nat. Methods **2013,** 10 (2), 162-70.
9. Wang, H.; Jing, M.; Li, Y., Lighting up the brain: genetically encoded fluorescent sensors for imaging neurotransmitters and neuromodulators. Curr. Opin. Neurobiol. **2018,** 50, 171-178.
10. Patriarchi, T.; Cho, J. R.; Merten, K.; Howe, M. W.; Marley, A.; Xiong, W. H.; Folk, R. W.; Broussard, G. J.; Liang, R.; Jang, M. J.; Zhong, H.; Dombeck, D.; von Zastrow, M.; Nimmerjahn, A.; Gradinaru, V.; Williams, J. T.; Tian, L., Ultrafast neuronal imaging of dopamine dynamics with designed genetically encoded sensors. Science **2018,** 360 (6396).
11. Borden, P. M.; Zhang, P.; Shivange, A. V.; Marvin, J. S.; Cichon, J.; Dan, C.; Podgorski, K.; Figueiredo, A.; Novak, O.; Tanimoto, M.; Shigetomi, E.; Lobas, M. A.; Kim, H.; Zhu, P. K.; Zhang, Y.; Zheng, W. S.; Fan, C.; Wang, G.; Xiang, B.; Gan, L.; Zhang, G.-X.; Guo, K.; Lin, L.; Cai, Y.; Yee, A. G.; Aggarwal, A.; Ford, C. P.; Rees, D. C.; Dietrich, D.; Khakh, B. S.; Dittman, J. S.; Gan, W.-B.; Koyama, M.; Jayaraman, V.; Cheer, J. F.; Lester, H. A.; Zhu, J. J.; Looger, L. L., A fast genetically encoded fluorescent sensor for faithful in vivo acetylcholine detection in mice, fish, worms and flies. bioRxiv **2020**, 2020.02.07.939504.
12. Tubio, M. R.; Fernandez, N.; Fitzsimons, C. P.; Copsel, S.; Santiago, S.; Shayo, C.; Davio, C.; Monczor, F., Expression of a G protein-coupled receptor (GPCR) leads to attenuation of signaling by other GPCRs: experimental evidence for a spontaneous GPCR constitutive inactive form. J. Biol. Chem. **2010,** 285 (20), 14990-8.
13. Mans, B. J.; Ribeiro, J. M.; Andersen, J. F., Structure, function, and evolution of biogenic amine-binding proteins in soft ticks. J. Biol. Chem. **2008,** 283 (27), 18721-33.
14. Mans, B. J.; Calvo, E.; Ribeiro, J. M.; Andersen, J. F., The crystal structure of D7r4, a salivary biogenic amine-binding protein from the malaria mosquito Anopheles gambiae. J. Biol. Chem. **2007,** 282 (50), 36626-33.
15. Marvin, J. S.; Borghuis, B. G.; Tian, L.; Cichon, J.; Harnett, M. T.; Akerboom, J.; Gordus, A.; Renninger, S. L.; Chen, T.-W.; Bargmann, C. I.; Orger, M. B.; Schreiter, E. R.; Demb, J. B.; Gan, W.-B.; Hires, S. A.; Looger, L. L., An optimized fluorescent probe for visualizing glutamate neurotransmission. Nature methods **2013,** 10, 162.
16. Hochbaum, D. R.; Zhao, Y.; Farhi, S. L.; Klapoetke, N.; Werley, C. A.; Kapoor, V.; Zou, P.; Kralj, J. M.; Maclaurin, D.; Smedemark-Margulies, N.; Saulnier, J. L.; Boulting, G. L.; Straub, C.; Cho, Y. K.; Melkonian, M.; Wong, G. K.-S.; Harrison, D.

J.; Murthy, V. N.; Sabatini, B. L.; Boyden, E. S.; Campbell, R. E.; Cohen, A. E., All-optical electrophysiology in mammalian neurons using engineered microbial rhodopsins. Nature methods **2014,** 11 (8), 825-833.
17. Lin, J. Y.; Knutsen, P. M.; Muller, A.; Kleinfeld, D.; Tsien, R. Y., ReaChR: a red-shifted variant of channelrhodopsin enables deep transcranial optogenetic excitation. Nature Neuroscience **2013,** 16 (10), 1499-1508.
18. Zhao, Y.; Araki, S.; Wu, J.; Teramoto, T.; Chang, Y. F.; Nakano, M.; Abdelfattah, A. S.; Fujiwara, M.; Ishihara, T.; Nagai, T.; Campbell, R. E., An expanded palette of genetically encoded Ca(2)(+) indicators. Science **2011,** 333 (6051), 1888-91.
19. Marvin, J. S.; Schreiter, E. R.; Echevarría, I. M.; Looger, L. L., A genetically encoded, high-signal-to-noise maltose sensor. Proteins **2011,** 79 (11), 3025-36.
20. Chen, S.; Chen, Z. J.; Ren, W.; Ai, H. W., Reaction-based genetically encoded fluorescent hydrogen sulfide sensors. J. Am. Chem. Soc. **2012,** 134 (23), 9589-92.
21. Fan, Y.; Chen, Z.; Ai, H. W., Monitoring redox dynamics in living cells with a redox-sensitive red fluorescent protein. Anal. Chem. **2015,** 87, 2802-2810.
22. Kardash, E.; Bandemer, J.; Raz, E., Imaging protein activity in live embryos using fluorescence resonance energy transfer biosensors. Nature protocols **2011,** 6 (12), 1835-1846.
23. Chen, Z.; Ai, H. W., Single Fluorescent Protein-Based Indicators for Zinc Ion (Zn(2+)). Anal. Chem. **2016,** 88 (18), 9029-36.
24. Molina, R. S.; Qian, Y.; Wu, J.; Shen, Y.; Campbell, R. E.; Drobizhev, M.; Hughes, T. E., Understanding the Fluorescence Change in Red Genetically Encoded Calcium Ion Indicators. Biophys. J. **2019,** 116 (10), 1873-1886.
25. Drobizhev, M.; Molina, R. S.; Hughes, T. E., Characterizing the Two-photon Absorption Properties of Fluorescent Molecules in the 680-1300 nm Spectral Range. Bio-protocol **2020,** 10 (2), e3498.
26. Chen, M.; Zhang, S.; Xing, Y.; Li, X.; He, Y.; Wang, Y.; Oberholzer, J.; Ai, H. W., Genetically Encoded, Photostable Indicators to Image Dynamic Zn(2+) Secretion of Pancreatic Islets. Anal. Chem. **2019**, DOI: 10.1021/acs.analchem.9b01802.
27. Rego, M.; Hanley, L. M.; Ersing, I.; Guerin, K.; Tasissa, M.; Haery, L.; Mueller, I.; Sanders, E.; Fan, M., Improved yield of AAV2 and rAAV2-retro serotypes following sugar supplementation during the viral production phase. bioRxiv **2018**, 488585.
28. Tetteh, H.; Lee, J.; Lee, J.; Kim, J. G.; Yang, S., Investigating Long-term Synaptic Plasticity in Interlamellar Hippocampus CA1 by Electrophysiological Field Recording. J. Vis. Exp. **2019,** (150).
29. Beltramo, R.; Scanziani, M., A collicular visual cortex: Neocortical space for an ancient midbrain visual structure. Science **2019,** 363 (6422), 64-69.
30. Holtmaat, A.; Bonhoeffer, T.; Chow, D. K.; Chuckowree, J.; De Paola, V.; Hofer, S. B.; Hübener, M.; Keck, T.; Knott, G.; Lee, W. C.; Mostany, R.; Mrsic-Flogel, T. D.; Nedivi, E.; Portera-Cailliau, C.; Svoboda, K.; Trachtenberg, J. T.; Wilbrecht, L., Long-term, high-resolution imaging in the mouse neocortex through a chronic cranial window. Nat. Protoc. **2009,** 4 (8), 1128-44.
31. Shaner, N. C.; Steinbach, P. A.; Tsien, R. Y., A guide to choosing fluorescent proteins. Nat. Methods **2005,** 2 (12), 905-9.

32. Hofherr, A.; Fakler, B.; Klöcker, N., Selective Golgi export of Kir2.1 controls the stoichiometry of functional Kir2.x channel heteromers. J. Cell Sci. **2005,** 118 (Pt 9), 1935-43.
33. Pedelacq, J. D.; Cabantous, S.; Tran, T.; Terwilliger, T. C.; Waldo, G. S., Engineering and characterization of a superfolder green fluorescent protein. Nat. Biotechnol. **2006,** 24 (1), 79-88.
34. Cataldo Bascuñan, L. R.; Lyons, C.; Bennet, H.; Artner, I.; Fex, M., Serotonergic regulation of insulin secretion. Acta Physiol. (Oxf.) **2019,** 225 (1), e13101.
35. Almaca, J.; Molina, J.; Menegaz, D.; Pronin, A. N.; Tamayo, A.; Slepak, V.; Berggren, P. O.; Caicedo, A., Human Beta Cells Produce and Release Serotonin to Inhibit Glucagon Secretion from Alpha Cells. Cell reports **2016,** 17 (12), 3281-3291.
36. Rohm, B.; Holik, A. K.; Somoza, M. M.; Pignitter, M.; Zaunschirm, M.; Ley, J. P.; Krammer, G. E.; Somoza, V., Nonivamide, a capsaicin analog, increases dopamine and serotonin release in SH-SY5Y cells via a TRPV1-independent pathway. Mol Nutr Food Res **2013,** 57 (11), 2008-18.
37. Fletcher, P. J.; Korth, K. M.; Robinson, S. R.; Baker, G. B., Multiple 5-HT receptors are involved in the effects of acute MDMA treatment: studies on locomotor activity and responding for conditioned reinforcement. Psychopharmacology (Berl.) **2002,** 162 (3), 282-91.
38. Devane, C. L., Fluvoxamine. Neuropsychiatr. Dis. Treat. **2005,** 1 (4), 287.
39. Jacobsen, J. P.; Medvedev, I. O.; Caron, M. G., The 5-HT deficiency theory of depression: perspectives from a naturalistic 5-HT deficiency model, the tryptophan hydroxylase 2Arg439His knockin mouse. Philos Trans R Soc Lond B Biol Sci **2012,** 367 (1601), 2444-59.
40. Flower, D. R.; North, A. C.; Sansom, C. E., The lipocalin protein family: structural and sequence overview. Biochim Biophys Acta **2000,** 1482 (1-2), 9-24.
41. Skerra, A., Alternative binding proteins: anticalins - harnessing the structural plasticity of the lipocalin ligand pocket to engineer novel binding activities. FEBS J. **2008,** 275 (11), 2677-83.
42. Wan, J.; Peng, W.; Li, X.; Qian, T.; Song, K.; Zeng, J.; Deng, F.; Hao, S.; Feng, J.; Zhang, P.; Zhang, Y.; Zou, J.; Pan, S.; Zhu, J. J.; Jing, M.; Xu, M.; Li, Y., A genetically encoded GRAB sensor for measuring serotonin dynamics <em>in vivo</em&gt. bioRxiv **2020**, 2020.02.24.962282.

Chapter 4

A General Strategy to Red-shift Green Fluorescent Protein Based Biosensors

ABSTRACT

Compared to green fluorescent protein (GFP) based biosensors, red fluorescent protein (RFP) based biosensors are inherently advantageous because of reduced phototoxicity, decreased autofluorescence, and enhanced tissue penetration. However, there is a limited choice of RFP-based biosensors and development of each biosensor requires significant effort. Herein, we describe a general and convenient method which uses the genetically encoded amino acid, 3-aminotyrosine (aY), to convert GFPs and GFP-based biosensors into red.

4.1. INTRODUCTION

Fluorescent protein (FP) based biosensors are indispensable research tools.[4-6] Despite that RFP-based biosensors are increasingly reported, the emission of most existing FP-based biosensors falls in the green or yellow spectral region.[5] Their spectral overlap hinders and sometimes precludes multiplexing. Moreover, RFP-based biosensors are expected to reduce phototoxicity and autofluorescence and increase photon penetration and imaging depth. However, existing RFP-based biosensors often suffer from small dynamic range, mislocalization, and undesired photoconversion.[5] Thus, RFP-based biosensors are repeatedly outperformed by their green fluorescent counterparts in reality. In this context,

there is a pressing need to expand RFP-based biosensors for not only a broader range of analytical targets but also enhanced properties.

Although several green-to-red, photoconvertible FPs have been reported and widely used,[4] there is limited success to directly convert a typical GFP to an RFP. In one study, mutagenesis of GFP resulted in an "R10-3" mutant containing a mixture of green and red fluorescent chromophores.[10] A few other studies reported green-to-red photoconversion under anaerobic conditions,[11, 12] under extensive ultraviolet or blue

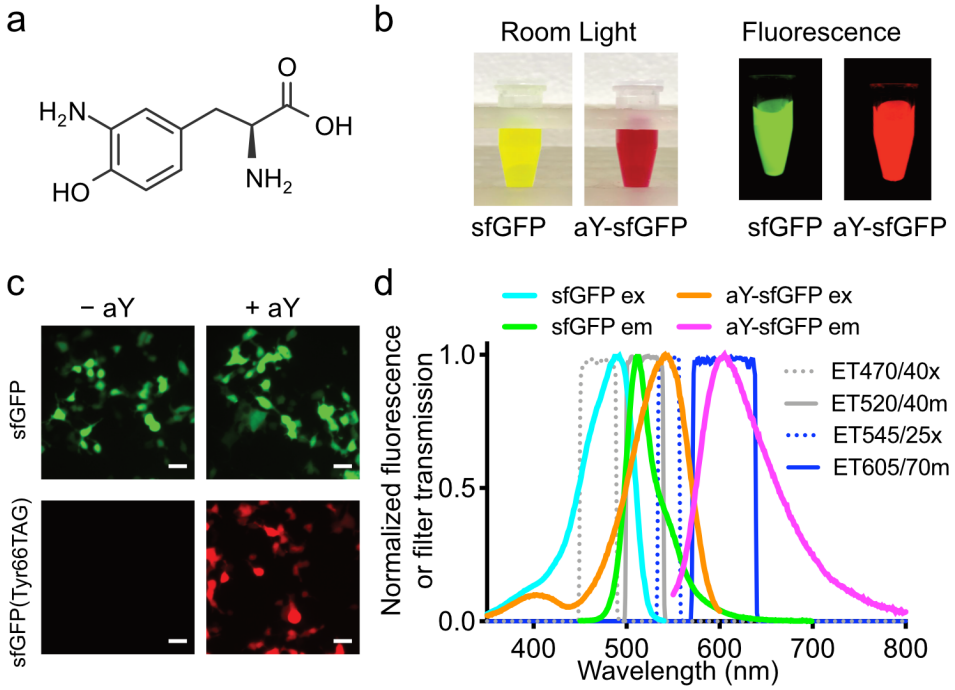

Figure 1. Green-to-red conversion of sfGFP by 3-aminotyrosine (aY). (a) Chemical structure of aY. (b) Imaging of sfGFP and aY-sfGFP proteins prepared from *E. coli*. (c) Microscopic imaging of HEK 293T cells co-transfected with pMAH-EcaYRS and pcDNA3-sfGFP or pcDNA3-sfGFP(Tyr66TAG), showing red fluorescence of aY-sfGFP in mammalian cells. Scale bar: 20 μm. (d) Fluorescence excitation and emission spectra of sfGFP (cyan and green) and aY-sfGFP (orange and magenta), suggesting that sfGFP and aY-sfGFP can be sequentially imaged with little crosstalk using appropriate filters. Transmission spectra for excitation and emission filters designated with Chroma Technology part numbers are also plotted (gray and blue). The experiments in panel b-d were repeated three times with similar results.

irradiation with high GFP expression levels,[13, 14] or in the presence of electron receptors.[15, 16] Nevertheless, these approaches usually lead to incomplete photoconversion; there is no reliable evidence that they can be generalized for green-to-red conversion of diverse GFP-like proteins and their derived biosensors.

We here present a general and convenient method, which uses genetic code expansion[17] to introduce a noncanonical amino acid (ncAA), aY (**Figure 1a**), to the chromophores of GFP-like proteins and biosensors for spontaneous and efficient green-to-red conversion.

4.2. EXPERIMENTAL SECTION

4.2.1. Materials, reagents, and general methods

Synthetic DNA oligonucleotides were purchased from Eurofins Genomics or Integrated DNA Technologies. The gene fragments for dLight1.2, SoNar, and iNap1 were chemically synthesized and purchased from Eurofins Genomics. CMV-B-GECO1 (Addgene plasmid # 32448) and pTorPE-G-GECO1 (Addgene plasmid # 32466) were gifts from Dr. Robert Campbell (University of Alberta). pCMV(MinDis).iGluSnFR (Addgene plasmid # 41732) and pAAV.hSynap.iGABASnFR (Addgene plasmid # 112159) were gifts from Dr. Loren Looger (Janelia). pm-iATPSnFR1.1 (Addgene plasmid # 102549) was a gift from Baljit Khakh (UCLA). FUGW-PercevalHR (Addgene plasmid # 49083) was a gift from Dr. Gary Yellen (Harvard). Wild-type MjTyrRS and EcTyrRS genes were gifts from Dr. Peter Schultz (Scripps). ZnGreen1 was previously reported by our lab.[18] FastDigest restriction endonucleases and Phusion High-Fidelity DNA Polymerase were

purchased from Fisher Scientific. ChoiceTaq DNA polymerase was purchased from Denville Scientific. The aY amino acid (a.k.a. H-3-amino-Tyr-OH·2HCl, Cat # 402789) was purchased from Bachem. 2-Deoxy-D-glucose (a.k.a. 2-DG, Cat # D0051) and tetramethylazodicarboxamide (a.k.a. diamide, Cat # A1458) were purchased from TCI America. Dopamine hydrochloride (Cat # A11136), ionomycin (Cat # J62448), and reduced β-nicotinamide adenine dinucleotide (a.k.a. NADH, Cat # J61638) were purchased from Alfa Aesar. N,N,N',N'-tetrakis(2-pyridinylmethyl)-1,2-ethanediamine (a.k.a. TPEN, Cat # 13340) and β-nicotinamide adenine dinucleotide phosphate reduced tetrasodium salt (a.k.a. NADPH, Cat # 9000743) were purchased from Cayman Chemical. Oxidized β-nicotinamide adenine dinucleotide (a.k.a. NAD^+, Cat # 481911) was purchased from Sigma-Aldrich. Monosodium L-glutamate (Cat # GL135) was purchased from Spectrum Chemical. Cell culture media were purchased from Corning. Other chemicals were purchased from Fisher Scientific. DNA sequencing was performed by Eurofins Genomics. Fluorescence images were acquired with a Leica DMi8 inverted microscope equipped with a Photometrics Prime 95B Scientific CMOS camera. A TRITC filter cube with a 545/25 nm bandpass excitation filter and a 605/70 nm bandpass emission filter was used to record red fluorescence from aY-modified FPs and biosensors. A FITC filter cube with a 470/40 nm bandpass excitation filter and a 520/40 nm bandpass emission filter was used to record green fluorescence from corresponding FPs and biosensors. A DAPI filter cube with a 377/50 nm bandpass excitation filter and a 447/60 nm bandpass emission filter was used to record blue fluorescence from B-GECO. Other general information is available from the "Life Sciences Reporting Summary".

4.2.2. Identification of aaRS for genetic encoding of aY in *E. coli*

Starting with the Protein Data Bank (PDB) entry, 2ZP1, which is an MjTyrRS mutant (MjTyrRS-H70A/D158T/I159S/D286Y) in complex with 3-iodotyrosine,[1] random mutagenesis at residue 70 was computationally introduced and the energy score function embedded in Autodock Vina 1.1.2[19] was used to assess the binding free energies of all complexes. By following our previously reported procedure,[7] a promising MjTyrRS mutant with H70S, D158T, I159S, and D286Y mutations (designated MjaYRS) was identified. These mutations were next experimentally introduced into the wild-type MjTyrRS by using sequential overlap PCR reactions and the resultant gene fragment was ligated into the previously reported pEvol plasmid.[20] Next, pEvol-MjaYRS and pBAD-sfGFP(Tyr66TAG) were used to co-transform bacterial DH10B cells. A colony picked from LB agar plates supplemented with ampicillin (100 μg/mL) and chloramphenicol (50 μg/mL) was used to inoculate 2 mL of LB at 37°C. Next day, the saturated culture was added to 100 mL of 2xYT. When OD_{600} reaches 0.6, L-arabinose (0.2%, w/v) and the aY amino acid (2 mM) were added to induce protein expression. After two additional days of shaking incubation at 250 rpm and 30°C, cells were pelleted and lysed with sonication. A control sample without aY was simultaneously prepared. Fluorescence of cleared cell lysates was analyzed. Strong red fluorescence was observed only for the positive group to which aY was added during protein expression. Ni-NTA agarose beads (Thermo Scientific) were added to remaining lysates and 6xHis-tagged proteins were purified by following the manufacturer's instructions. Proteins eluted from Ni-NTA beads were analyzed with SDS-PAGE and a band matching the size of full-length sfGFP was observed. Moreover, the eluted protein was desalted by precipitation with methanol and chloroform. The protein

pellet was dissolved in ddH_2O supplemented with 1% formic acid and injected into a Waters SQD2 electrospray ionization mass spectrometer (ESI-MS). The molar mass of the intact protein was determined by deconvolution of ESI peaks in MagTran1.03.[21]

4.2.3. Identification of aaRS for genetic encoding of aY in mammalian cells

On the basis of the PDB entry 1WQ3, which is an EcTyrRS mutant in complex with 3-iodotyrosine,[22] residues 37 and 195 of EcTyrRS were identified for mutagenesis. First, a D265R mutation was introduced to EcTyrRS using overlap PCR because the mutation was reported to increase anticodon recognition by the aaRS.[2] Furthermore, a gene fragment encoding the tyrosine editing domain of phenylalanyl-tRNA synthetase (PheRS)[3] was purchased from Eurofins Genomics and inserted to EcTyrRS via overlap PCRs, resulting in EcTyrRS* for reduced activity toward tyrosine. Using the aforementioned EcTyrRS* as the template, overlap PCRs were used to introduce mutations to residues 37 and 195 (numbered according to the wild-type EcTyrRS) and a total of 30 variants (residue 37: A, S, I, T, L, or V; and residue 195: A, N, S, T or C) in the pMAH vector[23, 24] were generated. These pMAH plasmids were used to co-transfect HEK 293T cells with pcDNA3-EGFP(Tyr39TAG).[23, 24] The aY amino acid (2 mM) was supplemented to cell culture media. After 2 days of incubation, cell lysates were prepared, and their fluorescence was determined by using a BioTek Synergy Mx plate reader. By comparing the lysate fluorescence of cells cultured in the presence and absence of the aY amino acid, an EcTyrRS* mutant with the highest incorporation specificity and efficiency was identified. This pMAH-aYRS plasmid was again used to co-transfect HEK 293T cells with pcDNA3-EGFP(Tyr39TAG), and the fluorescence difference of HEK 293T in the presence and

absence of aY was confirmed with fluorescence microscopy. Furthermore, the full-length EGFP was purified using Ni-NTA agarose beads, desalted, and analyzed with ESI-MS as aforementioned.

4.2.4. Detection of aY-sfGFP fragmentation using SDS-PAGE

Following a previously reported method,[25] purified aY-sfGFP in 1x SDS gel-loading buffer was either unboiled or boiled at 100°C for 10 min, before being loaded to a 15% SDS-polyacrylamide gel (PAGE). Similarly treated mCherry and sfGFP were used for comparison. After electrophoresis, the gel was stained with Coomassie blue R-250.

4.2.5. Construction of expression vectors for FPs and biosensors

Briefly, overlap PCRs with mutagenic primers were used to replace the codon of the chromophore tyrosine with the amber codon (TAG). The assembled gene fragments were inserted into either pBAD/His B between Xho I and Hind III restriction sites for *E. coli* expression, or pcDNA3 between Hind III and Xho I restriction sites for mammalian expression. To express the amber variants of iGABASnFR and iGluSnFR on mammalian cell surface, the gene fragments were inserted to pDisplay between Bgl II and Sal I restriction sites. In addition, two residues of SoNar, iNap1, and PercevalHR corresponding to residues 68 and 69 of wild-type GFP were mutated to V and M, respectively, because these mutations were found to promote the formation of the red chromophore. For comparison purposes, pBAD/His B, pcDNA3, and/or pDisplay plasmids harboring the genes of wild-type fluorescent proteins and biosensors were created in parallel. To express biosensors such as SoNar in mitochondria, overlap PCRs were used to add an N-terminal

mitochondrial localization sequence (MLSLRQSIRFFKPATRTLCSSRYLL) and the resultant gene fragments were inserted into pcDNA3 between Hind III and Xho I.

4.2.6. Spectral characterization of biosensors

Wild-type and aY-modified G-GECO1, ZnGreen1, iGluSnFR, SoNar, iNap1, PercevalHR, and iATPSnFR1.1 in pBad/HisB were used to express proteins in *E. coli* DH10B and purified as N-terminal 6xHis-tagged protein as previously described.[26] Furthermore, the proteins were passed through a HiPrep Sephacryl S-200 HR gel filtration column (GE Healthcare) by using elution buffers (10 mM MOPS, pH 7.2, and 100 mM KCl for G-GECO1 and its aY-modified variant; 150 mM HEPES, pH 7.4, 100 mM NaCl and 0.5 mM TCEP for ZnGreen1 and its aY-modified variant; and 50 mM Tris HCl, pH 7.4, and 100 mM NaCl for other biosensors). Sensor proteins were further diluted with their corresponding elution buffers to the final concentrations of ~ 100 nM and then mixed with other desired components for measurement of fluorescence excitation and emission spectra on a monochromator based BioTek Synergy Mx plate reader. Spectral characterization of dLight1.2 and iGABASnFR were directly performed with HEK 293T cells. After transfection and sensor expression, ~ 1 million cells were dissociated and thoroughly rinsed with Dulbecco's Phosphate-Buffered Saline (DPBS). Next, cells were resuspended in 300 µL DPBS and aliquoted into two individual wells of a 96-well microplate with or without supplementing dopamine or GABA. Fluorescence excitation and emission spectra were next determined on a BioTek Synergy Mx plate reader.

4.2.7. Culture and transfection of mammalian cell lines

HEK 293T cells and HeLa cells (purchased from ATCC and tested for mycoplasma by PCR) were cultured in Dulbecco's Modified Eagle Medium (DMEM) containing 1 g/L glucose and 10% fetal bovine serum (FBS) in a humidified 37°C incubator with 5% CO_2. The day before transfection, $2.5x10^5$ cells were used to seed each 35-mm cell culture dish. At the time of transfection, 10 μg of PEI (linear polyethylenimine, 25 kDa, from Polysciences) and a total of 4 μg of corresponding plasmid DNA (pcDNA3 biosensor plasmid: pMAH-aYRS = 1:1, w/w) were mixed in 250 μL of Opti-MEM I Reduced Serum Medium. Complexation lasted for 15 min at room temperature before addition of the mixture to cells with FBS-containing DMEM pre-removed. After additional 3 h of cell incubation at 37°C, the Opti-MEM mixture was replaced with DMEM supplemented with 10% FBS and 2 mM aY. Cell culture media were replaced every 36 h. Fluorescence imaging was typically performed between 48 and 72 h post transfection. Mouse insulinoma MIN6 cells (a gift from Dr. Shuibing Chen at Weill Cornell Medical College; tested for mycoplasma by PCR) were maintained in GlutaMAX-supplemented DMEM containing 4.5 g/L glucose, 10 mM HEPES (pH 7.4), 50 μM 2-mercaptoethanol, and 10% FBS at 37°C. The transfection procedure was similar to that of HEK 293T and HeLa, except for that $6x10^5$ cells were used to seed each 35-mm cell culture dish, and that commercial Lipofectamine 2000 (Thermo Fisher) was used to replace PEI.

4.2.8. Culture and transfection of primary mouse hippocampal neurons

E18 mouse hippocampus was purchased from BrainBits. Dissociated neurons were cultured with 2 mL of NbActiv4 medium (BrainBits) in 35 mm glass-bottom dishes pre-

coated with collagen I (Cat # A1048301, Thermo Fisher). Every two days, half of the cell culture medium was replaced with fresh NbActiv4. Neurons were transfected on day 7 by following BrainBits's protocol. Briefly, 1 mL of culture media were taken from each 35 mm dish and combined with another 1 mL of fresh NbActiv4. The conditioned medium was incubated at 37°C and 5% CO_2. A total of 4 μg of plasmid DNA (G-GECO1 : aY-iGluSnFR : pMAH-aYRS = 1:2:2, w/w/w) and 8 μL of Lipofectamine 2000 (Thermo Fisher) were mixed in 100 μL of BrainBits Transfection Medium and the resultant mixture was incubated at room temperature for 15 min. Next, 1 mL of warm, conditioned NbActiv4 medium was used to replace the medium in each 35 mm dish and the transfection mixture was then added. After 3 h of incubation in at 37°C in a 5% CO_2 incubator, the medium was exchanged again to the conditioned medium without transfection mixture but supplemented with 2 mM aY. Half of the aY-containing medium was exchanged every two days. Fluorescence imaging was performed between 48 and 72 h post transfection.

4.2.9. Time-lapse imaging of aY-GECO1, aY-PercevalHR, aY-iATPSnFR, and aY-SoNar in HeLa

For aY-GECO1, HeLa cells in DPBS (Ca^{2+}- and Mg^{2+}-free) were imaged every 1 s for a duration of 13 min. Stimuli, such as 5 μM histamine, 1 mM $CaCl_2$ with 10 μM ionomycin, and 2 mM EGTA with 5 μM ionomycin, were added sequentially. For aY-PercevalHR or aY-iATPSnFR, HeLa cells in Ca^{2+}- and Mg^{2+}-containing Hank's Balanced Salt Solution (HBSS) were imaged every 30 s and 10 mM 2-DG was added to induce cellular ATP concentration changes. For aY-SoNar, HeLa cells in Ca^{2+}- and Mg^{2+}-

containing DPBS were imaged every 20 s and 1 mM sodium pyruvate was added as the stimulus.

4.2.10. Time-lapse imaging of aY-ZnGreen1 and aY-iNap1 in HEK 293T

For aY-GECO1, HEK 293T cells in modified Krebs-HEPES-bicarbonate buffer (KHB) containing 140 mM NaCl, 3.6 mM KCl, 0.5 mM NaH_2PO_4, 0.5 mM $MgSO_4$, 1.5 mM $CaCl_2$, 10 mM HEPES, 2 mM $NaHCO_3$, and 3 mM glucose were imaged every 4 s. $ZnCl_2$ stock was prepared in slightly acidic pure water. TPEN and pyrithione stock solutions were prepared in DMSO. KHB was then used to dilute Zn^{2+}, pyrithione, and TPEN to desired concentrations right before each use. For aY-iNap1, HEK 293T cells in DPBS were imaged every min. 1 mM diamide was used to stimulate NADPH changes.

4.2.11. Imaging of metabolic dynamics of MIN6 cells

Cells were transiently transfected as aforementioned with desired combinations of plasmids and imaged between 48 and 72 h post transfection. Before imaging, cells were washed thoroughly and left in HBSS (1 g/L glucose). Images were acquired every min. 20 mM D-glucose was added to stimulate MIN6 cells.

4.2.12. Data and statistical analysis

Fiji was used to analyze microscopic images. Microsoft Excel, OriginPro, GraphPad Prism, and Affinity Designer were used to analyze data and prepare figures for publication. Paired two-tailed t-tests were used to determine all P values. No sample was excluded from data analysis, and no blinding or randomization was employed. Unless

otherwise indicated, data are shown as mean and s.d., and error bars in figures represent s.d.

4.3. RESULTS AND DISCUSSION

By expressing orthogonal tRNA and aminoacyl-tRNA synthetase (aaRS) in live cells, diverse ncAAs can be site-specifically introduced into proteins in response to nonsense or four-base codons.[17] To genetically introduce aY into proteins in *E. coli*, we first examined a reported *Methanococcus jannaschii* tyrosyl-tRNA synthetase (MjTyrRS) mutant but observed high cross-reactivity with Tyr.[27] Next, we examined another MjTyrRS mutant, which was initially engineered for the genetic encoding of 3-iodotyrosine.[1] We computationally docked aY to the active site of this enzyme and introduced randomization.[7] We identified a promising MjTyrRS mutant (designated MjaYRS) with Ser at residue 70, which mutation may promote H-bonding with the side-chain amino group of aY (**Figure 2a**). Next, we expressed a superfolder GFP (sfGFP)[28] mutant with an amber codon introduced to its residue 66 in the presence of MjaYRS and the corresponding amber suppression tRNA. We observed strong fluorescence and obtained the full-length protein in good yield (~ 6.7 mg per liter of culture) when aY was supplemented (**Figure 2b, c**). We further characterized the resultant protein with electrospray ionization mass spectrometry (ESI-MS) and confirmed the incorporation of aY to sfGFP (**Figure 2d**).

To genetically encode aY in mammalian cells, we took *E. coli* tyrosyl-tRNA synthetase (EcTyrRS) as our starting point (**Figure 3a**). We first introduced a D265R mutation to increase anticodon recognition by the aaRS,[2] and further inserted a tyrosine

editing domain into EcTyrRS to reduce its reactivity with tyrosine.[3] We next created 30 EcTyrRS variants with mutations at residues 37 and 195 within the amino acid-binding pocket. Screening of these mutants for amber suppression of pcDNA3-EGFP(Tyr39TAG) identified an aaRS variant (a.k.a. EcaYRS) with Y37L and Q195S mutations (**Figure 3b**). In the presence of aY, EcaYRS, and the corresponding tRNA, full-length EGFP was generated, as confirmed by both fluorescence microscopy and ESI-MS (**Figure 3c, d**).

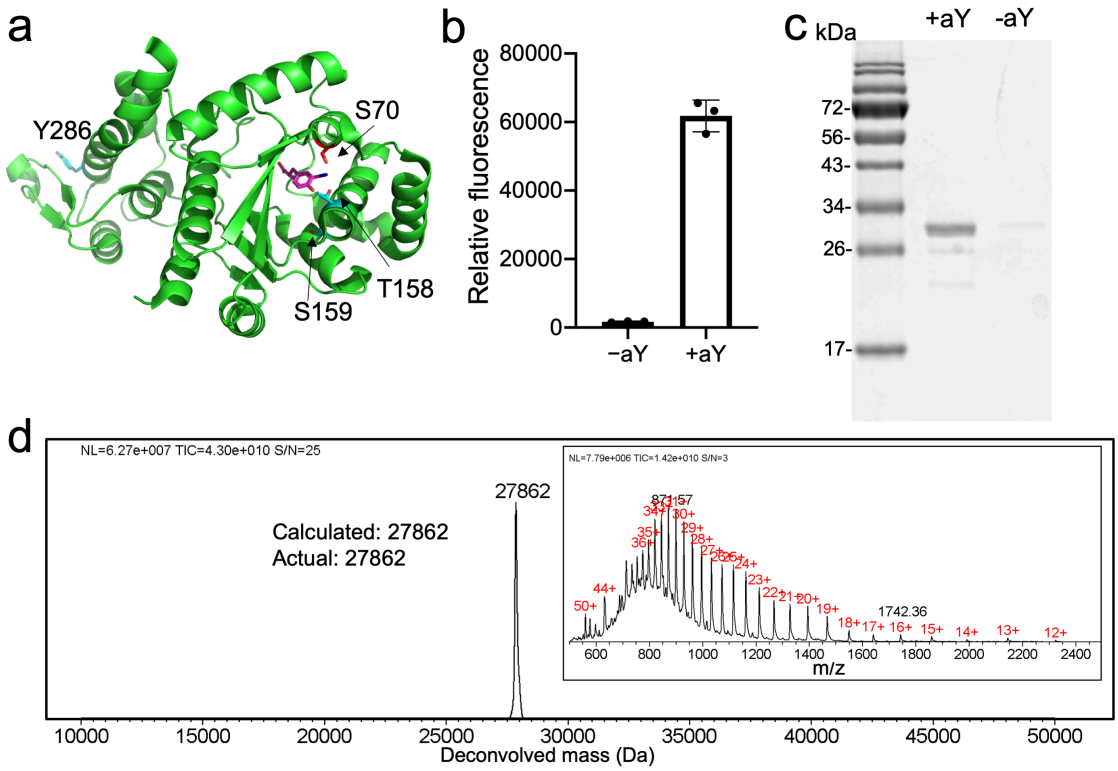

Figure 2. Genetic encoding of 3-aminotyrosine (aY) in *E. coli*. (**a**) Modeled structure of a *Methanococcus jannaschii* tyrosyl-tRNA synthetase mutant (*Mj*TyrRS-H70S/D158T/I159S/D286Y; a.k.a. *Mj*aYRS) in complex with aY. The template used for modeling is an *Mj*TyrRS mutant in complex with 3-iodotyrosine (Protein Data Bank 2ZP1).[1] This model was created with AutoDock Vina by following our previously reported procedure.[7] (**b**) pBAD-sfGFP(Tyr66TAG) expression with pEvol-*Mj*aYRS, as indicated by relative red fluorescence of cell lysates in the presence or absence of aY. (**c**) SDS-PAGE analysis of Ni-NTA-purified proteins from *E. coli* in the presence or absence of aY. (**d**) ESI mass spectrometry analysis of intact protein purified from *E. coli* in the presence of aY and its respective amino acid sequence. The observed mass matches the calculated mass (considering N-terminal Met cleavage, sfGFP chromophore maturation, and additional transformation to a mCherry-like chromophore). The data collectively support that aY can be site-specifically introduced into proteins in *E. coli* by using our engineered aminoacyl-tRNA synthetase, *Mj*aYRS.

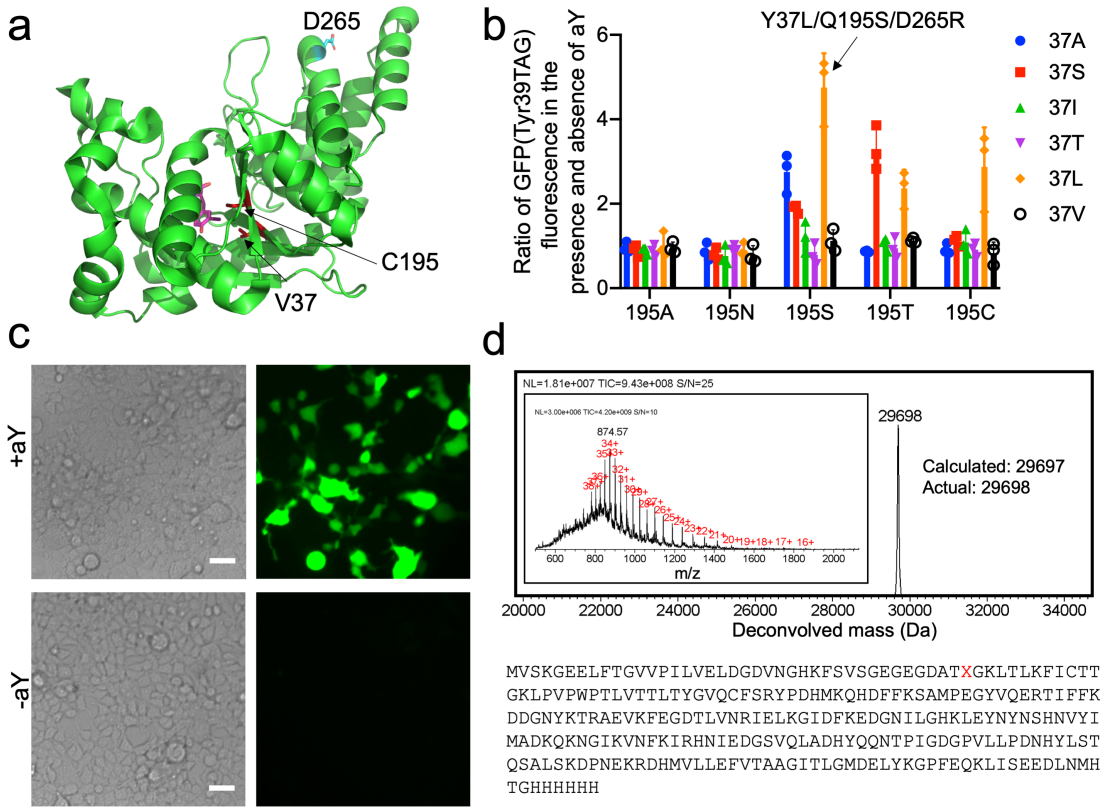

Figure 3. Genetic encoding of 3-aminotyrosine (aY) in mammalian cells. (**a**) Structure of an *E. coli* tyrosyl-tRNA synthetase mutant (*Ec*TyrRS-Y37V/Q195C) in complex with 3-iodotyrosine (Protein Data Bank 1WQ3). (**b**) Screening of *Ec*TyrRS mutants with mutations at residues 37 and 195 for the suppression of the amber TAG stop codon in pcDNA3-EGFP(Tyr39TAG) in HEK 293T cells. A D265R was introduced into *Ec*TyrRS because it increases the binding of the aminoacyl-tRNA synthetase to the anticodon.[2] An additional tyrosine editing domain was inserted as previously described,[3] resulting in *Ec*TyrRS* for reduced activity toward tyrosine. A mutant (*Ec*TyrRS*-Y37L/Q195S/D265R) in the pMAH plasmid was selected and named pMAH-*Ec*aYRS because of its high efficiency and fidelity for mammalian encoding of aY. (**c**) Microscopic imaging of HEK 293T cells transfected with pcDNA3-EGFP(Tyr39TAG) and pMAH-*Ec*aYRS in the presence (top row) or absence (bottom row) of aY (scale bar: 40 μm). (**d**) ESI mass spectrometry analysis of intact EGFP purified from HEK 293T cells in the presence of aY and its respective amino acid sequence. The difference between the observed and calculated masses is within the expected error range of the instrument. The data collectively support that aY can be site-specifically introduced into proteins in mammalian cells by using our engineered aminoacyl-tRNA synthetase.

The color of aY-sfGFP (sfGFP[28] with aY introduced to its chromophore-forming residue 66) from *E. coli* was red under both room light and green excitation, and it showed nearly no residual green fluorescence (**Figure 1b**). To test whether this phenomenon is species-specific, we expressed aY-sfGFP in human embryonic kidneys (HEK) 293T cells and then observed spontaneous, red fluorescence (**Figure 1c**). The excitation and emission maxima of aY-sfGFP were red-shifted from those of sfGFP by 56 and 95 nm, respectively, suggesting that it may be possible to pair aY-sfGFP with GFPs or GFP-based biosensors for sequential, dual-color imaging using common fluorescence microscope setups (**Figure 1d**).

The chromophore of GFP is spontaneously formed through cyclization, dehydration, and oxidation of an internal tripeptide motif, while the chromophores of common RFPs differ from GFP in that additional, self-catalyzed oxidation occurs to expand chromophore conjugation via a hydrolyzable N-acylimine substitution.[25] Because aY is sensitive to oxidation, we hypothesize that aY-sfGFP spontaneously forms an RFP-like chromophore through additional oxidation (**Figure 4a**). Although the detailed mechanism remains to be explored, the formation of a hydrolyzable chromophore is supported by backbone cleavage of aY-sfGFP under denaturing conditions (**Figure 4b**). Furthermore, the absorbance of aY-sfGFP decreases at ~ 540 nm with concurrent increase at ~ 390 nm as pH drops from neutral to acidic, (**Figure 4c**), suggesting the existence of an anionic chromophore in aY-sfGFP at neutral conditions.

Next, we introduced aY to the chromophores of several FPs containing Tyr-derived chromophores, including teal fluorescent mTFP1,[29] yellow fluorescent Citrine,[30] a circularly permuted sfGFP (cpsGFP),[31] and a circularly permuted yellow FP (cpYFP).[23]

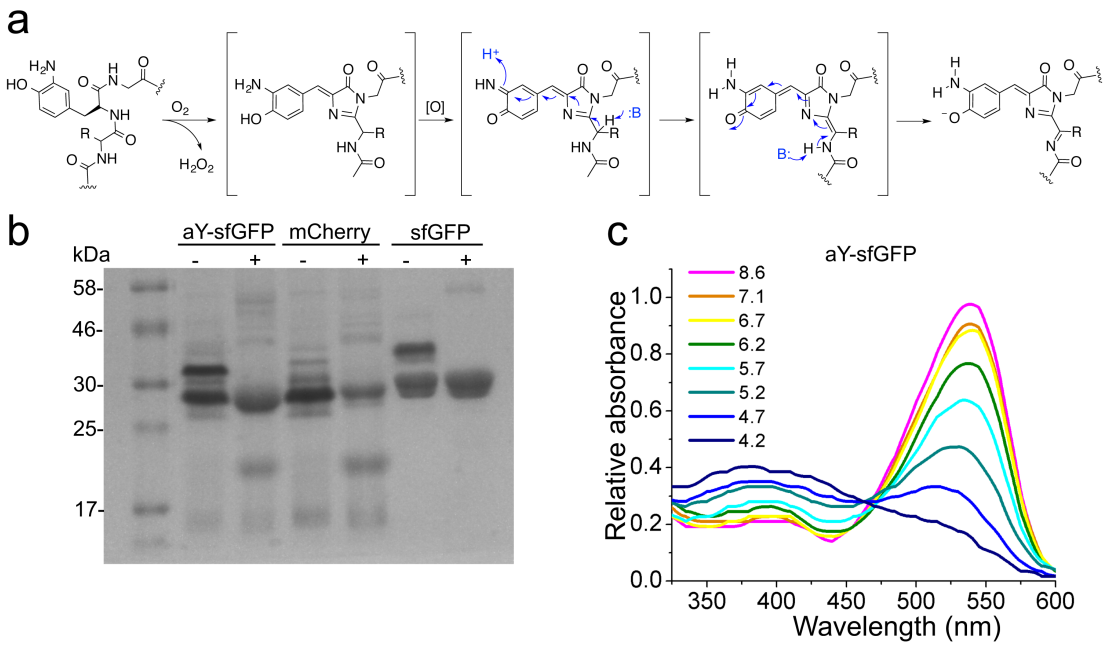

Figure 4. Proposed chromophore transformations in GFP upon aY-modification of the chromophore. (a) Proposed scheme for the conversion of the precursor polypeptide to the mature, red fluorescent chromophore. The formation of an mCherry-like chromophore is supported by polypeptide cleavage patterns in panel b. The negative charge of the chromophore is supported by pH titration in panel c. (b) Monitoring of polypeptide cleavage by SDS-PAGE. aY-sfGFP, mCherry, and sfGFP either unboiled (-) or boiled for 10 min (+) in 1x SDS gel-loading buffer were loaded to polyacrylamide gel. The boiled aY-sfGFP shows a polypeptide cleavage pattern similar to that of mCherry, suggesting the formation of a hydrolyzable C=N bond in aY-sfGFP. An additional band above 30 kDa was observed for both unboiled aY-sfGFP and sfGFP, likely due to additional folding states of these proteins. (c) Absorbance of aY-sfGFP in response to pH changes. At low pH, the chromophore of aY-sfGFP is further protonated, as indicated by absorbance increase at ~ 400 nm.

Red-shifted excitation and emission were observed for all of them (**Figure. 5** & **Table 1**), indicating that the aY-induced green-to-red conversion is neither protein-specific nor topology-specific.

After confirming that aY can red-shift various Tyr-derived chromophores, we used aY to modify a number of biosensors based on circularly permuted green, teal, or yellow FPs, including G-GECO1 (a Ca^{2+} sensor),[32] ZnGreen1 (a Zn^{2+} sensor),[18] iGluSnFR (a

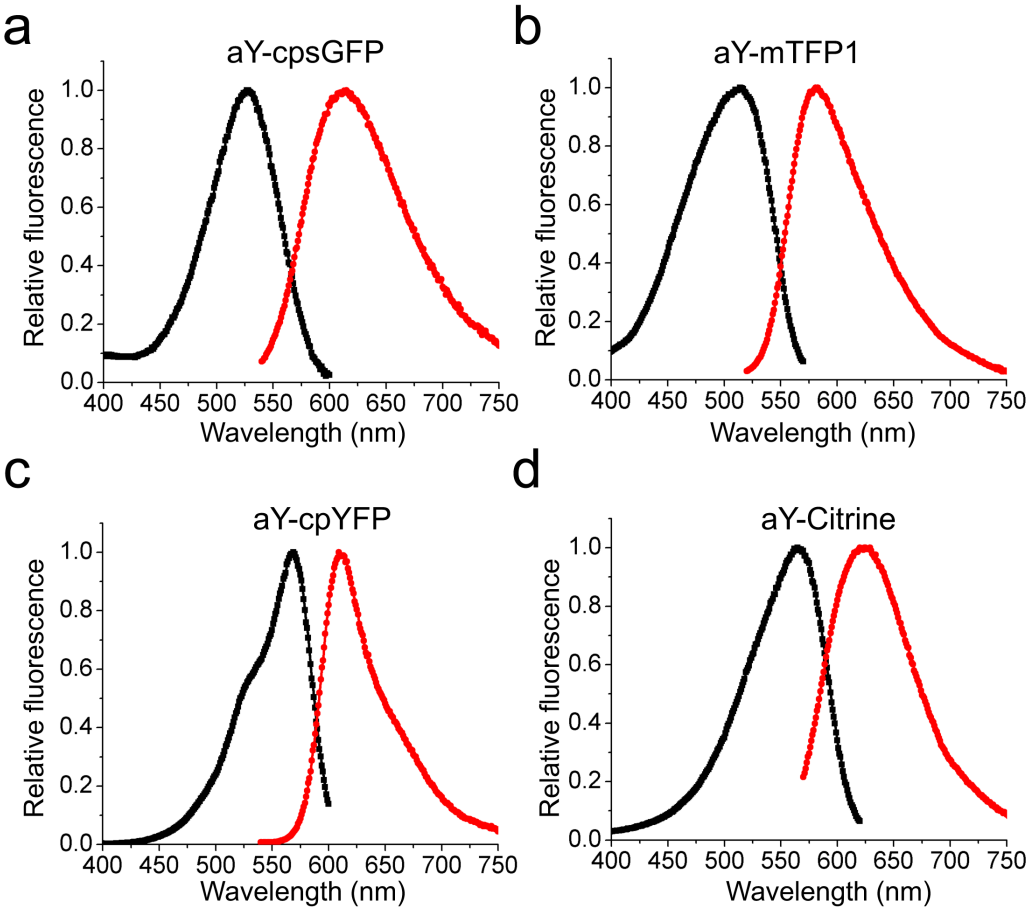

Figure 5. Fluorescence excitation and emission of various aY-modified fluorescence proteins. Fluorescence excitation (black) and emission (red) profiles of aY-modified cpsGFP (a), mTFP1 (b), cpYFP (c), and Citrine (d).

glutamate sensor),[33] iGABASnFR (a GABA sensor),[34] dLight1.2 (a dopamine sensor),[35] SoNar (a NAD^+/NADH sensor),[36] iNAP1 (a NADPH sensor),[37] PercevalHR (an ATP sensor),[38] and iATPSnFR1.1 (another ATP sensor).[39] We observed red-shifted fluorescence for all test biosensors (**Table 2**). Moreover, the converted biosensors largely

retained the dynamic range and responsiveness of their green fluorescent predecessors, as shown in our validation experiments with purified proteins, cultured mammalian cell lines, and/or primary neurons (**Figures. 6-13**).

Table 1. Excitation and emission maxima of selected fluorescent proteins.

	Chromophore-forming residues	Normal proteins		Proteins with aY-derived chromophores	
		Excitation (nm)	Emission (nm)	Excitation (nm)	Emission (nm)
sfGFP	TYG	485	510	541	605
cpsGFP [a]	TYG	488	510	527	615
mTFP1	AYG	462	492	514	581
cpYFP [b]	GYG	503	515	569	609
Citrine	GYG	516	529	565	624

[a] Circularly permuted sfGFP variant previously used to derive the hydrogen sulfide sensor, hsGFP.[31]
[b] Circularly permuted EYFP variant previously used to derive the hydrogen sulfide sensor, cpGFP-pAzF.[23]

Table 2. Properties of genetically encoded biosensors and their aY-modified variants.

Biosensor	Analytical target	Excitation (nm)	Emission (nm)	Dynamic Range ($\Delta F/F_{min}$)[a]	References
G-GECO1	Ca^{2+}	497	512	1,983%	Zhao et al.[32]
aY-G-GECO1	Ca^{2+}	528	594	1,566%	This work
ZnGreen1	Zn^{2+}	474	500	2,531%	Chen et al.[18]
aY-ZnGreen1	Zn^{2+}	520	585	915%	This work
iGluSnFR	glutamate	488	510	257%	Marvin et al.[33]
aY-iGluSnFR	glutamate	528	600	270%	This work
iGABASnFR	GABA	502	513	143%	Marvin et al.[34]
aY-GABASnFR	GABA	541	602	92%	This work
dLight1.2	dopamine	496	513	194%	Patriarchi et al.[35]
aY-dLight1.2	dopamine	545	603	117%	This work
SoNar	NAD^+/NADH	497	512	257%	Zhao et al.[36]
aY-SoNar	NAD^+/NADH	544	604	426%	This work
iNap1	NADPH	497	513	82%	Tao et al.[37]
aY-iNap1	NADPH	545	604	614%	This work
PercevalHR	ATP	498	513	185%	Tantama et al.[38]
aY-PercevalHR	ATP	545	604	120%	This work
iATPSnFR1.1	ATP	493	513	106%	Lobas et al.[39]
aY-iATPSnFR1.1	ATP	541	608	75%	This work

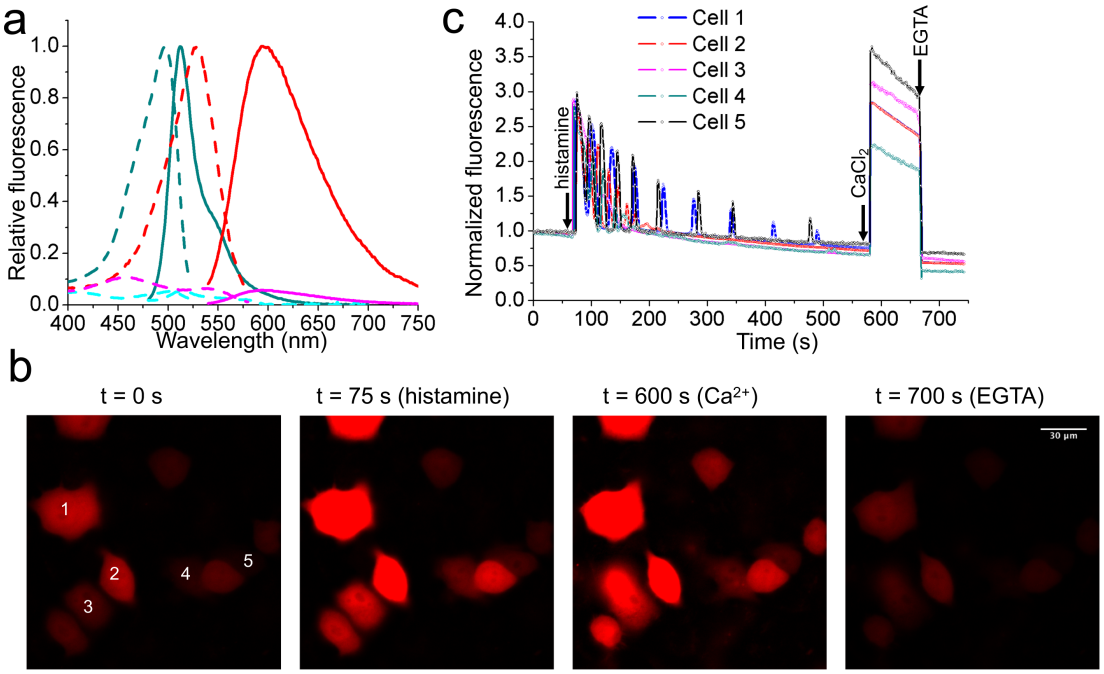

Figure 6. Characterization of aY-modified G-GECO1 (Ca^{2+} sensor). (a) Fluorescence excitation (dash line) and emission (solid line) profiles for G-GECO1 after addition of 1 mM EGTA (cyan) or 100 µM Ca^{2+} (dark cyan), and aY-G-GECO1 after addition of 1 mM EGTA (magenta) or 100 µM Ca^{2+} (red). (b) Representative images of HeLa cells expressing aY-G-GECO1 in response to sequential addition of 5 µM histamine, 1 mM $CaCl_2$ with 10 µM ionomycin, and 2 mM EGTA with 5 µM ionomycin. Scale bar: 30 µm. (c) Quantitative traces for randomly selected five cells in panel b. Intensities are normalized to the values at t = 0 s. The time points for addition of chemicals are shown as arrows. Ca^{2+} oscillations in response to histamine were observed as expected. These experiments were repeated three times with similar results using independent biological samples.

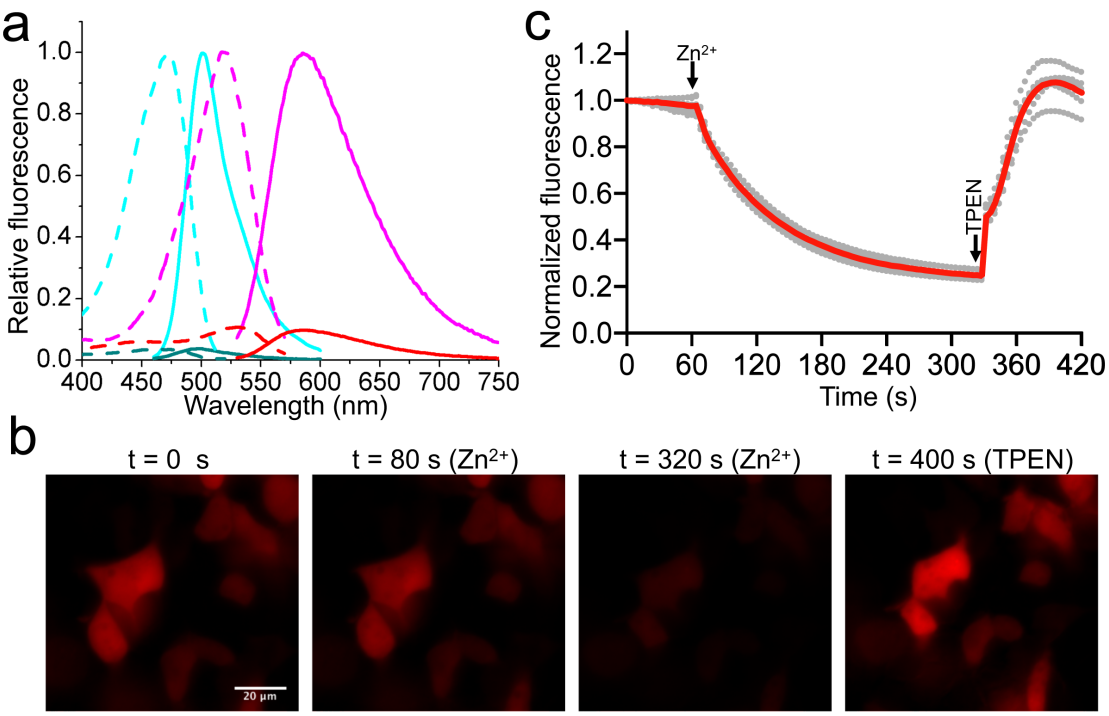

Figure 7. Characterization of aY-modified ZnGreen1 (Zn^{2+} sensor). (a) Fluorescence excitation (dash line) and emission (solid line) profiles for ZnGreen1 after addition of 1 mM EDTA (cyan) or 100 μM Zn^{2+} (dark cyan), and aY- ZnGreen1 after addition of 1 mM EDTA (magenta) or 100 μM Zn^{2+} (red). (b) Representative images of HEK 293T cells expressing aY-ZnGreen1 in response to sequential addition of 50 μM $ZnCl_2$ with 5 μM pyrithione, and 200 μM TPEN. Scale bar: 20 μm. (c) Quantitative traces for randomly selected six single cells (gray dots) and their average (red line). Intensities are normalized to the values at t = 0 s. The time points for addition of chemicals are shown as arrows. These experiments were repeated three times with similar results using independent biological samples.

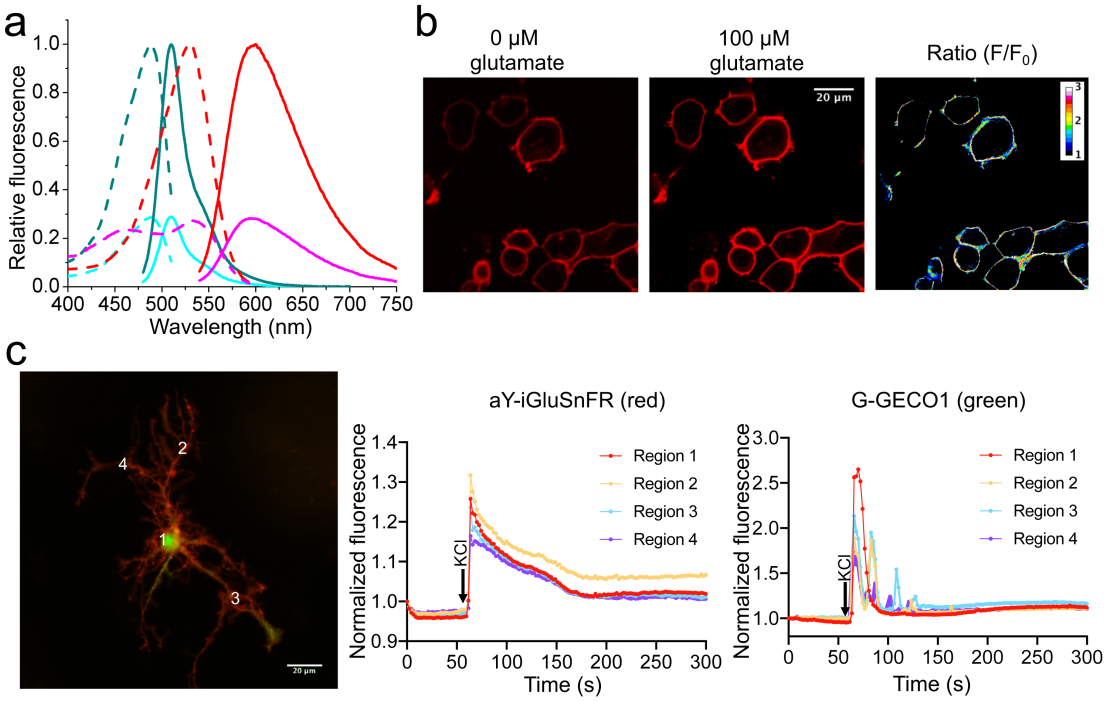

Figure 8. Characterization of aY-modified iGluSnFR (glutamate sensor). (**a**) Fluorescence excitation (dash line) and emission (solid line) profiles for iGluSnFR before (cyan) and after (dark cyan) addition of 100 μM L-glutamate, and aY-iGluSnFR before (magenta) and after (red) addition of 100 μM L-glutamate. (**b**) Representative images of HEK 293T cells expressing cell-surface-localized aY-iGluSnFR in response to addition of 100 μM L-glutamate. (**c**) Cultured mouse hippocampal neurons in response to 90 mM KCl (excitatory Tyrode's saline buffer).[8] Neurons were co-transfected to express cell-surface-localized aY-iGluSnFR (red fluorescence) and a Ca^{2+} indicator, G-GECO1 (green fluorescence). Quantitative traces for four different regions are presented. Intensities are normalized to the values at $t = 0$ s. These experiments were repeated three times with similar results using independent biological samples. Scale bar: 20 μm.

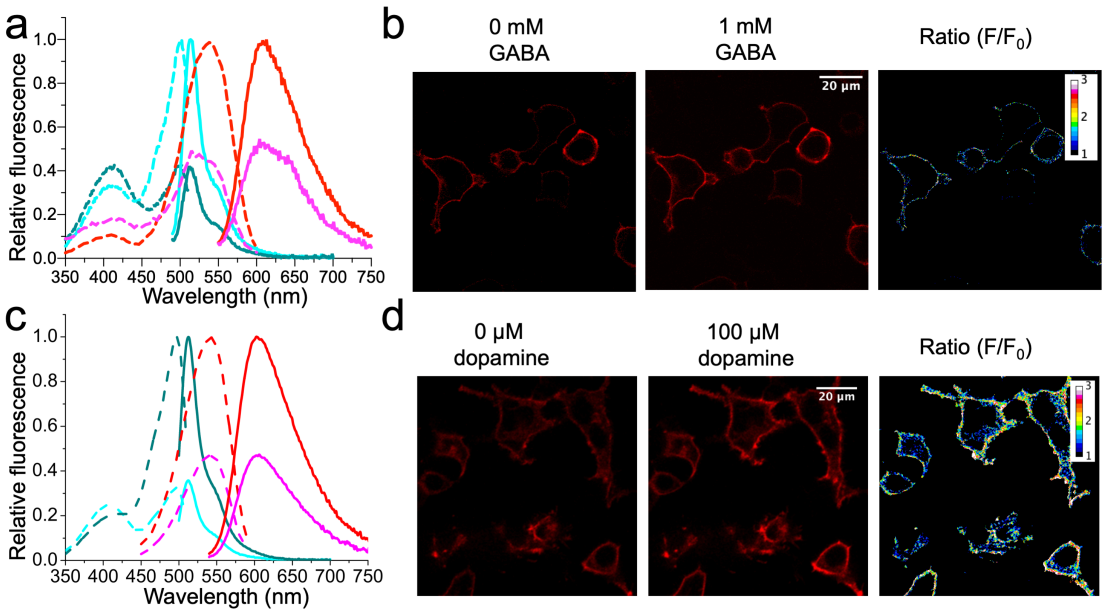

Figure 9. Characterization of aY-modified iGABASnFR (a,b) and dLight1.2 (c,d) as biosensors for GABA and dopamine, respectively. (a,c) Fluorescence excitation (dash line) and emission (solid line) profiles for iGABASnFR or dLight1.2 before (cyan) and after (dark cyan) addition of 1 mM GABA or 100 µM dopamine, and aY-iGABASnFR or aY-dLight1.2 before (magenta) and after (red) addition of 1 mM GABA or 100 µM dopamine. (b,d) Representative images of HEK 293T cells expressing surface-localized aY-iGABASnFR (b) or aY-dLight1.2 (d) in response to GABA or dopamine. These experiments were repeated three times with similar results using independent biological samples. Scale bar: 20 µm.

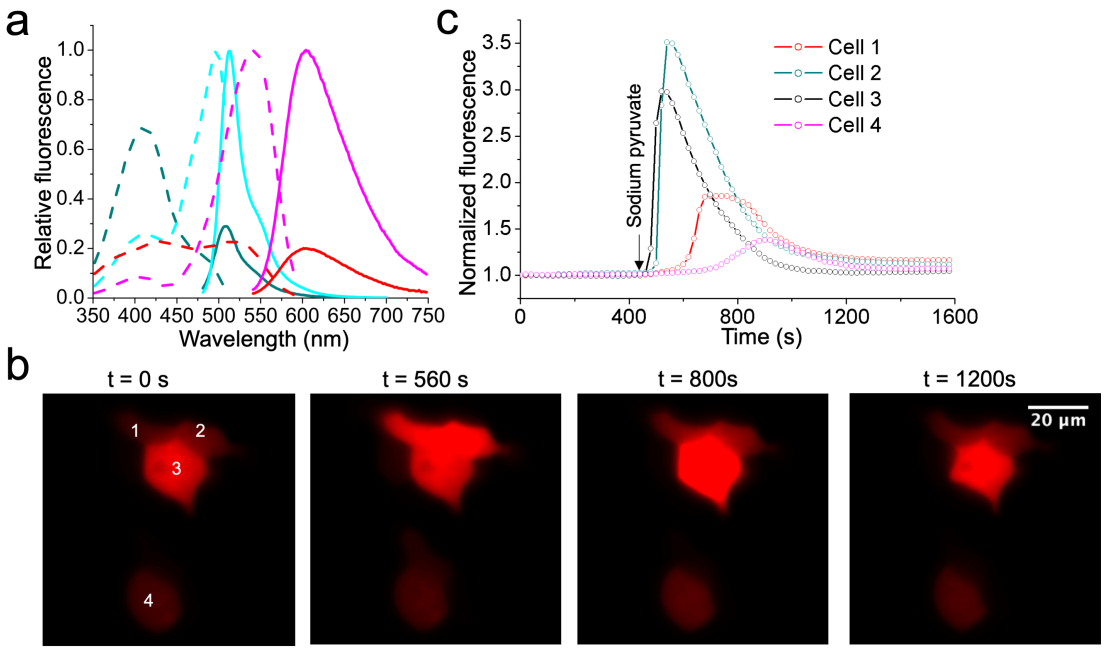

Figure 10. Characterization of aY-modified SoNar (NAD^+/NADH sensor). (a) Fluorescence excitation (dash line) and emission (solid line) profiles for SoNar after addition of 20 µM NAD^+ (cyan) or NADH (dark cyan), and aY-SoNar after addition of 20 µM NAD^+ (magenta) or NADH (red). (b) Representative images of HEK 293T cells expressing aY-SoNar in response to addition of 1 mM pyruvate. Scale bar: 20 µm. (c) Quantitative traces for randomly selected four single cells in panel b. Intensities are normalized to the values at t = 0 s. The time points for addition of chemicals are shown as arrows. These experiments were repeated three times with similar results using independent biological samples.

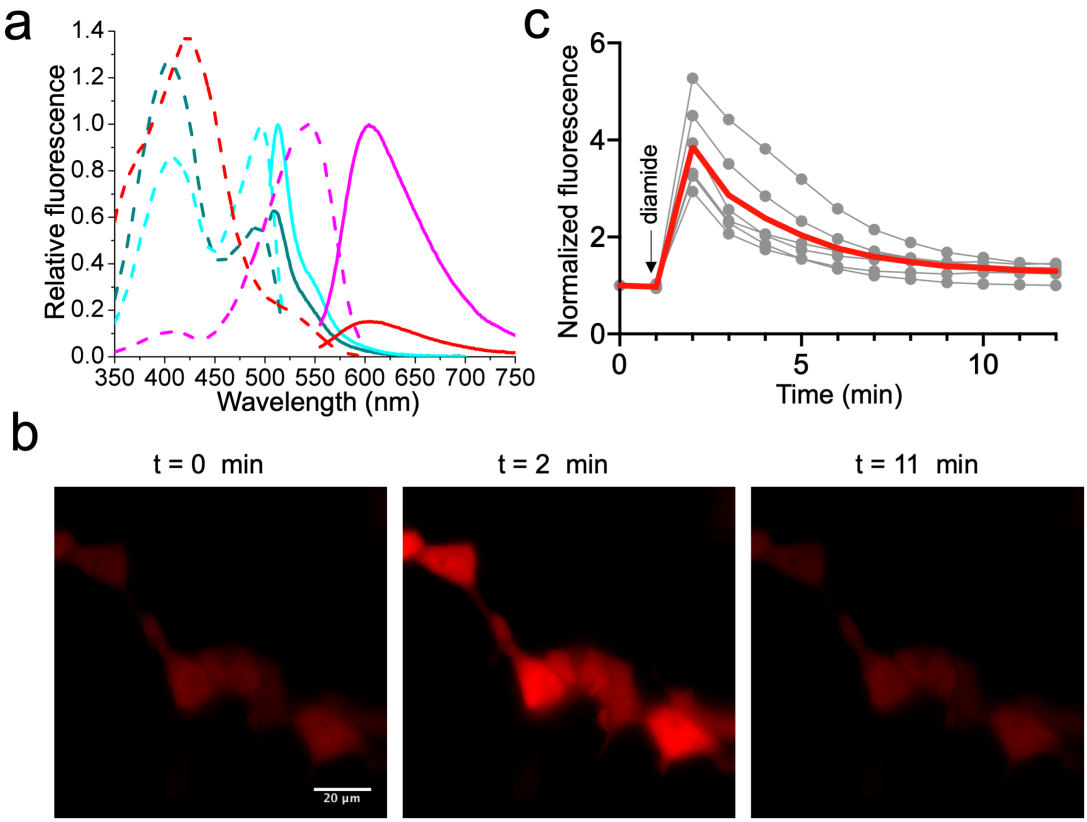

Figure 11. Characterization of aY-modified iNap1 (NADPH sensor). (a) Fluorescence excitation (dash line) and emission (solid line) profiles for iNap1 before (cyan) and after (dark cyan) addition of 100 µM NADPH, and aY-iNap1 before (magenta) and after (red) addition of 100 µM NADPH. (b) Representative images of HEK 293T cells expressing aY- iNap1 in response to addition of 1 mM diamide. Scale bar: 20 µm. (c) Quantitative traces for randomly selected five single cells (gray dots) and their average (red line). Intensities are normalized to the values at t = 0 s. The time points for addition of chemicals are shown as arrows. These experiments were repeated three times with similar results using independent biological samples.

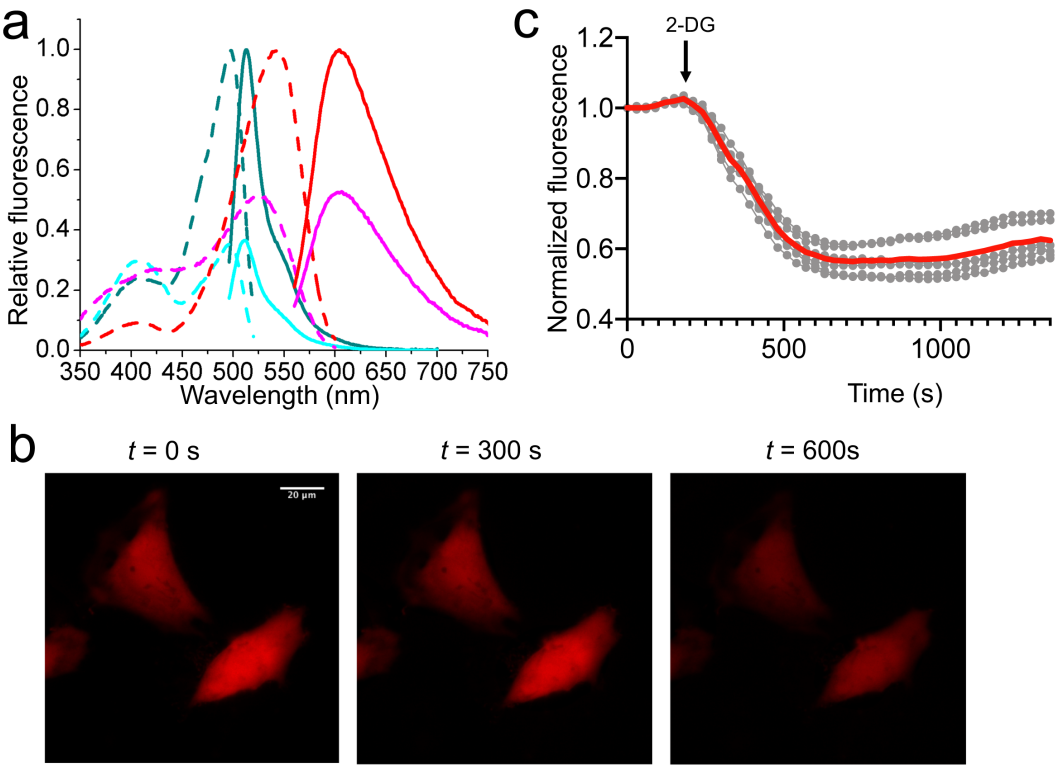

Figure 12. Characterization of aY-modified PercevalHR (ATP sensor). (a) Fluorescence excitation (dash line) and emission (solid line) profiles for PercevalHR before (cyan) and after (dark cyan) addition of 1 mM ATP, and aY-PercevalHR before (magenta) and after (red) addition of 1 mM ATP. (b) Representative images of HeLa cells expressing aY- PercevalHR in response to 10 mM 2-deoxy-D-glucose (2-DG). Scale bar: 20 µm. (c) Quantitative traces for randomly selected five single cells (gray dots) and their average (red line). Intensities are normalized to the values at t = 0 s. The time points for addition of chemicals are shown as arrows. These experiments were repeated three times with similar results using independent biological samples.

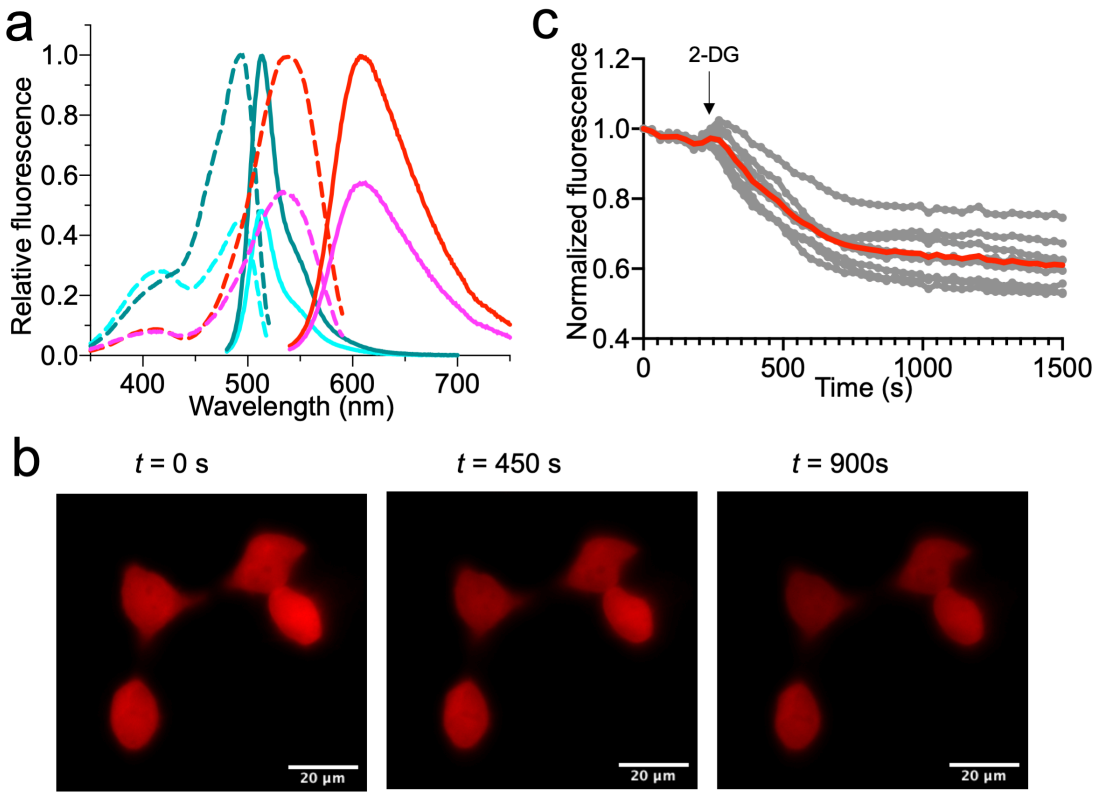

Figure 13. Characterization of aY-modified iATPSnFR1.1 (ATP sensor). (a) Fluorescence excitation (dash line) and emission (solid line) profiles for iATPSnFR1.1 before (cyan) and after (dark cyan) addition of 1 mM ATP, and aY-iATPSnFR1.1 before (magenta) and after (red) addition of 1 mM ATP. (b) Representative images of HeLa cells intracellular expressing aY-iATPSnFR1.1 in response to 10 mM 2-deoxy-D-glucose (2-DG). Scale bar: 20 µm. (c) Quantitative traces for randomly selected eight single cells (gray dots) and their average (red line). Intensities are normalized to the values at t = 0 s. The time points for addition of chemicals are shown as arrows. These experiments were repeated three times with similar results using independent biological samples.

To demonstrate the use of aY-modified biosensors for multiplexed imaging, we monitored glucose-induced metabolic dynamics in mouse MIN6 pancreatic β cells.

Pancreatic β cells are responsible for glucose sensing and secretion of insulin, a key hormone regulating sugar metabolism. Upon entering β cells, glucose breaks down to

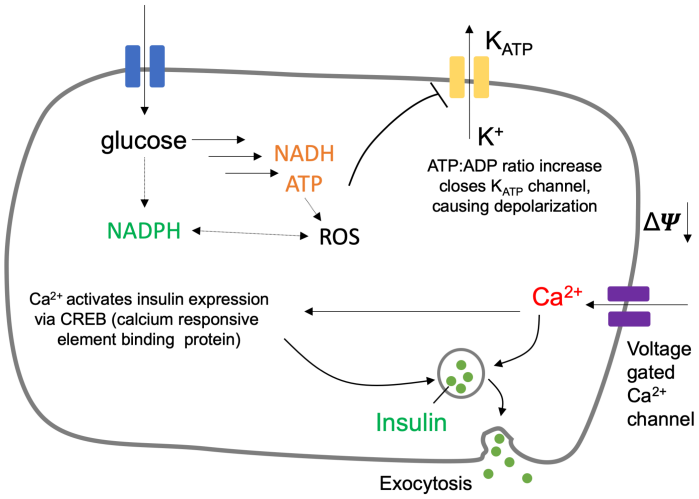

Figure 14. Simplified metabolic model of glucose-stimulated insulin release from pancreatic β-cells. NADH, ATP, NADPH, K^+, and Ca^{2+} are known coupling factors for glucose-stimulated insulin secretion.[9] In this simplified model, glucose is transported into β-cells through facilitated diffusion, is phosphorylated, and converted to substances such as pyruvate, NADH, NADPH, and ATP. ATP closes ATP-sensitive potassium (K_{ATP}) channels, initiating plasma membrane depolarization and increasing intracellular Ca^{2+} via voltage-dependent calcium channels (VDCCs). This glucose-induced cytosolic Ca^{2+} increase triggers the fusion of insulin granules with cell membrane and exocytosis of insulin, C-peptide, and a few other substances.

generate an array of metabolic signals that regulate insulin synthesis and secretion (**Figure 14**). Although previous studies have demonstrated important roles of NADH, NADPH, and ATP in glucose sensing in β cells, the spatiotemporal dynamics of these metabolic signals has not been adequately studied.[40] We first co-expressed B-GECO (a blue fluorescent Ca^{2+} biosensor),[32] iATPSnFR1.1 (a green fluorescent ATP biosensor),[39] and aY-SoNar (a red

fluorescent NAD^+/NADH biosensor) in MIN6 (**Figure 15a**). In response to high glucose (20 mM), we observed an immediate rise of B-GECO or iATPSnFR1.1 fluorescence, reflecting an acute increase of intracellular Ca^{2+} and ATP (**Figure 15b**). The fluorescence of B-GECO or iATPSnFR1.1 was sustained at high levels with some expected oscillations for an extended period. Surprisingly, the fluorescence of aY-SoNar displayed a small, immediate increase followed by a drop, suggesting an initial small increase and then a decrease of cellular NAD+/NADH. Despite the heterogeneity of individual MIN6 cells, this trend for aY-SoNar was well reproduced when we examined more cells (**Figure 15c**). Similarly, we observed a phenomenal rise followed by a reduction of the fluorescence of aY-iNap1 (a red fluorescent NADPH biosensor) post glucose stimulation (**Figure 15d**). Since the concentration of NADPH is inversely correlated with the fluorescence of aY-iNap1 (**Figure 11**), we interpret that high glucose transiently decreased cellular NADPH and then maintained high NADPH levels in MIN6 cells. Because NAD^+/NADH and NADPH are compartmentalized and mitochondria play a central role in metabolism, we next fused aY-SoNar or aY-iNap1 to a mitochondrial localization sequence to for mitochondrial expression in MIN6. In response to high glucose, mitochondrial NAD^+/NADH displayed an immediate decrease, whereas mitochondrial NADPH still decreased transiently before the rise (**Figures 15e, f**). We further co-expressed SoNar and mitochondrial aY-SoNar to follow compartmentalized changes in the same MIN6 cells (**Figures 15g, h**). Upon glucose stimulation, there were obvious and consistent delays in cytosolic NAD^+/NADH decrease compared to mitochondrial NAD^+/NADH and the average delay time was determined to be 3.3 min by analyzing 17 individual cells (**Figures 15h, i**). Normally, a net gain on NADH is expected to occur upstream to the gain on ATP

in glucose metabolism.[40] Thus, our observed delay of NAD^+/NADH reduction, particularly in the cytosol, in relation to ATP increase corroborates recent hypotheses and findings that alternative mechanisms may play roles in glucose sensing in β-cells.[40, 41] Furthermore, glucose-induced NADPH in β-cells was suggested to protect β-cells from oxidative stress,[42] but our study uncovered an unexpected, transient phase lasting a few minutes post glucose stimulation, during which NADPH decreases in both cytosol and mitochondria of MIN6 cells. On the basis of these results, we postulate that lactate dehydrogenase (LDH) based ATP production from NADH, metabolite shuttles between the cytosol and mitochondria, and/or transient oxidative signaling may contribute to acute responses of β-cells to glucose.[40-42] Research is ongoing in our laboratory to further investigate these mechanism in β-cells and primary islets.

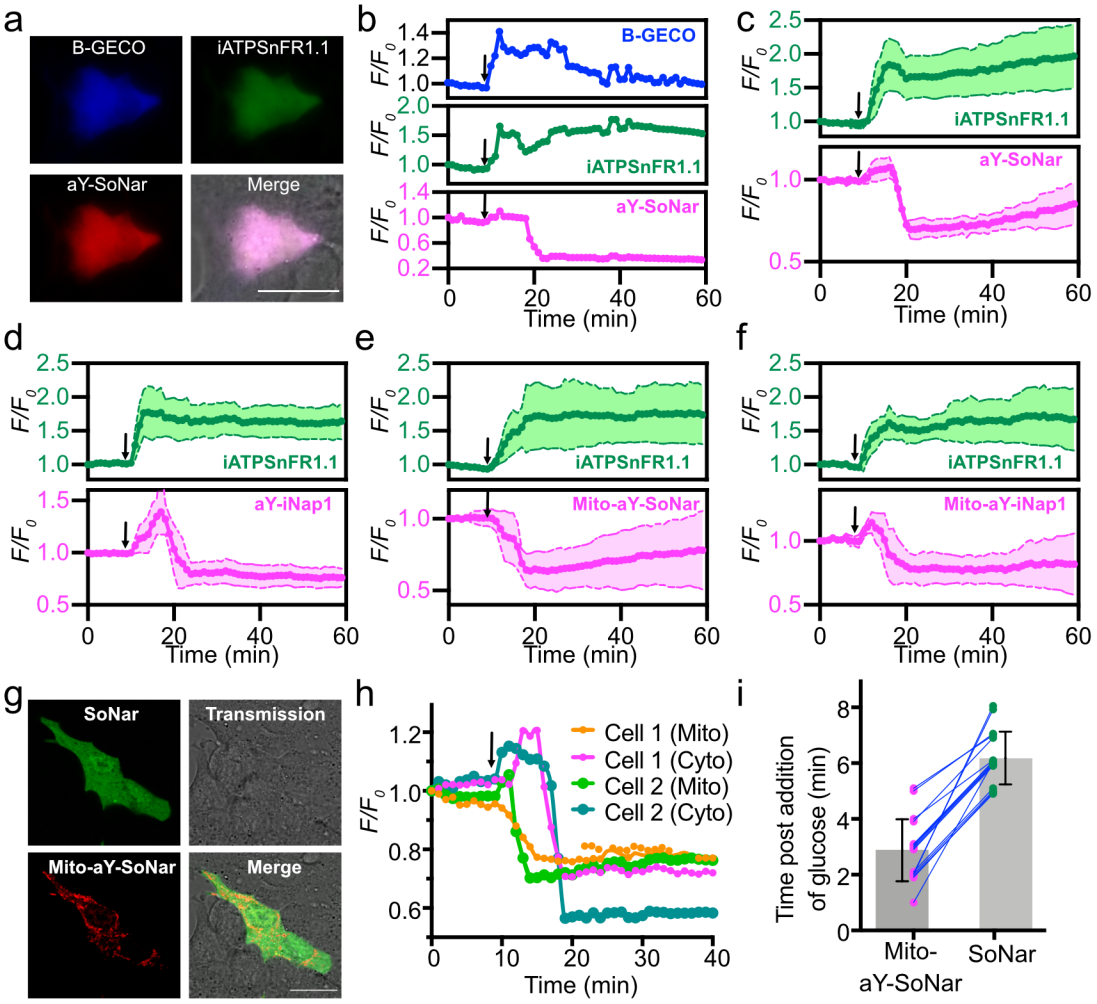

Figure 15. Fluorescence imaging of glucose-induced metabolic dynamics in pancreatic MIN6 β-cells. (**a**) Representative tri-color images of MIN6 co-expressing B-GECO, iATPSnFR1.1, aY-SoNar. (**b**) Representative traces (F/F_0) for B-GECO, iATPSnFR1.1, and aY-SoNar. These experiments were repeated three times with similar results. (**c**) Quantitative traces (F/F_0) for co-expressed iATPSnFR1.1 and aY-SoNar (n=8). (**d**) Quantitative traces (F/F_0) for co-expressed iATPSnFR1.1 and aY-iNap1 (n=7). (**e**) Quantitative traces (F/F_0) for co-expressed iATPSnFR1.1 and mitochondrial aY-SoNar (n=8). (**f**) Quantitative traces (F/F_0) for co-expressed iATPSnFR1.1 and mitochondrial aY-iNap1 (n=12). (**g**) Representative dual-color images of MIN6 co-expressing SoNar and mitochondrial aY-SoNar. (**h**) Representative traces (F/F_0) for cytosolic SoNar and mitochondrial aY-SoNar. (**i**) Comparison of response time (corresponding to the middle point of the fluorescence decrease phase) in individual MIN6 cells after glucose addition (n=17; Mito-aY-SoNar: 2.88±1.11 min; SoNar: 6.18±0.95 min; paired two-tailed *t*-test, $P<0.001$). The time points for addition of 20 mM D-glucose are shown as arrows in panels **b-f** and **h**. Data are presented as mean and s.d. of indicated replicates.

4.4. CONCLUSIONS

In summary, we genetically encoded aY in both *E. coli* and mammalian cells, and developed a general method based on the introduction of aY to the chromophores of GFP-like proteins and biosensors for spontaneous and efficient green-to-red conversion. This approach does not require photoconversion or other special experimental conditions and is compatible with a variety of FPs and FP-based biosensors in *E. coli*, mammalian cell lines, and primary cells. Little optimization is needed as dynamic range and responsiveness are largely retained in the converted biosensors. Therefore, this method can be used to quickly expand the repository of RFP-based biosensors.

REFERENCES

1. Sakamoto, K.; Murayama, K.; Oki, K.; Iraha, F.; Kato-Murayama, M.; Takahashi, M.; Ohtake, K.; Kobayashi, T.; Kuramitsu, S.; Shirouzu, M.; Yokoyama, S., Genetic encoding of 3-iodo-L-tyrosine in Escherichia coli for single-wavelength anomalous dispersion phasing in protein crystallography. Structure **2009,** 17 (3), 335-44.
2. Takimoto, J. K.; Adams, K. L.; Xiang, Z.; Wang, L., Improving orthogonal tRNA-synthetase recognition for efficient unnatural amino acid incorporation and application in mammalian cells. Mol. BioSyst. **2009,** 5 (9), 931-4.
3. Oki, K.; Sakamoto, K.; Kobayashi, T.; Sasaki, H. M.; Yokoyama, S., Transplantation of a tyrosine editing domain into a tyrosyl-tRNA synthetase variant enhances its specificity for a tyrosine analog. Proc. Natl. Acad. Sci. U. S. A. **2008,** 105 (36), 13298-303.
4. Rodriguez, E. A.; Campbell, R. E.; Lin, J. Y.; Lin, M. Z.; Miyawaki, A.; Palmer, A. E.; Shu, X.; Zhang, J.; Tsien, R. Y., The Growing and Glowing Toolbox of Fluorescent and Photoactive Proteins. Trends Biochem Sci **2017,** 42 (2), 111-129.
5. Greenwald, E. C.; Mehta, S.; Zhang, J., Genetically Encoded Fluorescent Biosensors Illuminate the Spatiotemporal Regulation of Signaling Networks. Chem Rev **2018,** 118 (24), 11707-11794.

6. Greenwald, E. C.; Mehta, S.; Zhang, J., Genetically Encoded Fluorescent Biosensors Illuminate the Spatiotemporal Regulation of Signaling Networks. Chemical Reviews **2018,** 118 (24), 11707-11794.
7. Ren, W.; Truong, T. M.; Ai, H. W., Study of the Binding Energies between Unnatural Amino Acids and Engineered Orthogonal Tyrosyl-tRNA Synthetases. Sci. Rep. **2015,** 5, 12632.
8. Okumoto, S.; Looger, L. L.; Micheva, K. D.; Reimer, R. J.; Smith, S. J.; Frommer, W. B., Detection of glutamate release from neurons by genetically encoded surface-displayed FRET nanosensors. Proceedings of the National Academy of Sciences of the United States of America **2005,** 102 (24), 8740.
9. MacDonald, P. E.; Joseph, J. W.; Rorsman, P., Glucose-sensing mechanisms in pancreatic beta-cells. Philos Trans R Soc Lond B Biol Sci **2005,** 360 (1464), 2211-25.
10. Mishin, A. S.; Subach, F. V.; Yampolsky, I. V.; King, W.; Lukyanov, K. A.; Verkhusha, V. V., The first mutant of the Aequorea victoria green fluorescent protein that forms a red chromophore. Biochemistry **2008,** 47 (16), 4666-73.
11. Sawin, K. E.; Nurse, P., Photoactivation of green fluorescent protein. Curr. Biol. **1997,** 7 (10), R606-7.
12. Elowitz, M. B.; Surette, M. G.; Wolf, P. E.; Stock, J.; Leibler, S., Photoactivation turns green fluorescent protein red. Curr. Biol. **1997,** 7 (10), 809-12.
13. Sattarzadeh, A.; Saberianfar, R.; Zipfel, W. R.; Menassa, R.; Hanson, M. R., Green to red photoconversion of GFP for protein tracking in vivo. Scientific reports **2015,** 5, 11771.
14. Ai, M.; Mills, H.; Kanai, M.; Lai, J.; Deng, J.; Schreiter, E.; Looger, L.; Neubert, T.; Suh, G., Green-to-Red Photoconversion of GCaMP. PLoS One **2015,** 10 (9), e0138127.
15. Bogdanov, A. M.; Mishin, A. S.; Yampolsky, I. V.; Belousov, V. V.; Chudakov, D. M.; Subach, F. V.; Verkhusha, V. V.; Lukyanov, S.; Lukyanov, K. A., Green fluorescent proteins are light-induced electron donors. Nat. Chem. Biol. **2009,** 5 (7), 459-61.
16. Saha, R.; Verma, P. K.; Rakshit, S.; Saha, S.; Mayor, S.; Pal, S. K., Light driven ultrafast electron transfer in oxidative redding of Green Fluorescent Proteins. Scientific reports **2013,** 3, 1580.
17. Liu, C. C.; Schultz, P. G., Adding new chemistries to the genetic code. Annu Rev Biochem **2010,** 79, 413-44.
18. Chen, Z.; Ai, H. W., Single Fluorescent Protein-Based Indicators for Zinc Ion (Zn(2+)). Anal. Chem. **2016,** 88 (18), 9029-36.
19. Trott, O.; Olson, A. J., AutoDock Vina: improving the speed and accuracy of docking with a new scoring function, efficient optimization, and multithreading. J. Comput. Chem. **2010,** 31 (2), 455-61.
20. Young, T. S.; Ahmad, I.; Yin, J. A.; Schultz, P. G., An enhanced system for unnatural amino acid mutagenesis in E. coli. J. Mol. Biol. **2010,** 395 (2), 361-74.
21. Zhang, Z.; Marshall, A. G., A universal algorithm for fast and automated charge state deconvolution of electrospray mass-to-charge ratio spectra. J Am Soc Mass Spectrom **1998,** 9 (3), 225-33.
22. Kobayashi, T.; Sakamoto, K.; Takimura, T.; Sekine, R.; Kelly, V. P.; Kamata, K.; Nishimura, S.; Yokoyama, S., Structural basis of nonnatural amino acid recognition

by an engineered aminoacyl-tRNA synthetase for genetic code expansion. Proc. Natl. Acad. Sci. U. S. A. **2005,** 102 (5), 1366-71.
23. Chen, S.; Chen, Z. J.; Ren, W.; Ai, H. W., Reaction-based genetically encoded fluorescent hydrogen sulfide sensors. J. Am. Chem. Soc. **2012,** 134 (23), 9589-92.
24. Chatterjee, A.; Xiao, H.; Bollong, M.; Ai, H. W.; Schultz, P. G., Efficient viral delivery system for unnatural amino acid mutagenesis in mammalian cells. Proc. Natl. Acad. Sci. U. S. A. **2013,** 110 (29), 11803-8.
25. Gross, L. A.; Baird, G. S.; Hoffman, R. C.; Baldridge, K. K.; Tsien, R. Y., The structure of the chromophore within DsRed, a red fluorescent protein from coral. Proc. Natl. Acad. Sci. U.S.A. **2000,** 97 (22), 11990-5.
26. Chen, Z. J.; Ren, W.; Wright, Q. E.; Ai, H. W., Genetically encoded fluorescent probe for the selective detection of peroxynitrite. J. Am. Chem. Soc. **2013,** 135 (40), 14940-3.
27. Seyedsayamdost, M. R.; Xie, J.; Chan, C. T.; Schultz, P. G.; Stubbe, J., Site-specific insertion of 3-aminotyrosine into subunit alpha2 of E. coli ribonucleotide reductase: direct evidence for involvement of Y730 and Y731 in radical propagation. J. Am. Chem. Soc. **2007,** 129 (48), 15060-71.
28. Pedelacq, J. D.; Cabantous, S.; Tran, T.; Terwilliger, T. C.; Waldo, G. S., Engineering and characterization of a superfolder green fluorescent protein. Nat. Biotechnol. **2006,** 24 (1), 79-88.
29. Ai, H. W.; Henderson, J. N.; Remington, S. J.; Campbell, R. E., Directed evolution of a monomeric, bright and photostable version of Clavularia cyan fluorescent protein: structural characterization and applications in fluorescence imaging. Biochem. J. **2006,** 400 (3), 531-40.
30. Griesbeck, O.; Baird, G. S.; Campbell, R. E.; Zacharias, D. A.; Tsien, R. Y., Reducing the environmental sensitivity of yellow fluorescent protein. Mechanism and applications. J. Biol. Chem. **2001,** 276 (31), 29188-94.
31. Chen, Z. J.; Ai, H. W., A Highly Responsive and Selective Fluorescent Probe for Imaging Physiological Hydrogen Sulfide. Biochemistry **2014,** 53 (37), 5966-5974.
32. Zhao, Y.; Araki, S.; Wu, J.; Teramoto, T.; Chang, Y. F.; Nakano, M.; Abdelfattah, A. S.; Fujiwara, M.; Ishihara, T.; Nagai, T.; Campbell, R. E., An expanded palette of genetically encoded Ca(2)(+) indicators. Science **2011,** 333 (6051), 1888-91.
33. Marvin, J. S.; Borghuis, B. G.; Tian, L.; Cichon, J.; Harnett, M. T.; Akerboom, J.; Gordus, A.; Renninger, S. L.; Chen, T. W.; Bargmann, C. I.; Orger, M. B.; Schreiter, E. R.; Demb, J. B.; Gan, W. B.; Hires, S. A.; Looger, L. L., An optimized fluorescent probe for visualizing glutamate neurotransmission. Nat. Methods **2013,** 10 (2), 162-70.
34. Marvin, J. S.; Shimoda, Y.; Magloire, V.; Leite, M.; Kawashima, T.; Jensen, T. P.; Kolb, I.; Knott, E. L.; Novak, O.; Podgorski, K.; Leidenheimer, N. J.; Rusakov, D. A.; Ahrens, M. B.; Kullmann, D. M.; Looger, L. L., A genetically encoded fluorescent sensor for in vivo imaging of GABA. Nat. Methods **2019,** 16 (8), 763-770.
35. Patriarchi, T.; Cho, J. R.; Merten, K.; Howe, M. W.; Marley, A.; Xiong, W. H.; Folk, R. W.; Broussard, G. J.; Liang, R.; Jang, M. J.; Zhong, H.; Dombeck, D.; von Zastrow, M.; Nimmerjahn, A.; Gradinaru, V.; Williams, J. T.; Tian, L., Ultrafast neuronal imaging of dopamine dynamics with designed genetically encoded sensors. Science **2018,** 360 (6396).

36. Zhao, Y.; Hu, Q.; Cheng, F.; Su, N.; Wang, A.; Zou, Y.; Hu, H.; Chen, X.; Zhou, H. M.; Huang, X.; Yang, K.; Zhu, Q.; Wang, X.; Yi, J.; Zhu, L.; Qian, X.; Chen, L.; Tang, Y.; Loscalzo, J.; Yang, Y., SoNar, a Highly Responsive NAD+/NADH Sensor, Allows High-Throughput Metabolic Screening of Anti-tumor Agents. Cell Metab. **2015,** 21 (5), 777-89.
37. Tao, R.; Zhao, Y.; Chu, H.; Wang, A.; Zhu, J.; Chen, X.; Zou, Y.; Shi, M.; Liu, R.; Su, N.; Du, J.; Zhou, H. M.; Zhu, L.; Qian, X.; Liu, H.; Loscalzo, J.; Yang, Y., Genetically encoded fluorescent sensors reveal dynamic regulation of NADPH metabolism. Nat. Methods **2017,** 14 (7), 720-728.
38. Tantama, M.; Martinez-Francois, J. R.; Mongeon, R.; Yellen, G., Imaging energy status in live cells with a fluorescent biosensor of the intracellular ATP-to-ADP ratio. Nat. Commun. **2013,** 4, 2550.
39. Lobas, M. A.; Tao, R.; Nagai, J.; Kronschlager, M. T.; Borden, P. M.; Marvin, J. S.; Looger, L. L.; Khakh, B. S., A genetically encoded single-wavelength sensor for imaging cytosolic and cell surface ATP. Nat. Commun. **2019,** 10 (1), 711.
40. Fridlyand, L. E.; Philipson, L. H., Glucose sensing in the pancreatic beta cell: a computational systems analysis. Theor Biol Med Model **2010,** 7, 15.
41. Korosak, D.; Slak Rupnik, M., Collective Sensing of beta-Cells Generates the Metabolic Code. Front. Physiol. **2018,** 9, 31.
42. Gray, J. P.; Alavian, K. N.; Jonas, E. A.; Heart, E. A., NAD kinase regulates the size of the NADPH pool and insulin secretion in pancreatic beta-cells. Am J Physiol Endocrinol Metab **2012,** 303 (2), E191-9.

Chapter 5

Perspectives

Genetically encoded fluorescent biosensors have become powerful imaging tools that illuminate the spatiotemporal regulation of signaling networks. Both improvements in sensitivity and kinetics during the development of fluorescent biosensors have fulfilled our understanding of the smallest structural and functional unit of living organisms, cells.

In this dissertation, we have proven our genetically encoded biosensors to be capable of performing fluorescence imaging in complex biological systems, pushed the genetically encoded Zn^{2+} sensors toward the far-red spectrum, and developed a general strategy to red-shift green fluorescent protein based biosensors.

Although countless fluorescent sensors have been utilized to visualize the important biological signaling networks in mammalian cells, neurons, and live animals,[1] the numerical values of the analytes of interest are essential biological parameters but typically unknown. In almost every genetically encoded indicator, the change in fluorescence intensity indicates only a relative change in dynamics, not a quantitative value for the analyte of interest. Even with FRET-based ratiometric sensors, it can be challenging to determine absolute concentration for an analyte of interest because the two FPs may have different rates of folding, maturation, and photobleaching. Fortunately, in some sensors, changes in different states modulate the lifetime of the electronically excited state, which can be measured as the lifetime of fluorescence. Time can be measured with absolute

accuracy, so lifetime imaging of absolute concentration and membrane potential may be possible. Further work should be done to expand genetically encoded sensors that can be detected under the fluorescence lifetime mode.[2, 3]

Another challenge for fluorescence imaging is the elucidation of biological processes *in vivo*, especially in deeper tissues. Red-shifted fluorescent sensors are desirable for *in vivo* imaging given the reduced phototoxicity, less scattering, decreased absorption, and increased deeper tissue penetration. To date, the far-red FPs and near-infrared biliverdin-based FPs all suffer from low quantum yield or folding issues.[4-8] To perform better *in vivo* imaging, genetically encoded sensors need to be brighter, faster, redder, more photostable, and more sensitive. The next generation of far-red or near-infrared fluorescent proteins must be developed to achieve these goals.

A recently developed strategy to pursue live animal imaging is utilizing photoacoustic waves. Compared with photons, an acoustic wave has better tissue penetration with less background noise. It provides high resolution and contrast in real-time and at extended penetration depths. Deán-Ben et al. have demonstrated the fundamental ability to directly track neural dynamics using optoacoustic in zebrafish transduced with GCaMP5G, a genetically encoded calcium indicator.[9] Recently, they further demonstrated large-scale optoacoustic calcium imaging in isolated murine brain model using GCaMP6f, an improved version of GCaMP5G.[10] Because of their low quantum yield, far-red and near-infrared FPs, such as the IFP family, might be ideal dyes for photoacoustic imaging. In particular, bacterial phytochrome photoreceptors (BphPs),

the origin of IFP family, may be adapted to biosensor engineering for photoacoustic imaging (PAI). The first BphPs derivative demonstrated in PAI was BphP iRFP713[11] (also known as iRFP). iRFP expressed *in vivo* may efficiently incorporate endogenous biliverdin (BV) and can be imaged as deep as 4 mm.[12] This penetration depth of imaging is far beyond the capability of prototypical fluorescent proteins based sensors. Despite this much-improved penetration depth of imaging compared to prototypical fluorescent proteins, the photostability of BphPs is low.[13, 14] To date, directly using fluorescent biosensors for optoacoustic imaging remains problematic due to lack of optimization, and thus not yet been used at live animal level. It is desirable to develop a high-throughput screening method for engineering photoacoustic imaging sensors.

The methods mentioned above, both fluorescence imaging and photoacoustic imaging, require invasive detection to deliver light into the tissue and achieve high resolution of imaging. To achieve noninvasive detection, scientists have synthesized numerous contrast agents for magnetic resonance imaging (MRI).[15] MRI is a powerful technique for brain imaging that could provide a possibility for deep-tissue sensor imaging in animals and humans. MRI is capable of achieving deep tissue penetration, 3D spatial resolution, and high sensitivity. MRI has become a well-developed imaging modality for molecular identity and localization. However, it remains much room for development of MRI-based *in vivo* imaging for biologically relevant reactivity and/or dynamic. Progress has been made to monitor Ca^{2+} dynamics based on gadolinium complexes or superparamagnetic iron oxide nanoparticles.[16-18] Although extracellular Ca^{2+}dynamics have been visualized *in vivo* using these sensors,[19, 20] monitoring intracellular Ca^{2+} has been

much more challenging, due to the lack of delivering methods for existing polar or bulky MRI Ca^{2+} sensors into cells. Barandov et al. developed a manganese-based paramagnetic contrast agent, ManICS1-AM, to permeate cells and allow intracellular Ca^{2+} levels to be monitored.[21] Although the ManICS1-AM contrast agent can emulate properties of fluorescent sensors for intracellular Ca^{2+} imaging, it remains crucial to develop MRI probes with increased Ca^{2+} affinity and optimized interactions between the chelator and the paramagnetic complex. Meanwhile, MRI detection for bioactivities and dynamics other than Ca^{2+} lags far behind, compared to fluorescent sensors. We expect to see more intensive development in this field in the near future.

REFERENCES

1. Greenwald, E. C.; Mehta, S.; Zhang, J., Genetically Encoded Fluorescent Biosensors Illuminate the Spatiotemporal Regulation of Signaling Networks. Chemical Reviews **2018,** 118 (24), 11707-11794.
2. Brinks, D.; Klein, A. J.; Cohen, A. E., Two-Photon Lifetime Imaging of Voltage Indicating Proteins as a Probe of Absolute Membrane Voltage. Biophysical journal **2015,** 109 (5), 914-921.
3. Bilan, D. S.; Pase, L.; Joosen, L.; Gorokhovatsky, A. Y.; Ermakova, Y. G.; Gadella, T. W. J.; Grabher, C.; Schultz, C.; Lukyanov, S.; Belousov, V. V., HyPer-3: A Genetically Encoded H2O2 Probe with Improved Performance for Ratiometric and Fluorescence Lifetime Imaging. ACS Chemical Biology **2013,** 8 (3), 535-542.
4. Chu, J.; Haynes, R. D.; Corbel, S. Y.; Li, P.; González-González, E.; Burg, J. S.; Ataie, N. J.; Lam, A. J.; Cranfill, P. J.; Baird, M. A.; Davidson, M. W.; Ng, H.-L.; Garcia, K. C.; Contag, C. H.; Shen, K.; Blau, H. M.; Lin, M. Z., Non-invasive intravital imaging of cellular differentiation with a bright red-excitable fluorescent protein. Nature methods **2014,** 11 (5), 572-578.
5. Bajar, B. T.; Lam, A. J.; Badiee, R. K.; Oh, Y.-H.; Chu, J.; Zhou, X. X.; Kim, N.; Kim, B. B.; Chung, M.; Yablonovitch, A. L.; Cruz, B. F.; Kulalert, K.; Tao, J. J.; Meyer, T.; Su, X.-D.; Lin, M. Z., Fluorescent indicators for simultaneous reporting of all four cell cycle phases. Nature methods **2016,** 13 (12), 993-996.
6. Yu, D.; Gustafson, W. C.; Han, C.; Lafaye, C.; Noirclerc-Savoye, M.; Ge, W.-P.; Thayer, D. A.; Huang, H.; Kornberg, T. B.; Royant, A.; Jan, L. Y.; Jan, Y. N.;

Weiss, W. A.; Shu, X., An improved monomeric infrared fluorescent protein for neuronal and tumour brain imaging. Nature communications **2014,** 5, 3626.
7. Rodriguez, E. A.; Tran, G. N.; Gross, L. A.; Crisp, J. L.; Shu, X.; Lin, J. Y.; Tsien, R. Y., A far-red fluorescent protein evolved from a cyanobacterial phycobiliprotein. Nature methods **2016,** 13, 763.
8. Qian, Y.; Piatkevich, K. D.; Mc Larney, B.; Abdelfattah, A. S.; Mehta, S.; Murdock, M. H.; Gottschalk, S.; Molina, R. S.; Zhang, W.; Chen, Y.; Wu, J.; Drobizhev, M.; Hughes, T. E.; Zhang, J.; Schreiter, E. R.; Shoham, S.; Razansky, D.; Boyden, E. S.; Campbell, R. E., A genetically encoded near-infrared fluorescent calcium ion indicator. Nature methods **2019,** 16 (2), 171-174.
9. Deán-Ben, X. L.; Sela, G.; Lauri, A.; Kneipp, M.; Ntziachristos, V.; Westmeyer, G. G.; Shoham, S.; Razansky, D., Functional optoacoustic neuro-tomography for scalable whole-brain monitoring of calcium indicators. Light: Science & Applications **2016,** 5 (12), e16201-e16201.
10. Gottschalk, S.; Degtyaruk, O.; Mc Larney, B.; Rebling, J.; Deán-Ben, X. L.; Shoham, S.; Razansky, D., Isolated Murine Brain Model for Large-Scale Optoacoustic Calcium Imaging. Frontiers in Neuroscience **2019,** 13, 290.
11. Filonov, G. S.; Piatkevich, K. D.; Ting, L.-M.; Zhang, J.; Kim, K.; Verkhusha, V. V., Bright and stable near-infrared fluorescent protein for in vivo imaging. Nature Biotechnology **2011,** 29 (8), 757-761.
12. Filonov, G. S.; Krumholz, A.; Xia, J.; Yao, J.; Wang, L. V.; Verkhusha, V. V., Deep-Tissue Photoacoustic Tomography of a Genetically Encoded Near-Infrared Fluorescent Probe. Angewandte Chemie International Edition **2012,** 51 (6), 1448-1451.
13. Vegh, R. B.; Bravaya, K. B.; Bloch, D. A.; Bommarius, A. S.; Tolbert, L. M.; Verkhovsky, M.; Krylov, A. I.; Solntsev, K. M., Chromophore Photoreduction in Red Fluorescent Proteins Is Responsible for Bleaching and Phototoxicity. The Journal of Physical Chemistry B **2014,** 118 (17), 4527-4534.
14. Zhu, J.; Shcherbakova, D. M.; Hontani, Y.; Verkhusha, V. V.; Kennis, J. T. M., Ultrafast excited-state dynamics and fluorescence deactivation of near-infrared fluorescent proteins engineered from bacteriophytochromes. Scientific Reports **2015,** 5 (1), 12840.
15. Que, E. L.; Chang, C. J., Responsive magnetic resonance imaging contrast agents as chemical sensors for metals in biology and medicine. Chemical Society Reviews **2010,** 39 (1), 51-60.
16. Li, W.-h.; Fraser, S. E.; Meade, T. J., A Calcium-Sensitive Magnetic Resonance Imaging Contrast Agent. Journal of the American Chemical Society **1999,** 121 (6), 1413-1414.
17. Angelovski, G.; Fouskova, P.; Mamedov, I.; Canals, S.; Toth, E.; Logothetis, N. K., Smart Magnetic Resonance Imaging Agents that Sense Extracellular Calcium Fluctuations. Chembiochem : a European journal of chemical biology **2008,** 9 (11), 1729-1734.
18. Atanasijevic, T.; Shusteff, M.; Fam, P.; Jasanoff, A., Calcium-sensitive MRI contrast agents based on superparamagnetic iron oxide nanoparticles and calmodulin. Proceedings of the National Academy of Sciences **2006,** 103 (40), 14707.
19. Moussaron, A.; Vibhute, S.; Bianchi, A.; Gündüz, S.; Kotb, S.; Sancey, L.; Motto-Ros, V.; Rizzitelli, S.; Crémillieux, Y.; Lux, F.; Logothetis, N. K.; Tillement, O.;

Angelovski, G., Ultrasmall Nanoplatforms as Calcium-Responsive Contrast Agents for Magnetic Resonance Imaging. Small **2015,** 11 (37), 4900-4909.
20. Okada, S.; Bartelle, B. B.; Li, N.; Breton-Provencher, V.; Lee, J. J.; Rodriguez, E.; Melican, J.; Sur, M.; Jasanoff, A., Calcium-dependent molecular fMRI using a magnetic nanosensor. Nature Nanotechnology **2018,** 13 (6), 473-477.
21. Barandov, A.; Bartelle, B. B.; Williamson, C. G.; Loucks, E. S.; Lippard, S. J.; Jasanoff, A., Sensing intracellular calcium ions using a manganese-based MRI contrast agent. Nature communications **2019,** 10 (1), 897.